Electronic and Magnetic Properties of Multiferroic Based Magnetoelectric Field Effect Devices

by

Stephen Mingda Wu

A dissertation submitted in partial satisfaction of the
requirements for the degree of
Doctor of Philosophy

in

Physics

in the

Graduate Division

of the

University of California, Berkeley

Committee in charge:

Professor Robert C. Dynes, Chair
Professor Ramamoorthy Ramesh
Professor Luke P. Lee

Fall 2012

Electronic and Magnetic Properties of Multiferroic Based Magnetoelectric Field Effect Devices

Abstract

Electronic and Magnetic Properties of Multiferroic Based Magnetoelectric Field Effect Devices

by

Stephen Mingda Wu

Doctor of Philosophy in Physics

University of California, Berkeley

Professor Robert C. Dynes, Chair

The electric field control of ferromagnetism has been a long sought after effect, due to the large number of potential applications in electronic/magnetic devices. Large currents (and hence large powers) are required to generate the large magnetic fields needed to control the magnetization of a ferromagnetic material in a thin film electronic device, which is incompatible with planar integrated circuit technology. Alternatively, creating large electric fields at these scales requires minimal current (and hence minimal power) and is already well established. By exploiting a magnetoelectric material, magnetization can be manipulated in a scalable planar low-power device through the application of electric field. Using this type of device architecture could lead to huge advances in magnetic memory and storage, as well as provide a crucial first step to creating low-power spintronic devices as a replacement for traditional electronics that are reaching the limit of scaling. One possible way to achieve the electric control of ferromagnetism is by controlling exchange bias, the shift of a magnetic hysteresis curve along the applied field axis due to interface interactions between coupled antiferromagnetic (AFM) and ferromagnetic (FM) materials. If it is possible to shift exchange bias through the coercive field of the FM, magnetization can be reversed. Reaching this goal requires a careful understanding of antiferromagnetism, ferromagnetism and the interactions between the two when coupled (exchange bias). The main focus of this thesis will be the design, fabrication, characterization, and understanding of an electric field effect device where we are able to reversibly modulate between two exchange bias states with opposite polarity in a thin film ferromagnet by coupling it to a multiferroic (ferroelectric/antiferromagnetic) material.

The multiferroic material $BiFeO_3$ (BFO), an AFM and ferroelectric (FE) with coupled AFM/FE order parameters, is a prime candidate material for affecting change in exchange bias systems. When coupled to a thin film ferromagnet such as the colossal magnetoresistive manganite $La_{0.7}Sr_{0.3}MnO_3$ (LSMO), one can envision a system where FE order is switched in BFO, which induces a change in AFM order in BFO, which induces a change in exchange bias in LSMO. Here, an electric field effect device is created using BFO as the dielectric and

LSMO as the conducting channel to realize just such a system. Heteroepitaxially deposited BFO (3 nm)/LSMO (200 nm) heterostructures are grown on $SrTiO_3$ (100) substrates and subsequently patterned into field effect devices using a fabrication process involving photolithography and argon ion milling. These devices are then characterized through magneto-transport measurements to characterize the magnetic properties of the LSMO channel with respect to BFO FE polarization. Through these measurements this thesis shows, for the first time, exchange bias is directly controlled with electric field without temperature cycling or any electric or magnetic field cooling/biasing. This effect is reversible and comes concurrently with the modulation of channel resistance (sometimes over 300%), the modulation of magnetic coercivity, and magnetic Curie temperature.

Based on these results and the current understanding of exchange bias we propose a model to understand the electric control of exchange bias. In this model the coupled antiferromagnetic/ferroelectric order in BFO along with the modulation of interfacial exchange interactions due to ionic displacement of Fe^{3+} in BFO relative to $Mn^{3+/4+}$ in LSMO cause exchange bias modulation.

To my mom and dad.

Contents

List of Figures

Acknowledgments

I am greatly indebted to a large number of people that have shaped the direction of my life throughout the course of my graduate career. Each person having provided his or her unique influence. Only through the assistance, support, motivation, and mentorship of these individuals could I have achieved what I have.

Firstly, many thanks go to Bob Dynes for being a wonderful advisor, mentor, and scientific role model throughout entire scientific career. The work I have done could not have been accomplished without your support and motivation. Along with teaching me the technical details of working in a lab, you have also shown me firsthand what it means to be an outstanding scientist. I will always cherish the stories that you have told, and advice that you have given, as they will have prepared me well for my future. Next, I would like to thank Ramamoorthy Ramesh for his contribution as my co-advisor in my graduate work at Berkeley. Your support and guidance was invaluable in allowing me to progress into a mature researcher. I am always in awe of your dedication to science and your lab. Both you and Bob respond to emails faster than anyone I have ever worked with previously in my life. You provided me with interesting research topics and always guided me to the right sources of people and information when it was needed. You pushed me when I needed to be pushed, telling me I was capable of solving problems when I didn't believe so myself, and for that I am forever thankful. Thanks also goes to John Clarke for being a great advisor during my late undergraduate career and early graduate career, and for being a great mentor throughout. There are things that I have learned from you about being a scientist that I will take with me for the rest of my life. I will always appreciate how you welcomed us into your home and created a tight knit social community in the laboratory environment, and how that connection is not easily broken after people leave the group. I would also like to thank both Professors Luke Lee and Dung-Hai Lee for sitting on my qualifying exam committee. Prof. Luke Lee deserves special thanks for attending on such short notice.

Many thanks also go to Shane Cybart for his role in guiding and mentoring me throughout both my undergraduate and graduate research career. A large portion of why I am the person I am today is due to our constant collaboration and interaction. Through all the good times and bad times you were there with me to either celebrate or commiserate. Despite all our arguments throughout the years about serious matters like science and politics, or more trivial ones like food, we always worked things out and were stronger because of it. Without your influence I would be a greatly different person than I am today. I would also like to thank Steve Anton for being a great friend and labmate through all the time we worked together as well as all the students who came before me in the lab who acted as friends and mentors, such as Travis Hime, Sarah Busch, Michael Hatridge, Nathan Kelso, and Jed Johnson. My interactions with the many Postdoctoral scholars, and visiting professors such as Emile Hoskinson, Ke Chen, Rich Barber, Darin Kinion and R. Vijay have provided me with invaluable knowledge that will serve me well in my future endeavors. Also, thanks to the many research collaborators in the Ramesh group that have helped me accomplish what I have today, including Pu Yu,Jing-Xing Zhang, Di Yi, Ying-Hao "Eddie" Chu, Jan Seidel,

and Lane Martin. Additionally I would like to recognize the many undergraduate researchers who worked in our labs and contributed to the success of our research, Philip Chen, Travis Wong, Jasper Drisko, Patricia S. Yen, James M. Parker, and Christine Chen.

Finally I would like to thank my family and friends, who have loved and supported me throughout my time with them. To my mom and dad, I could not have accomplished what I have today without your unwavering support. To my friends, knowing that I could rely on everyone to help me through crises both physical and emotional was the most valuable gift any friend could ever ask for. Without this support, love and motivation from my friends and family I would only be a fraction of the person I am now.

Chapter 1

Introduction

In the past 15 years there has been considerable growth in activity in the area of magnetic materials. With the advent of new technologies for the thin film growth and characterization of such materials, a door has been opened for the use of these materials in magnetic device applications. One fundamental aspect of these magnetic materials that remains a prerequisite for application is the ability to control the magnetization within the material in a straightforward way. Many different approaches have been taken along this path to achieve this, for example the use of read-write heads on hard disk drives to magnetize and read magnetic domains on magnetic disks. The focus of this thesis will be the use of electric fields to control the properties of a ferromagnetic thin film. If this could be accomplished we would be able to create high-density, scalable, low-power, planar magnetic devices; all properties that are desirable for memory or spintronics applications. In this chapter, the requisite background information is presented to serve as a base to introduce the fundamental idea behind the device which is the main topic of this thesis. First, the fundamentals of the magnetoelectric effect, the electric control of magnetization or the magnetic control of polarization, are introduced. Then, multiferroic materials, materials that have more than one type of ferroic order, are discussed as a possible (but currently difficult) method to obtain the desired magnetoelectric effect. Next, exchange bias, a shift of the magnetic hysteresis curve along the applied field axis, is reviewed and discussed as an alternative method to achieve the electric control of magnetism. Finally, we summarize the current world of devices that attempt to achieve magnetoelectric control through exchange bias manipulation and introduce our own multiferroic field effect device that obtains the full electric control of exchange bias that other devices have been unsuccessful at in the past.

1.1 Magnetoelectric Effect

In the most general sense, the magnetoelectric effect is the induction of magnetization by an electric field or of polarization by a magnetic field. The effect was first conjectured by Curie in 1894 [1], although the first rigorous experimental confirmation of electric field induced

magnetization did not come until the 1960s, where it was shown to exist in Cr_2O_3 by Astrov [2], after being theoretically predicted by Dzyaloshinskii [3, 4]. This caused a large effort to find other materials systems that exhibited magnetoelectric behavior but was relatively unsuccessful until recently when the possibility of applications in electronics started again drawing the attention of the scientific community. Formally the magnetoelectric effect can be described using Landau theory through expressing the free energy of a single-phase crystal in terms of applied magnetic field H_i and applied electric field E_i [5].

$$-F(E,H) = \frac{1}{2}\varepsilon_0\varepsilon_{ij}E_iE_j + \frac{1}{2}\mu_0\mu_{ij}H_iH_j + \alpha_{ij}E_iH_j + \frac{\beta_{ijk}}{2}E_iH_jH_k + \frac{\gamma_{ijk}}{2}H_iE_jE_k + \dots \quad (1.1)$$

Here the second rank tensors, ε_{ij} represents the relative permittivity, μ_{ij} represents the relative permiability,and α_{ij} represents the linear magnetoelectric coupling. The third rank tensors β_{ijk}, and γ_{ijk} represent higher order magnetoelectric coupling terms. By differentiating the free energy with respect to E_i and H_i we obtain:

$$P_i = -\frac{\partial F}{\partial E_i} = \varepsilon_0\varepsilon_{ij}E_j + \alpha_{ij}H_j + \frac{\beta_{ijk}}{2}H_jH_k + \dots \quad (1.2)$$

$$M_i = -\frac{\partial F}{\partial H_i} = \mu_0\mu_{ij}H_j + \alpha_{ji}E_j + \frac{\gamma_{ijk}}{2}E_jE_k + \dots \quad (1.3)$$

Where the first term of equations 1.2 and 1.3 represent linear susceptibility, the second represents the linear magnetoelectric effect, and the third represents higher order magnetoelectric effects. The focus of most research is on the linear magnetoelectric term, therefore the term "linear" is generally omitted when referring to the magnetoelectric effect, a convention we will follow in this text. Focus has generally been to find materials that both exhibit the magnetoelectric effect and also have a large α_{ij} for applications purposes. It has been shown though [4, 5], that α_{ij} is fundamentally limited by the relation:

$$\alpha_{ij}^2 \leq \varepsilon\mu_0\varepsilon_{ii}\mu_{jj} \quad (1.4)$$

Due to this, two different approaches have been taken to achieve large magnetoelectric coupling [4]. The first was to drop the idea that the magnetoelectric effect had to occur in a single material, and use composite systems where piezoelectric materials were coupled to magnetostrictive materials. In this way, applying electric fields causes a change in the strain of the piezoelectric material that is passed on to a coupled magnetostrictive material where a change in strain causes a change in magnetization. The second approach, was to use materials that have simultaneously large magnetic and electric susceptibilities. The highest susceptibilities occur in ferromagnetic (FM) and ferroelectric (FE) materials, so their coexistence in a single multiferroic material would be the ideal candidate for magnetoelectric coupling. Since piezoelectric/magnetostrictive composite systems involve more caveats to operation, such as frequency dependence of magnetoelectric coupling strength and do not necessarily retain either magnetization or polarization after turning off electric or magnetic

fields, here we will first examine multiferroic magnetoelectrics. Specifically, we focus on the electric field control of ferromagnetism through the use of multiferroics. Such a single-phase ferroelectric/ferromagnetic material would retain magnetization information after the application of electric field and offer no frequency dependence of magnetoelectric coupling, and thus be directly applicable to magnetic memory and spintronics applications. In the following section we explore the background behind multiferroics and how they may be used to achieve electric control of magnetization.

1.2 Multiferroic Materials

By definition, a multiferroic material is one that simultaneously shows more than one type of ferroic order such as, ferromagnetism, ferroelectricity, or ferroelasticity. A large amount of interest has been generated in the field of multiferroic materials due to the prospect of finding a single-phase magnetoelectric multiferroic material with coupled ferromagnetic and ferroelectric order parameters, which would be involve both interesting physics and at the same time allow for interesting applications[6–8]. This, as it turns out, is not an easy prospect due to the large number of restrictions placed upon each material as we demand the properties that we want from it. This scarcity of materials is illustrated by Fig. 1.1, where the requirements for magnetoelectric multiferroics are explicitly drawn out, and only a small subset of materials meet that need [5]. One of the seminal theoretical works on multiferroics suggested that, in fact, many of the key requirements for the coexistence of ferromagnetism and ferroelectricity are mutually exclusive [9]. Since then, the challenge has been to work around these limitations and many groups have recently come up with moderate magnetoelectric coupling factors in single-phase multiferroics[10, 11]. Here we review the constituent forms of order that go into searching for a ferroelectric ferromagnet and what significant challenges exist in finding one.

Ferromagnetism

A material is said to be ferromagnetic when it exhibits a spontaneous macroscopic magnetic moment without the application of a magnetic field. Typically a phase transition occurs from a high-temperature paramagnetic state to a low-temperature ferromagnetic state, at a temperature known as the Curie temperature T_C. Due to the formation of magnetic domains, as prepared samples of ferromagnets may not necessarily have a net magnetization due to the random ordering of these domains. Upon application of a magnetic field, domains are aligned and a net magnetization is produced. This causes ferromagnets to exhibit hysteresis in magnetization vs. applied magnetic field plots as shown in Fig. 1.2a. Upon applying positive magnetic field, the magnetization increases until reaching a value known as the saturation magnetization M_S. Now as the magnetic field is reversed, even at zero applied magnetic field a spontaneous magnetization still exists up to a point known as a coercive field H_C. The coercive field is the magnetic field in the reverse direction needed

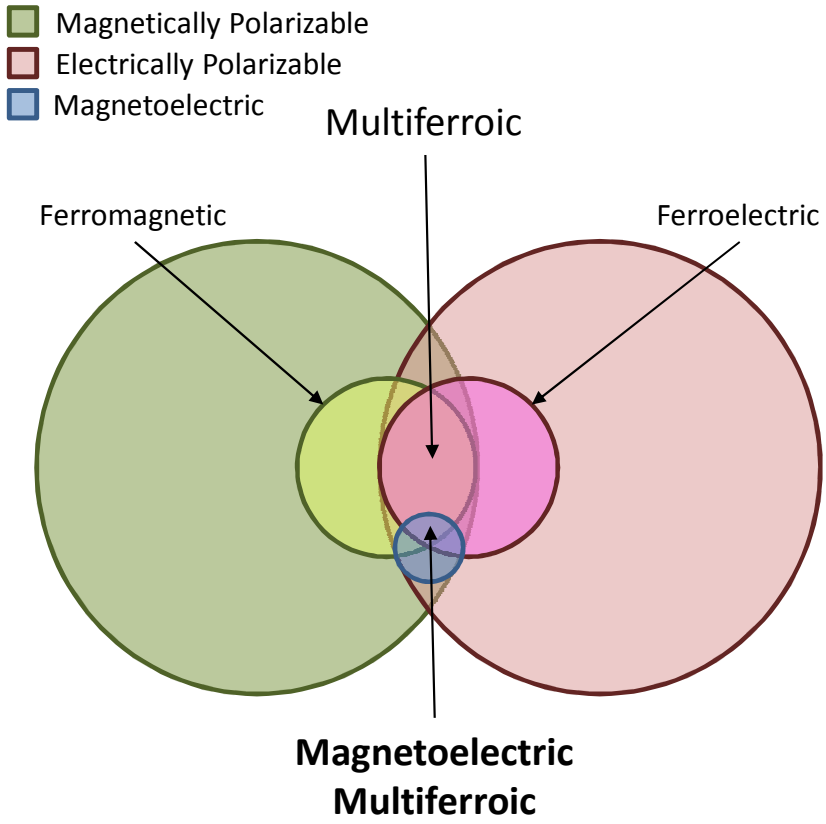

Figure 1.1: An illustration of the large number of requirements placed on a magnetoelectric multiferroic and why these such materials are scarce. Within the space of all materials only a small subset are magnetically or electrically polarizable. Within those spaces, only a small subset are ferromagnetic or ferroelectric. Then there exists only a small overlap between those two groups, and an even smaller subset within that group when the requirement for magnetoelectric coupling is added. Overall, what is left is a large possible space to search for an extremely small group of materials with the properties that we desire.

to reduce the net magnetization to zero before flipping magnetization completely. The microscopic origin of ferromagnetism involves the exchange interactions between the electrons of individual magnetic ions that favors the alignment of electronic magnetic moments over anti-alignment. The exact mechanism for each system may be slightly different and result in slightly different magnetic properties. Most elemental ferromagnets, for example, are a result of direct exchange, while in the doped manganites double exchange is the relevant interaction term. Several other types of exchange interactions exist such as RKKY and superexchange interactions. These different types of exchange interaction can also cause antiferromagnetism (AFM) where the spins are anti-aligned between ions. The full theory of ferromagnetism is well studied and involves a depth that is beyond the scope of this thesis.

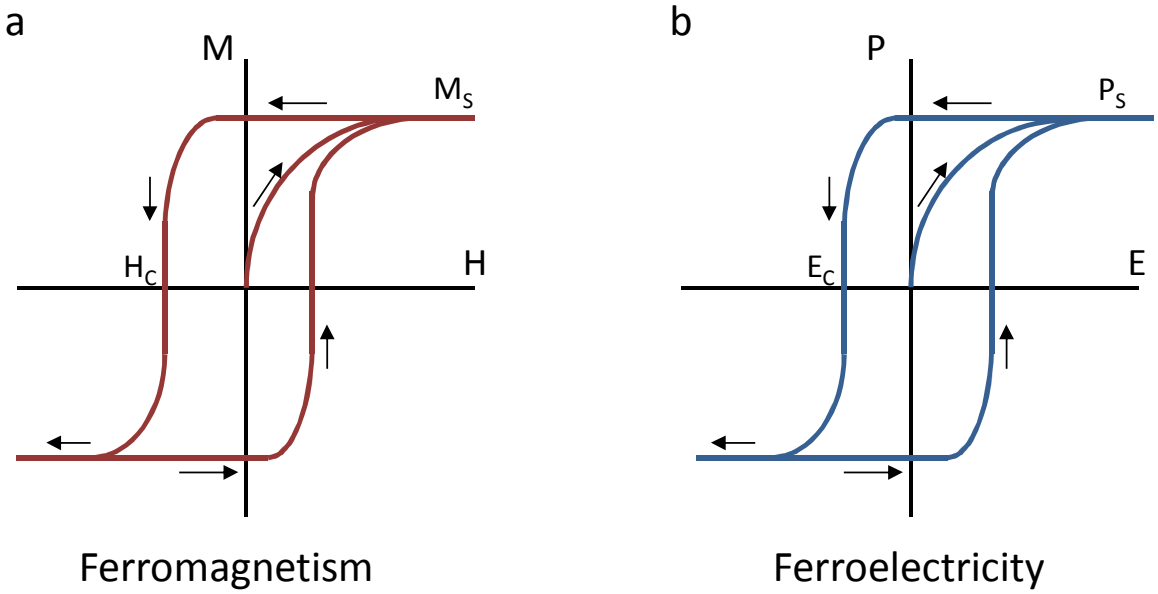

Figure 1.2: A depiction of the similarities between (a) ferromagnetism and (b) ferroelectricity. M_S and P_S represent the saturation magnetization and polarization, respectively. H_C and E_C represent the electric and magnetic coercive fields, respectively.

There are, however, some fundamental requirements for ferromagnetism worth mentioning: the violation of time reversal symmetry, and the existence of unpaired d orbital electrons. Both of these factors limit the number of possible materials that exhibit ferromagnetism, which will become important as we look for materials that both exhibit ferromagnetism and ferroelectricity.

Ferroelectricity

By making an exact analogy to ferromagnetism, a ferroelectric material exhibits a spontaneous macroscopic polarization without the application of electric field. There is typically also a phase transition that occurs between a paraelectric to a ferroelectric state, and an analogous hysteresis curve can be plotted involving polarization vs. electric field as shown in Fig. 1.2b. The earliest studies of ferroelectricity occurred in the 1920's involving Rochelle salt, the first ferroelectric to be discovered [12]. Since then, many others have been discovered and applications for ferroelectrics have hugely increased.

Fundamentally, when a lattice of oppositely charged ions are put together the structure is inherently unstable. However, due to a careful balancing act of ionic placement, a stable

structure can be created from these constituent ions. Whether this balancing act favors a symmetric structure or a nonsymmetric structure as a stabilizer is key to ferroelectricity. In the formation of ferroelectric materials, typically stabilization results in a double well potential that favors a distorted structure rather than a symmetric one. By using electric field to switch between two different nonsymmetric states a spontaneous polarization can develop due to the relative position of the cations to the anions, thus leading to ferroelectricity. The prototypical ferroelectric is the transition metal oxide, where often this type of non-centrosymmetric distortion is caused by the hybridization of the d-orbitals in the transition metal with the p-orbitals of the surrounding oxygen due to covalent bonding [13]. Because of these non-centrosymmetric structures in ferroelectric materials inversion symmetry must be broken, placing a limit on the number of ferroelectric systems that exist.

Single phase magnetoelectric multiferroics

Based off the previous two sections we can see that there exists challenges to finding both a ferromagnetic and ferroelectric material. Ferroelectrics require spatial inversion symmetry, but not time reversal symmetry, while ferromagnets require time reversal symmetry, but not spatial inversion symmetry. This brings the number of compatible Shubnikov point groups down from a total of 122 to a minuscule 13 [9]. Additionally, ferromagnetism arises from unpaired d-orbital electrons, where ferroelectricity relies on the covalent bonding of these d-orbitals to induce a non-centrosymmetric distortion. Ferroelectrics are also typically insulating materials (otherwise polarization would induce an electric current to flow) ,and while there is no requirement for ferromagnets to have specific electrical properties, they are often metallic. Since these many different factors are often incompatible, it is not a surprise that finding magnetoelectric multiferroics is not an easy task. In fact, to date there are no fully coupled single phase ferroelectric/ferromagnetic magnetoelectric systems.

Several methods have been used recently, though, as an attempt to try to get around these requirements. For example,in transition metal perovskite oxide materials (oxides with the form ABO_3), the A-site ion is used to to induce ferroelectricity rather than the B-site ion as is typical for most ferroelectrics. In this way, ferromagnetic properties can derive from B-site ionic interactions, while ferroelectricity can be induced from the A-site ions. $BiMnO_3$ derives ferroelecity from the Bi ion, leaving the Mn ion free to develop magnetic interactions [14]. In this material there is both large polarization and magnetization, although only a weak coupling between the two [15]. Other methods involve using improper ferroelectrics that derive ferroelectricity through non-hybridization methods [16], or using ferroelectricity that arises from magnetic ordering[17]. While there is a scarcity of simultaneously ferroelectric/ferromagnetic magnetoelectric materials, this is not the case with simultaneously ferroelectric/antiferromagnetic coupled systems[18, 19]. Thus, in the next section we introduce exchange bias as a method of controlling magnetism in a coupled two material system, which avoids the complications of finding single phase mangetoelectric materials. Using this method we combine the best aspects of both multiferroic and composite magnetoelectric systems.

1.3 Exchange Bias

Exchange bias occurs in coupled antiferromagnetic/ferromagnetic systems, where a unidirectional shift along the applied field axis develops in ferromagnetic hysteresis curve due to interfacial spin effects between the AFM and FM materials. Phenomenologically, adding an AFM layer to a FM layer does not immediately induce this shift in hysteresis, only an increase in coercivity, but when a exchange bias system is cooled through the Neel temperature of the AFM layer in an applied magnetic field a shift develops in the opposite direction of the cooling field [20]. These effects are outlined in Fig. 1.3. Exchange bias was first discovered in 1956 by Meiklejohn and Bean [21], and has since garnered a lot of attention due to its usefulness in magnetic device applications such as magnetic stabilizers in hard disk read/write heads. Though, only recently has its usefulness in magnetoelectric devices been exploited [7, 22]. Despite being discovered over 50 years ago, a complete understanding of this phenomenon has not yet been developed. However, recent experimental and theoretical work has shed light on many aspects of exchange bias that goes beyond the simple models developed immediately after its discovery. Here we start with simplest early model

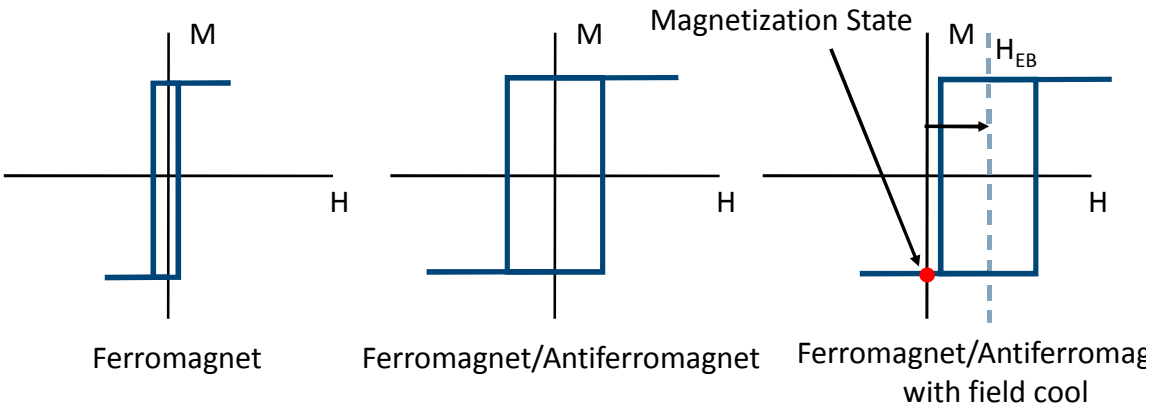

Figure 1.3: The effects of coupling a ferromagnetic (FM) material to a antiferromagnetic (AFM) material are depicted. In a FM only system, the system has a small coercivity, and is symmetric about the applied magnetic field axis. When adding an AFM to the FM, coercive field is enhanced due to a "spin drag" effect but the hysteresis curve is still symmetric. By cooling the AFM/FM system through the Neel temperature of the AFM material in applied magnetic field, coercive enhancement is seen and an exchange bias field develops and the hysteresis curve is no longer symmetric.

to arise for exchange bias systems. Typically they involved a simple colinear spin system with a perfect interface between the AFM and FM as depicted in Fig. 1.4 [20, 23, 24]. First we start above the Neel temperature of the AFM and apply a magnetic field, aligning the

FM but not the AFM where the spins are randomized (Fig. 1.4a). Next, temperature is lowered through the AFM Neel temperature such that AFM order develops and AFM spins at the interface are aligned to the FM due to interfacial magnetic interactions (Fig.1.4b) . In this case, they align ferromagnetically, although AFM alignment is also possible depending on the type of interface interactions. Now that the AFM spins are frozen-in due to AFM anisotropy, when we sweep magnetic field in the opposite direction additional magnetic field is needed to reverse the magnetization because of a force that develops on the FM due to interfacial interactions (Fig.1.4c). When field is swept back now, the extra force now favors the original spin direction and thus less field is required to flip the spins back (Fig.1.4d). The end result is a hysteresis curve that is shifted in the direction opposite to the original magnetic cooling field.

This model can be described as a simple energy minimization problem as an attempt to quantify the exchange bias field. Here the energy per unit area of an exchange bias system is described as:

$$E = -HM_{FM}t_{FM}cos(\theta - \beta) + K_{FM}t_{FM}sin^2(\beta) + K_{AF}t_{AF}sin^2(\alpha) - J_{INT}cos(\beta - \alpha) \quad (1.5)$$

Where H is the applied magnetic field, M_{FM} is the saturation magnetization of the FM, t_{FM} is the thickness of the FM, t_{AFM} is the thickness of the AFM, K_{FM} is the FM anisotropy energy, K_{AFM} is the AFM anisotropy energy, and J_{INT} is the interfacial coupling constant. Here the anisotropy axis of both the FM and the AFM are assumed to be the same, and θ, β,and α are the angles of H, M_{FM}, and M_{AFM} from that axis, respectively. It is typically assumed that K_{FM} is much smaller than K_{AFM}, which is typically true experimentally, thus simplifying the equations.

$$E = -HM_{FM}t_{FM}cos(\theta - \beta) + K_{FM}t_{FM}sin^2(\beta) - J_{INT}cos(\beta - \alpha) \quad (1.6)$$

From here we can minimize the energy with respect to α and β, in two different limiting cases which results in different spin behavior. Starting with $K_{AFM}t_{AFM} \gg J_{INT}$, here the energy is minimized by keeping α small independently of β, which leads to the AFM spins being pinned, and resulting in an exchange bias of:

$$H_{EB} = \frac{J_{INT}}{M_{FM}t_{FM}} \quad (1.7)$$

In the second case, with $K_{AFM}t_{AFM} \ll J_{INT}$, the energy is minimized by keeping $\beta - \alpha$ small, and thus the AFM spins will rotate with the FM spins, and cause no exchange bias. In this case coercivity is increased due to the force from the interface still "dragging" the spins causing them to not flip as easily. This idea of unequally contributing AFM spins goes a long way to explain some of the behavior in exchange bias systems. Some spins are pinned and contribute to exchange bias without enhancing coercivity much, while other spins rotate with the AFM not contributing to exchange bias but enhancing coercivity more [25]. Despite the successes of this simple model, there are still huge discrepancies between theory and reality.

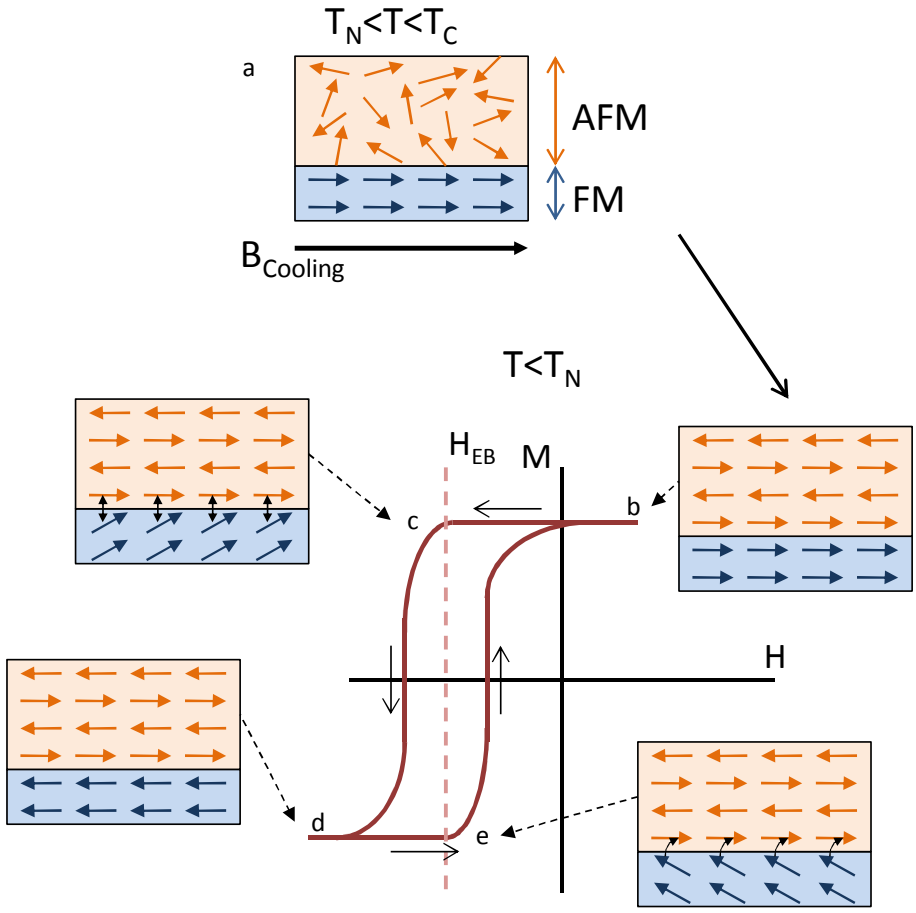

Figure 1.4: A simple model of exchange bias. A microscopic picture of interface spin structure is presented along with the macroscopic effect on the magnetic hysteresis curve. Initially the system is above the Neel temperature of the AFM (a), and is cooled with field to a starting state (b). Magnetic field is then swept in the opposite direction and back depicted in (c), (d), and (e).

For example, the estimated value of exchange bias is orders of magnitude larger than typical observed values. Several theories have since tried to resolve this apparent incongruity, by introducing models that include AF domain walls forming at the interface [26], or rough interfaces [27]. All such models involve a unique interface structure where only a fraction of the spins in the AFM are contributing to exchange bias. Recent experimental work using x-ray spectroscopy have shown that the underlying idea behind these models is correct and that in some systems only around 4 percent of AFM interface spins are pinned [28].

Another failure point of the simplified models is the reliance on systems with uncompensated interfaces, where all the AFM spins at the interface lie in the same direction. Exchange bias exists in many systems where it has been shown that the type of antiferromagnetism causes the interface to be magnetically compensated such that there is no net magnetization at the interface layer in the AFM. A few theories have emerged attempting to explain this and other unexplained exchange bias effects but a full picture has not yet emerged due to the difficulty of viewing the spin structure of an atomically thin interface layer [23–25, 29]. In this thesis we attempt to exploit exchange bias as a mechanism to affect the magnetism in a thin film ferromagnet, and along the way attempt to add to the understanding of exchange bias physics.

1.4 Magnetoelectric Devices Using Multiferroics

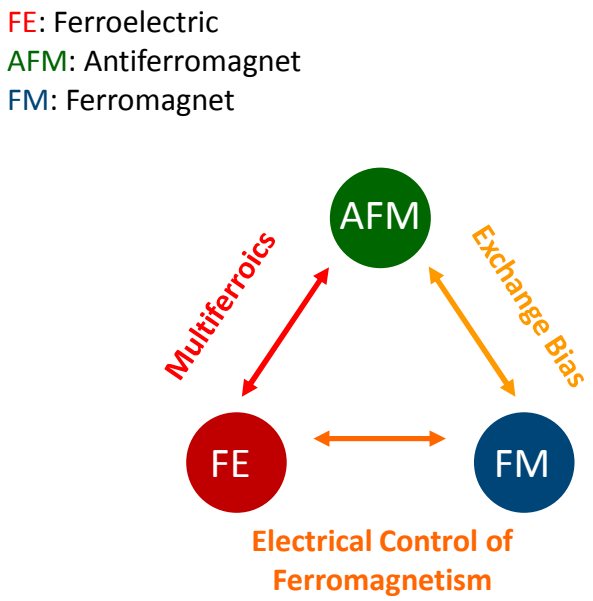

Figure 1.5: Using an intermediate order parameter as a method to control ferromagnetism through ferroelectricity.

Instead of the typical approach of finding single-phase multiferroics with coupled FM and FE order parameters, a separate movement is growing in the field of magnetoelectric devices where multiferroics are used in conjunction with another material to affect magnetism [22]. By using an antiferromagnetic ferroelectric with coupled order parameters we can attempt to use the antiferromagnetism as a form of intermediate order to connect ferroelectrcity to

ferromagnetism as illustrated in Fig. 1.5 [7]. Many groups have seen that the electric control of exchange bias as a necessary first step in using this technique. If it is possible to electrically shift exchange bias through the coercive field of the FM, magnetization of the FM film can be reversed and thus magnetoelectric coupling can be achieved (Fig. 1.6). There have

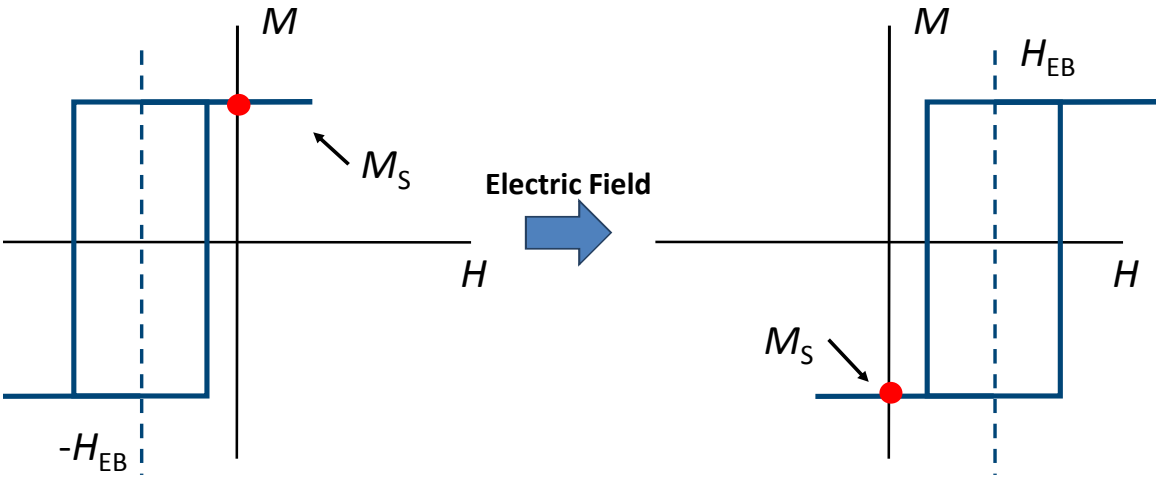

Figure 1.6: A schematic depicting using the electric control of exchange bias to control the magnetization of a ferromagnet.

been several groups who have attempted to control exchange bias using electric field with varying degrees of success. Each attempt uses different materials and device architectures, each having its own unique limitations for operation, and thus falling just short of full direct electrical control of exchange bias. Using multiferroic $YMnO_3$/permalloy bilayers, Laukhin et al. showed that it was possible to field cool a device and subsequently irreversibly suppress exchange bias in this system [30]. Later, work by He et al. using Cr_2O_3 coupled to Pd/Co multilayers showed that it was possible to reversibly switch between two different exchange bias polarity states through the application of electric field and an additional applied magnetic field after magnetoelectric field cooling [31]. The focus of this thesis is the use of multiferroic $BiFeO_3$ with ferromagnetic $La_{0.7}Sr_{0.3}MnO_3$ to create a multiferroic field effect device with reversible static control of the polarity of exchange bias, using no additional cooling fields and no additional caveats, the first time this behavior has ever been demonstrated in any device. Achieving this is a huge first step in the direction of fully electrically controllable magnetoelectric devices, and highlights many important aspects of the physics of exchange bias.

1.5 Organization of Dissertation

The remainder of this dissertation includes 5 more chapters. Chapter 2 focuses on the motivation of choosing multiferroic $BiFeO_3$ and ferromagnetic $La_{0.7}Sr_{0.3}MnO_3$ as the relevant materials for our device. Chapter 3 focuses on the the design of the multiferroic field effect device,and the fabrication techniques used in its construction. Chapter 4 focuses on electrical and magnetic characterization of the device. Here we introduce the magnetotransport characterization system, and the experimental techniques involved in measuring magnetic properties using electrical transport. The results of the experiments directly show that we achieve the full electric control of exchange bias and provide evidence for the model introduced in chapter 5. Chapter 5 discuses the results of Chapter 4 and introduces a simple model based on our current knowledge of exchange bias and multiferroics. Also in this chapter a brief discussion is included about how what steps need to be taken to achieve the full control of magnetization at room temperature. Finally, chapter 6 explains what is left unknown about this system and what future experimentation can shed light in these areas.

Chapter 2

$BiFeO_3/La_{0.7}Sr_{0.3}MnO_3$ Heterostructures

2.1 Multiferroic $BiFeO_3$

A large amount of interest in antiferromagnetic ferroelectrics have developed recently specifically for the applications to the magnetoelectric effect [7, 8, 32]. Many oxide AFM/FE multiferroics exist such as $YMnO_3$ (T_N=∼90 K, T_C=∼900 K) [33, 34], or $BiMnO_3$ (T_N=∼100 K, T_N=∼450 K) [15], but one of the most ideal materials for exploring composite magnetoelectric systems with multiferroics is $BiFeO_3$ (BFO). BFO is, to date, the only room temperature multiferroic (AFM/FE), having a ferroelectric T_C of ∼1103 K and an antiferromagnetic T_N of ∼673 K [35]. Here we take advantage of these properties to attempt to indirectly couple ferroelectricity to ferromagnetism. Historically, BFO was first synthesized in bulk in the late 1950's where it was suspected to contain both ferroelectric and antiferromagnetic order, although this was not shown until years later [36]. Initial structural investigations showed that in single crystal BFO, the unit cell is rhombohedral and takes the form of two distorted perovskite cells connected along pseudocubic [111] direction [37]. Within these perovskite cells the oxygen octahedra are rotated in opposite directions by ±13.8° forming an antiferrodistortive octahedral tilt lattice. In the early 1970's it was shown, in bulk BFO, that there was a net ferroelectric polarization of 6.1 $\mu C/cm^2$ along the [111] direction of the crystal, which is small compared to other ferroelectric systems of the time [38]. Later it was also shown that ferroelectricity was due to the hybridization of the A-site ion (Bi) to oxygen ions resulting in a relative displacement to the oxygen octahedra, which exists in contrast to typical ferroelectricity which relies on hybridization of the B-site ion [14]. Investigations into the magnetic ordering using neutron diffraction were performed in the 1980's to reveal G-type antiferromagnetic order due to magnetic superexchange in Fe^{3+} [39]. Additionally, the symmetry of the system allows for a canting of the AFM moment that would allow for weak ferromagnetism due to Dzyaloshinskii-Moriya interactions. Typically, in bulk films this weak magnetism is quenched due to the the canted spins orienting in a cycloidal structure

along the [110] direction with a periodicity of ∼62 nm [40].

After most of the initial studies on BFO were performed, a wain in BFO related research occurred until 2003 when Wang et. al. first grew high quality thin film BFO samples and reported an "enhancement" of ferroelectricity from a saturation polarization of 6.1 μC/cm^2 to 90 μC/cm^2 [11]. Along with this, a significant magnetization can also be detected, which suggests that the spin cycloid structure in bulk BFO has been suppressed. Studies have shown that these properties were intrinsic to the material, and only revealed themselves when controlled thin film growth allowed for higher quality samples; low polarization values of bulk samples were due to poor quality materials. Since this seminal work, research interest in BFO has exploded and many interesting properties of BFO have been exploited for applications. In the next section we explore some of the magnetoelectric properties of BFO.

Magnetoelectric coupling in $BiFeO_3$

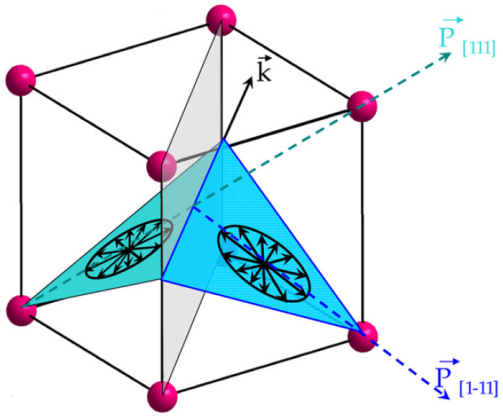

Figure 2.1: Depiction of the magnetic easy plane in bulk BFO. The vector $\vec{k}$ represents the cycloid propagation vector, and the vectors $\vec{P}$ represent the polarization vectors. Together, these two vectors define the easy magnetic plane for bulk BFO. Adapted from [41].

In thin film BFO, there exists a small single phase magnetoelectric coupling effect (3 V/cm·Oe) that exists due to the coupling of the AFM canting and ferroelectric polarization [11]. However, a more interesting type of magnetoelectric coupling exists at a more subtle level. Detailed study on bulk BFO has shown that the magnetic moments rotate along an easy plane defined by the polarization vector (P$\|[111]_{pseudocubic}$) and the cycloid propagation vector (k$\|[10\text{-}1]_{pseudocubic}$) as shown in Fig. 2.1. Thus, by changing the polarization vector by either a 71° or 109° shift, the AFM easy plane can be controlled [41, 42]. While this is

a groundbreaking effect, in bulk BFO the existence of a spin cycloid makes these changes hard to exploit, but in thin film BFO this is a different story.

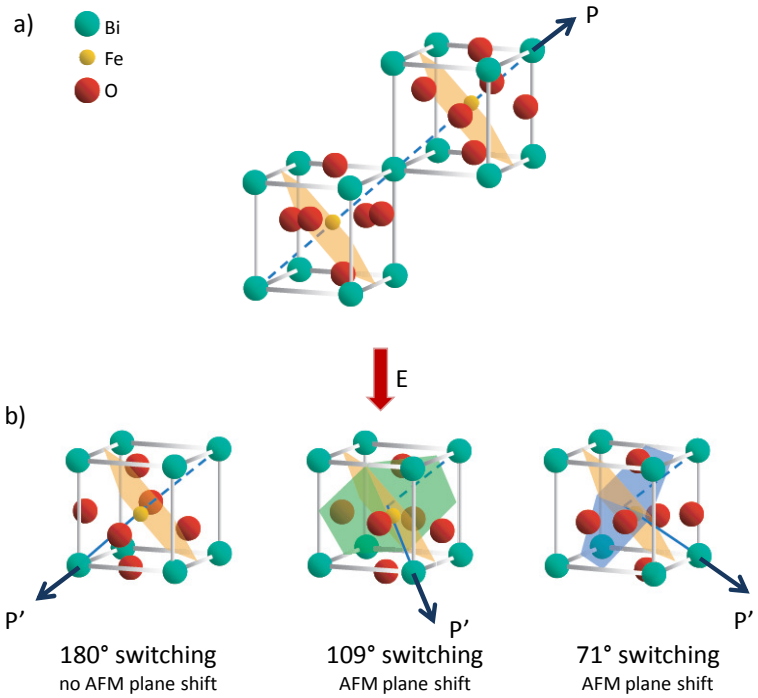

Figure 2.2: Thin film BFO is depicted in (a), where the out of plane polarization is defined to be up, as represented by P. The easy magnetic plane is depicted by the plane perpendicular to the polarization vector P. When an electric field is applied there are three different possible switching events, as depicted in (b). 180° switches do not change the AFM easy plane, while 109° and 71° switching does. Adapted from [19].

Since there is a suppression of the cycloidal moment in thin film BFO, a favorable change in the relationship between AFM spin orientation and FE polarization occurs. Theoretical studies have shown that in thin film BFO the spins are homogenously G-type antiferromagnetic with a slight cant, without the cycloid [43]. The orientation of these spins exist in an easy plane that lies perpendicular to the polarization vector with six degenerate preferred orientations within this plane. By changing the direction of the polarization vector we can control the easy magnetic plane, exactly in the case of bulk BFO, but due to the lack of a spin cycloid we are able to now observe the direct macroscopic effects (Fig. 2.2). Zhao et. al. shows that there is a direct one to one correlation between AFM domains and FE polarization using a combination of piezoresponse force microscopy and X-ray photoemission electron microscopy [19]. This fact is of extreme importance as it opens the possibility to exploit the AFM/FE coupling in BFO for magnetoelectric devices, as is the case with the

device which is the central focus of this thesis.

2.2 Ferromagnetic $La_{0.7}Sr_{0.3}MnO_3$

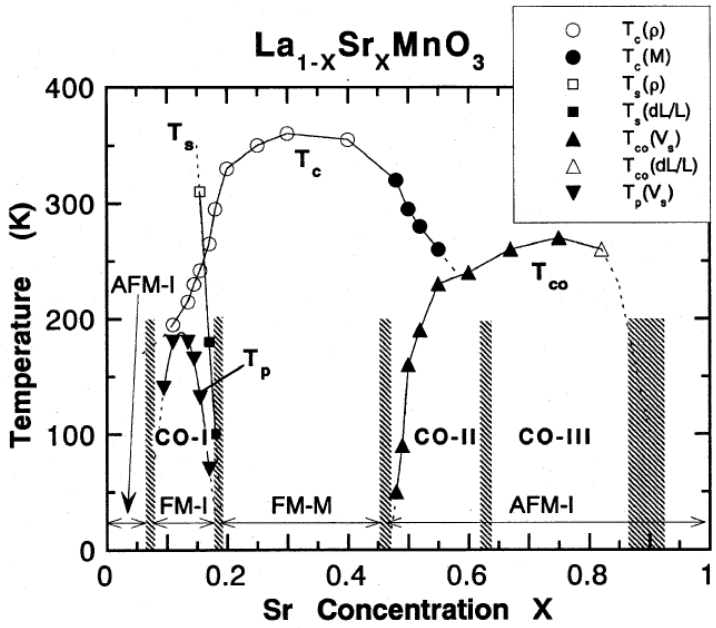

Figure 2.3: The phase diagram of $La_{1-x}Sr_xMnO_3$ with increasing Sr concentration x. Various different magnetic and conductive states such as antiferromagnetic-insulating (AFM-I), ferromagnetic-insulating (FM-I), and ferromagnetic-metallic (FM-M) appear as x increases. In addition, three different charge ordered states exist as well. The transition temperatures of these phases are as shown. The different symbols represent the methods used to obtain the transition temperatures. Adapted from [44].

To produce a system with exchange bias, there must be a ferromagnet in addition to an antiferromagnet. For the purposes of our device, an ideal material is the conducting ferromagnet $La_{0.7}Sr_{0.3}MnO_3$ (LSMO), which exists as a perovskite oxide that is closely lattice matched to BFO. This material comes from a boarder class of materials known as the manganites, which consist of perovskite oxides of the form $AMnO_3$ (A=La,Ca,Ba,Sr,Pb,Nd,Pr). A large amount of research has been poured into the subsitutionally doped La manganites due to their incredibly rich phase diagrams and unique electronic and magnetic properties [44, 45]. Initial interest began in the 1950's when a barrage of experimental studies were done on $La_{1-x}A'_xMnO_3$ (A'=Sr,Ca,Ba), to map out different electronic and magnetic properties

as a function of x [46, 47]. One of the exciting things about these materials is that when doped the material becomes ferromagnetic and conducting, when the parent compounds are antiferromagnetic and insulating. Greater interest did not develop until the discovery of colossal magnetoresistance (CMR) in the manganites by Jin et. al. in 1994 [48]. It was shown that in doped manganites that upon application of magnetic field thousandfold changes in resistivity can occur. This lead to a huge push in experimental and theoretical research in these materials systems to both exploit and explain the CMR effect, starting a new renaissance for manganite materials.

Detailed studies of the electronic and magnetic properties of $La_{1-x}Sr'_xMnO_3$ reveal that in manganite systems, various interacting charge, spin and orbital degrees of freedom play a huge role in what properties the material shows. A full phase diagram for $La_{1-x}Sr_xMnO_3$ is presented in Fig. 2.3. It should be noted that within this phase diagram that while x=0 ($LaMnO_3$) and the x=1 ($SrMnO_3$) both exhibit insulating AFM states, with different doping levels several different magnetic and charge ordered phases start to emerge. There different charge ordered states appear at x=1/8,1/2, and 2/3, all corresponding to insulating states. The more technologically exploitable doping level is $0.2 \leq x \leq 0.45$, which corresponds to a ferromagnetic metallic state which has a high degree of spin polarization. For the purposes of our experiments a doping level of x=0.3 was chosen due to its higher than room temperature T_C (380 K) in bulk. This doping level is extremely well studied due to this fact and some of the relevant physics behind electronic transport is reviewed in the next section.

Electron Transport in $La_{0.7}Sr_{0.3}MnO_3$

Some of the first experiments with manganites already showed that transport in these materials was unique. Many conclusions were already being reached by researchers in the 1950's, such as a linear relationship between magnetization and magnetoresistance, showing a unique relationship between magnetism and electrical conductivity. AC measurements also showed that the material was extremely inhomogeneous and that it was likely made up of metallic grains surrounded by a high-resistance intergrain material. In addition, it was found that T_C of the material was directly related to the Mn-O-Mn bond angle, which is related to the different dopant species used. Depending on the different dopant species, different distortions could be induced in the lattice due to the difference in size of the ions. In the case of Sr, a smaller bond angle is induced which leads to higher T_C. After extensive study on this material system, it was concluded that the transport effects could be mostly explained by two effects: double exchange interactions between mixed valent Mn ions [49], and percolative phase separation providing an intrinsic inhomogeneity to the material [50].

To understand double exchange transport in manganites we must first examine the energy levels of the 3d electrons in Mn. Initially the states are five-fold degenerate, but due to O^{2-} surrounding Mn in an octahedral pattern a crystal field splitting occurs. The energy states are split into two different groups, the lower energy t_{2g} and the higher energy e_g (Fig. 2.4a). The three lower energy t_{2g} states are highly localized and do not contribute to conduction, but the higher energy e_g states do. If we look initially at the Mn^{3+} state and fill the

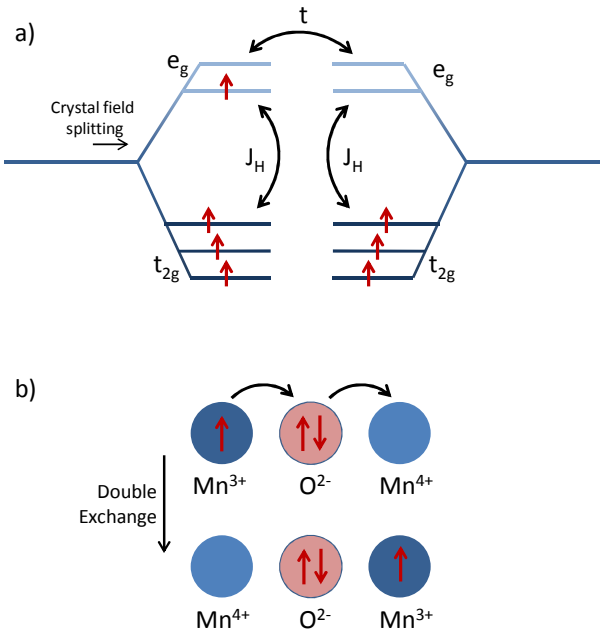

Figure 2.4: A depiction of the interaction energies involved in double exchange manganite systems. Energy levels are depicted in (a) with electrons occupying these levels (all spin up due to Hund's rules). A Hund's coupling term J_H and a hopping term t represent the interaction between e_g electrons and t_2g electrons and a hopping probability between neighboring Mn ions. A depiction of a double exchange "hop" mediated through an oxygen ion is depicted in (b).

energy levels using Hund's rules, we can fill all the t_{2g} states while leaving one in the e_g state, all with the same spin due to Hund's rules. An effective Hund's rule coupling, J_H, exists then between the t_{2g} electrons and the e_g electrons, favoring e_g spin alignment with the t_{2g} spins. In Mn^{4+}, only the t_{2g} states are filled. If we have a mixed valent system where Mn^{3+} and Mn^{4+} coexist, such as in doped $LaMnO_3$, the e_g electrons can hop from Mn^{3+} to Mn^{4+} through an intermediate O^{2-}. This process of simultaneously exchanging one electron from Mn^{3+} to O^{2-} while another electron is exchanged from O^{2-} to Mn^{4+} is known as double exchange hopping and is the primary mechanism for conduction in these systems (Fig. 2.4b). From these two mechanisms it can be seen that conduction is favored when the t_{2g} electron spins are aligned between neighboring Mn^{3+} and Mn^{4+} ions, and that the ferromagnetism in manganites is carrier mediated. Although beyond this simple model, the physics of manganites is significantly more complex, this double exchange model remains a cornerstone in the theory of magnetism and conduction in this system [51]. This model is used to partially explain the CMR effect, and the relation between magnetism and conductivity.

Another contributing factor to the interesting transport physics of manganites is the percolative phase separation that is intrinsic to the system. Many experimental groups now have confirmed the initial suspicions that manganites are highly inhomogeneous [50, 52, 53]. This is a result of the competition between the ferromagnetic conducting phase and antiferromagnetic charge ordered insulating phase that manifests itself as electronically phase separated regions at the nanoscale. In a single material, electronically inhomogeneous phases can coexist in a percolative nanoscale network that changes with temperature and magnetic field, thus making transport measurements in this material difficult (e.g. Hall effect). This effect contributes to the unique transport mechanisms in manganites and also is believed to contribute to the physics of CMR behavior.

Although we are primarily only concerned with exchange bias in a BFO/LSMO system, clearly the many degrees of freedom (charge, spin, orbital, lattice) between the two different highly correlated materials BFO and LSMO are extremely unique. The interaction between the two materials at an artificially created heterointerface will also allow for interesting exploration of the physics of complex oxide material systems.

2.3 $BiFeO_3/La_{0.7}Sr_{0.3}MnO_3$ Heterostructure Growth and Characterization

Growth of $BiFeO_3/La_{0.7}Sr_{0.3}MnO_3$ Heterostructures

To grow high quality BFO/LSMO heterostructures a process known as pulsed laser deposition (PLD) [54] is employed with reflection high-energy electron diffraction (RHEED) to monitor growth [55]. In this process a high energy laser is used to ablate material from a target which epitaxially deposited onto a substrate. To monitor the growth process in-situ, a high energy electron bean ($\sim$20 keV) is used to strike the growth surface at a grazing angle of 1-5° and the reflected beam is analysed by a detector. A highly surface sensitive diffraction pattern is formed due to the interaction with the electron beam and the crystal lattice.

The process begins with the preparation of the substrate. Chosen because it is closely lattice matched to both LSMO and BFO, a 5x5 mm^2 sample of $SrTiO_3$ (STO) (001) is treated by first wet etching in a buffered HF solution followed by a thermal anneal to obtain a fully TiO_2 (B-site)-terminated surface [56]. This interface engineering is highly important in this process, since highly different interface properties can arise from growing LSMO or BFO on the opposite termination. LSMO and BFO were then epitaxially grown using the previously described method, at a laser energy density of 1.5 J/cm^2 at a repetition rate of 1 and 3 Hz, respectively. The substrate was held at 700° C in an oxygen ambience of 200 mTorr and 100 mTorr, for LSMO and BFO respectively. RHEED was used to continuously monitor the growth process to ensure layer-by-layer growth, where atoms coalesce together in one atomic layer until that layer has been filled before starting growth on the next layer. This can be observed as oscillations in the RHEED diffraction pattern. Initially a smooth

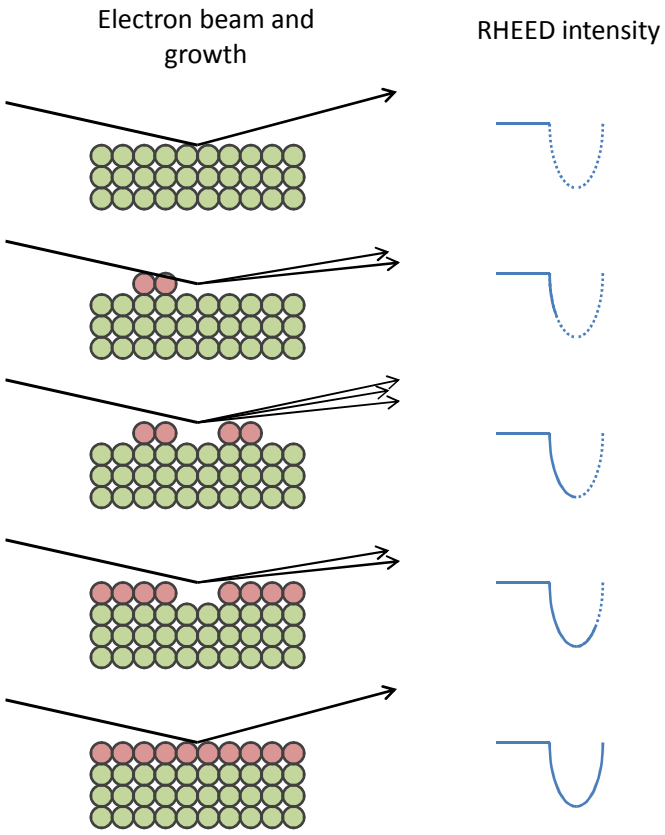

Figure 2.5: An example of RHEED oscillations with respect to layer growth in layer by layer growth. The RHEED signal is reduced due to the increased scattering when a non-complete layer is formed, and increases again after the layer is complete.

surface exists and the diffraction pattern is at a local maxima. As the next layer starts to grow the surface gets rougher and the signal decreases, until a local minimum is reached. The signal starts to rise again and returns to the next local max when the next layer is completed. This is schematically shown in Fig. 2.5. By viewing these oscillations, it is possible to precisely control the thickness of the film down to the unit cell level. Oscillations for a typical BFO/LSMO heterostructure growth process is shown in Fig. 2.6. Here we deposit 8 u.c. (3 nm) of LSMO before moving onto BFO, where there is a quick transition from layer-by-layer growth into a step flow growth regime where RHEED oscillations die out. Here, 3 nm was chosen so that exchange bias effects at the interface will dominate when probed with electrical transport measurements. BFO is then deposited for 3 hours at the rate previously mentioned, which typically results in a film of $\sim$200 nm. This thickness is necessary to prevent pinhole defects from forming within BFO, which will later affect the ability to gate the material. After the growth process the heterostructure is cooled to room

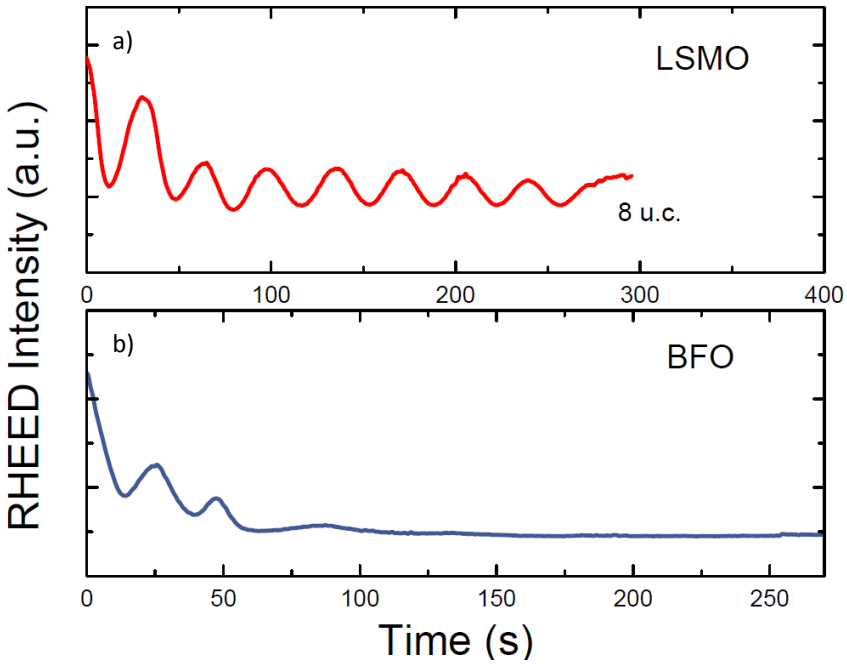

Figure 2.6: RHEED oscillations for a typical BFO/LSMO heterostructure.

temperature at an oxygen ambience of 760 Torr at a rate of 1° C/min, which is necessary to ensure full oxygenation of the sample.

Ferroelectric characterization

Using piezoresponse force microscopy (PFM) we can image the ferroelectric domain structure of these BFO/LSMO heterostructures. This method is a variant of atomic force microscopy that allows for the imaging of ferroelectric domains at the nanoscale. Using a sharp conductive probe, a AC voltage is used to excite a response from the underlying ferroelectric surface. The resulting deflection is the detected and corresponds to ferroelectric polarization. By measuring both lateral and vertical deflection both in-plane (IP) and out-of-plane (OOP) ferroelectric polarizations can be mapped.

Since the ferroelectric polarization vector in BFO lies along the body diagonal in {111}, there are 8 possible variants corresponding to vectors pointing to any of the 8 cubic corners. By imaging the sample along the [1-10] direction we can obtain contrast between the two OOP components and three IP components (left and right polarizations have no contrast). Displayed in Fig. 2.7, is both the IP and OOP ferroelectric domain structures on a BFO/LSMO heterostructure where a conducting AFM tip has been used to locally switch ferroelectric polarization from up to down. The polarization in BFO was both stable and

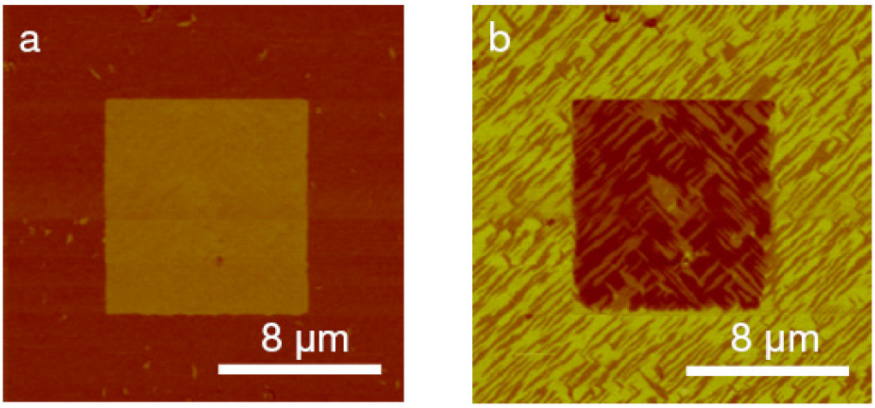

Figure 2.7: Both out of plane (a) and in plane (b) ferroelectric domain structure as obtained from piezoresponse force microscopy. The center region has been poled into the down polarization state using a conducting AFM tip.

switchable and shows stripe like domains IP whether polarization is up or down OOP.

Magnetic characterization

To measure the magnetic properties of the grown heterostructures a Quantum Design MPMS SQUID magnetometer was used. Here we can characterize the exchange bias in BFO/LSMO heterostructures before any fabrication has been done. By applying a magnetic cooling field of ± 1 T, we can observe exchange bias in the most canonical sense by observing a shift in the M-H curve. Shown in Fig. 2.8a are the M-H hysteresis curves of a typical BFO/LSMO heterostructure at 7 K cooled with opposite magnetic fields showing exchange bias shifts of 225 Oe in either direction. Additionally, a similarly grown sample with a 2 nm STO spacer between BFO and LSMO was also measured under the same field cooling procedure and resulted in a M-H curve without exchange bias (Fig. 2.8b). It appears from these measurements that exchange bias does indeed exist in BFO/LSMO heterostructures and the effect is very dependent on the interface between BFO and LSMO. Additionally, temperature dependent measurements show that exchange bias only starts to occur at $\sim$100-120 K despite field cooling from room temperature. This type of behavior is normal in many exchange bias systems, where the onset of exchange bias occurs at some blocking temperature T_B that does not equal either T_C nor T_N.

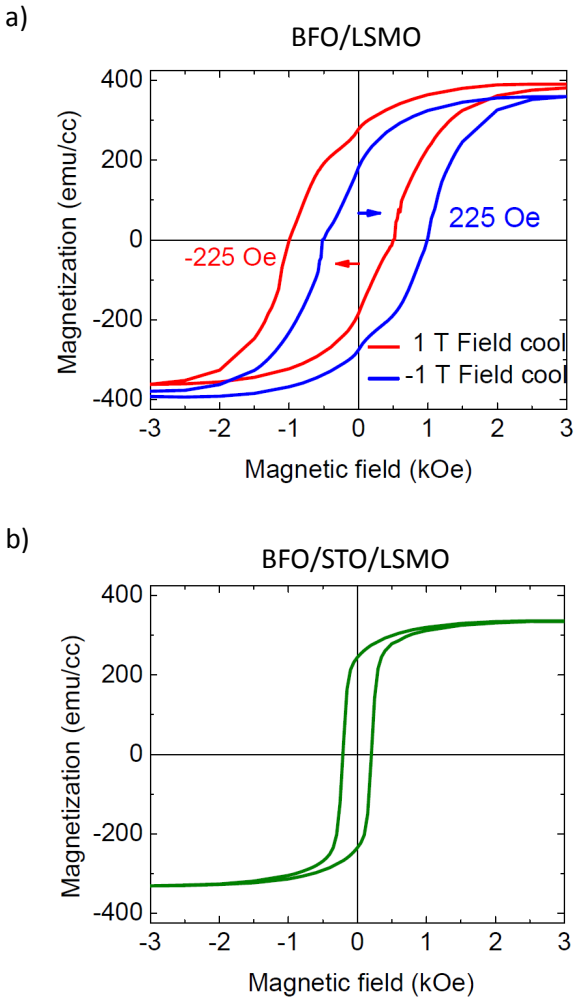

Figure 2.8: SQUID magnetometery measurements of exchange bias after ±1 T field coolings of BFO/LSMO heterostructures are presented in (a). The corresponding magnetometery measurement with a 2 nm STO spacer shows no exchange bias in (b).

2.4 Emergent Interfacial Phenomenon in $BiFeO_3/La_{0.7}Sr_{0.3}MnO_3$ Heterostructures

Measurements have been done using x-ray spectroscopy techniques by Yu et. al. that shed light on some of the interfacial interactions that cause exchange bias in BFO/LSMO systems [57]. In exchange bias systems, symmetry in the magnetic hysteresis curve is broken due to pinned unrotatable spins in the AFM. A few of the major questions that arise when dealing

with exchange bias in BFO/LSMO are the origin of these pinned spins and how they interact at the interface. Since BFO is strongly G-type antiferromagnetic, the spins in the (100) plane are compensated, meaning they have no net magnetic moment (Fig. 2.9), it is therefore not immediately obvious where the pinned spins necessary for exchange bias arise from.

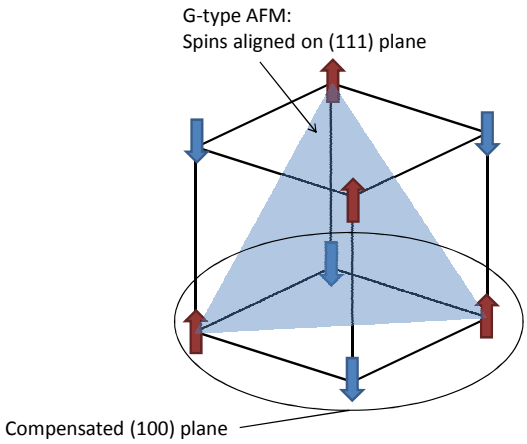

Figure 2.9: BFO spin structure is depicted here. G-type antiferromagnetism occurs in this system, and leaves the (100) plane magnetically compensated.

To answer these questions it is necessary to directly probe the spin structure at the interface of this system. X-ray absorption spectroscopy (XAS) is the perfect tool to do this with. By obtaining XAS spectra while recording the total electron yield (TEY) current as a function of x-ray photon energy, highly element specific information about the transition metal spin structure at the interface can be obtained. A technique known as x-ray magnetic circular dichroism (XMCD) can be used to examine the magnetic properties of individual transition metal ions at the interface by examining the differences between the absorption spectras of left and right circularly polarized light [58]. This is due to the spin-orbit coupling of the electrons in the sample and the fact that left and right circularly polarized x-rays carry different angular momenta resulting in different absorption cross sections. The sign of the XMCD signal gives information about the direction of the spin, while the amplitude gives information about the magnitude of the magnetization. In BFO/LSMO heterostructures it was found that a spin structure that is highly different than that of the bulk is formed at the interface between BFO and LSMO. Data from XMCD measurements show that at the interface a unique magnetic state is formed exhibiting magnetization of $\sim$0.6 μ_B/Fe, which is 20 times larger than the nominal value in non-interfacial BFO (0.03 μ_B/Fe). Temperature dependent measurements of this magnetic interface state show that the onset of interface magnetism corresponds directly to the onset of exchange bias (Fig. 2.10). It is likely that

in this magnetically compensated system that the unique magnetic interface state is contributing the pinned unrotatable spins necessary for exchange bias. Further work by Yu et. al. show that the origin of this interface state involves orbital ordering of the interfacial Mn and Fe. Additionally, it was also found from the sign of the XMCD signal that the coupling at the interface between interfacial Mn and Fe was antiferromagnetic in nature.

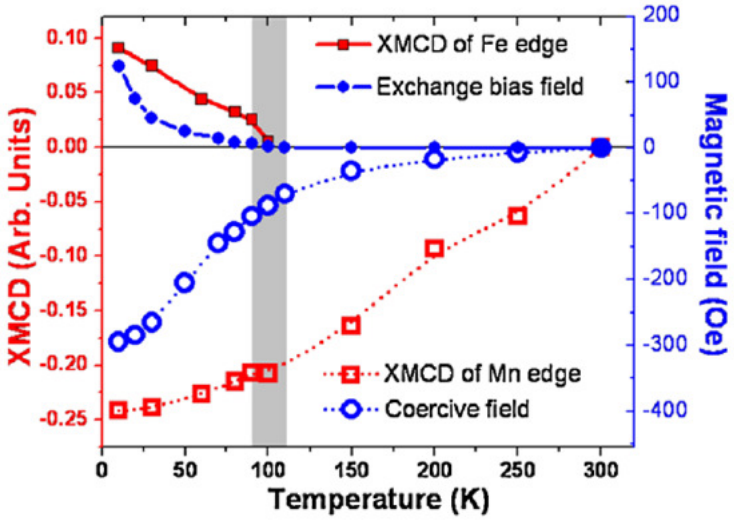

Figure 2.10: Temperature dependent XMCD data on both Fe and Mn is presented in this figure. The uniquely large interface magnetism arises at the same temperature as exchange bias as measured using SQUID magnetometery. The magnetism in Mn as measured through XMCD roughly behaves in the way expected, and arises as soon as the LSMO film becomes magnetic. Adapted from [57].

One drawback of doing x-ray spectroscopy measurements on large unpatterned as-grown heterostructures is that in this experiment it was not possible to switch the polarization of the BFO. A huge remaining question is, by changing BFO polarization is it possible to manipulate this interface state to control exchange bias? In the remainder of this thesis we answer this question by using fabrication techniques to build a switchable field effect device out of the bulk heterostructures, the topic of the next chapter.

Chapter 3

Device Design and Fabrication

3.1 Multiferroic Field Effect Device

After growth it is important to pattern the heterostructure into a device configuration. Unpatterned thin film heterostructures have their inherent limitations on experimentation and applicability. Due to the large area of the films grown for this thesis work (5 mm x 5 mm), it was not practical to ferroelectrically switch the entire BFO thin film. This is due to the number of pinhole defects per unit area in the BFO dielectric, which limits the size of the top electrode. This is partially obviated by the use the a conducting AFM tip to locally switch ferroelectric polarization of BFO, but to do this repeatedly on a large scale would be impractical. To more carefully examine the effects of BFO polarization on exchange bias here we design and fabricate a multiferroic field effect device with a patterned conduction channel and top electrode gate. By patterning smaller gate electrodes we are able to reliably and repeatedly switch BFO polarization by only having to apply a gate voltage pulse. In addition, by creating a device with the same device architecture as a traditional field effect transistor, we create a scalable magnetic device already ready for applications. Due to the patterning of the material into small area field effect devices, the bulk magnetometery techniques used in the previous section cannot be used, and because of this we use magnetotransport to measure the electronic and magnetic properties of the LSMO channel upon gate switching. By using this technique we are measuring only the relevant LSMO layer beneath the gated BFO, thus providing more direct information about the magnetic properties of LSMO that are changing upon gating.

The device is shown schematically in Fig. 3.1. Devices were patterned with the conduction channel both in the [100] (Fig. 3.1a) and the [110] directions (Fig. 3.1b) relative to the STO substrate. A conventional hall bar geometry was chosen for this device but with a BFO dielectric and Au top gate electrode over the center. Using this device geometry we can easily measure the resistance of the channel using a four-point probe method by inputting current and then measuring V_{MR} (Fig. 3.1b). Magnetoresistance measurements can be performed by applying an external magnetic field in either the [100] or [010] directions, depicted as B_x

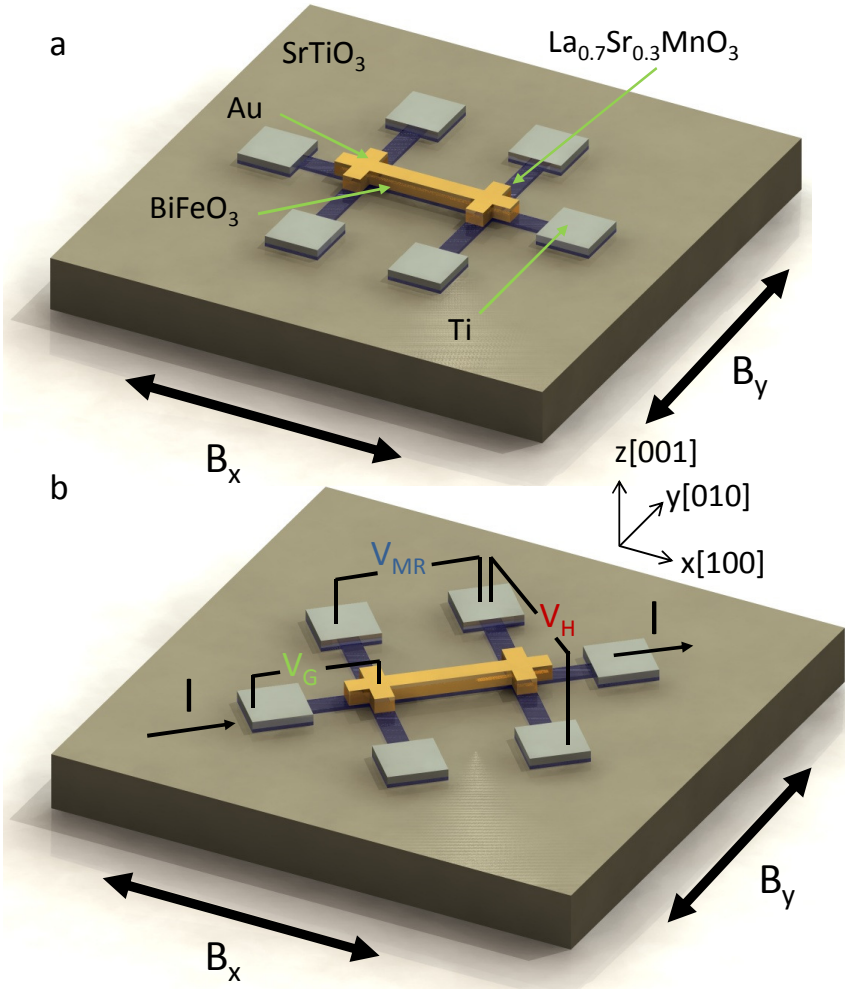

Figure 3.1: A schematic depiction of a fabricated BFO/LSMO field effect device in a gated hall bar geometry. In (a) current goes in the [100] direction, while in (b), the current goes along [110]. Voltage pulses (V_G) are applied to the Au top gate electrode to ferroelectrically polarize BFO and the four point magnetoresistivity of LSMO is measured under applied fields in both the x and y directions.

and B_y in Fig. 3.1, respectively. By changing the applied magnetic field to the out of plane direction [001], or B_z, the Hall effect can be measured by inputting current and measuring V_H (Fig. 3.1b). Using these two techniques, information about the magnetic and electronic properties of LSMO can be deduced, and the effect of BFO polarization on these properties can be observed. The following sections of this chapter provide a guide for the fabrication steps and techniques used in creating this device.

3.2 Fabrication Process

Through careful engineering, a reliable process was developed for the fabrication of BFO/LSMO multiferroic field effect devices. Each step of the process is outlined in Fig. 3.2, which provides a summary of the entire process. As described in the previous chapter, we start with a high quality 5x5 mm^2 heterostructure sample of BFO (200 nm)/LSMO (3 nm) grown on (100) STO. The first step is to put down a top electrode for the gate, since the LSMO channel doubles as the bottom electrode for the ferroelectric. Here we use thermal evaporation to uniformly put down a gold top electrode over the entire chip (Fig. 3.2a). Next, using photolithography and argon ion milling the channel is patterned by etching the entire film down to the substrate (Fig. 3.2b). Using a second photolithography and ion milling step, the gate is patterned so that the gold top electrode remains only on the portion of the device that is measured through magnetotransport (Fig. 3.2c). A lift-off process was used to pattern titanium that was deposited using e-beam evaporation for contact pads (Fig. 3.2d). Finally, the entire device is annealed for 2 hours at 250° C to heal oxygen defects induced through the previous processing steps.

3.3 Gate Electrode Deposition

Using a modified Varian 3118 thermal deposition system, top electrode contacts were thermally evaporated onto as grown BFO/LSMO heterostructures. The 5x5 mm^2 chips were mounted onto a 4 in copper dummy wafer using vacuum grease and loaded into the vacuum chamber using a custom made holder. The chamber was then pumped to $<2 \times 10^{-6}$ Torr, and 2 nm of titanium was deposited at a rate of 0.05 nm/s as measured by a quartz crystal microbalance. The Ti layer served as an adhesion layer between the gold and oxide. Then, without breaking vacuum, 200 nm of gold was deposited at a rate of 0.5 nm/s. The largest mechanism for failure in BFO capacitor type devices are the pinhole defects that cause shorts through the oxide. One way to limit this type of failure mode is by growing a thick BFO film to reduce the areal density of defects that reach the underlying LSMO. Another is reducing the area of the gate such that there is a reduced probability of encountering a defect. Empirically we have found that using a non-reactive noble metal with a large atomic radius also decreases the chances of pinhole shorts in devices. This is especially relevant after

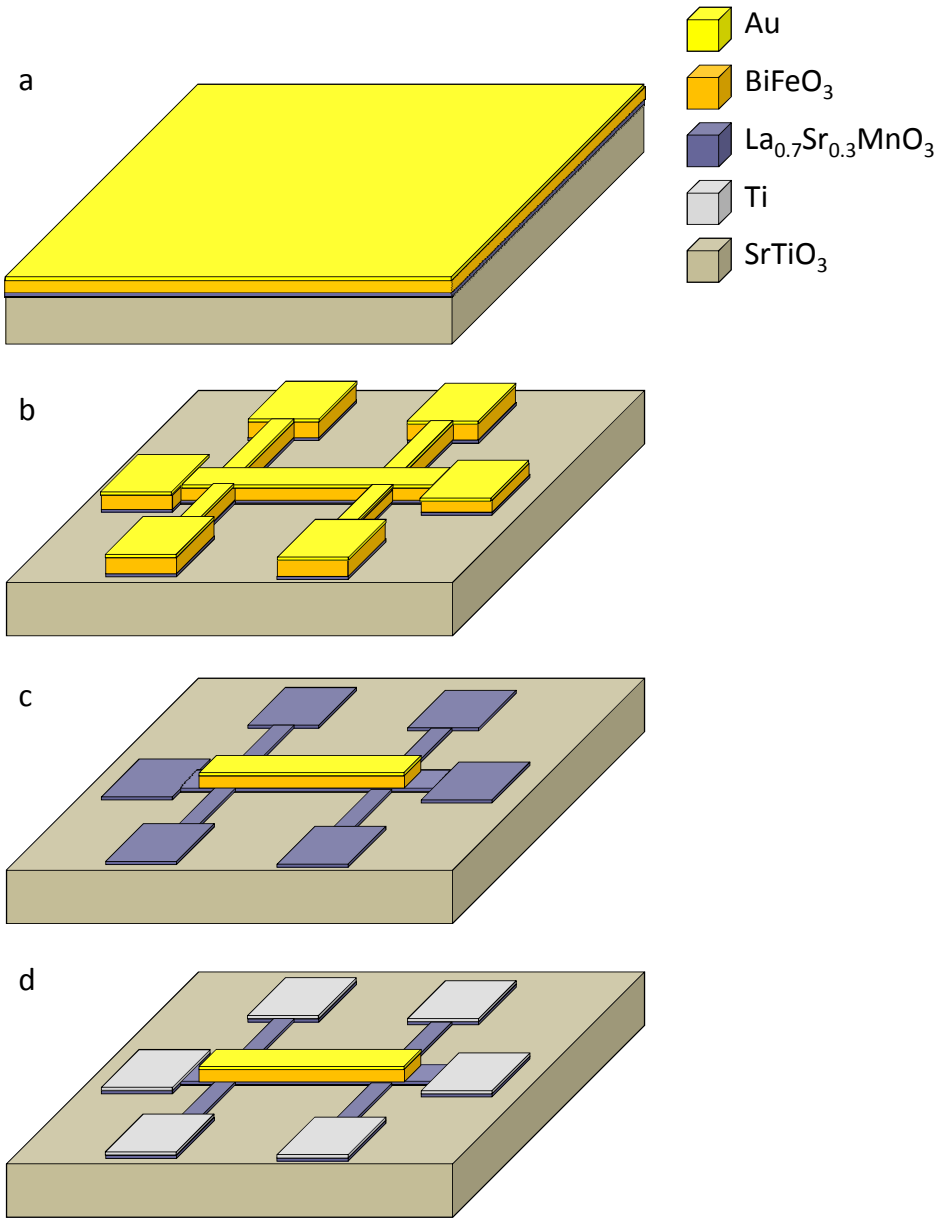

Figure 3.2: A depiction of each step in the device fabrication process. (a) Thermal deposition of gold for the gate top electrode. (b) Photolithography and ion milling to define the LSMO channel. (c) Second photolithography and ion milling step for the definition of a gate electrode. (d) Electron beam deposition and lift-off process for Ti contact pads.

an annealing process which increases the chances that metallic ions diffuse through pinhole defects to create shorts. For these reasons, a gold gate electrode was chosen.

3.4 Photolithographic Patterning and Mask Design

All the patterning steps done were done through contact photolithography using a JBA contact mask aligner. Since there were three separate patterning steps, three masks were designed and shown in Fig. 3.3. Five separate devices were designed to be linked together so a common input current could be used. Each device was also designed to have four separate voltage probes to measure either magnetoresistance or hall effect, depending on the applied magnetic field direction and the choice of voltage probes. Each device has its own gate electrode, which was designed to have the smallest area (80 x 80 μm^2) to reduce gate leakage, but still remain bondable by an ultrasonic wire bonder. Additionally, ferroelectric test capacitors were included on each device to serve as a check of the ferroelectric properties of the BFO. Three separate masks were designed for each of the patterning steps needed, as mentioned previously. The first mask (Fig. 3.3a) involves the overall pattern, and only masks the portion of the material which is not to be etched away through ion milling. The second mask (Fig. 3.3b), protects the gate electrode on the second ion milling step that removes the gold from the areas of the device not under measurement. The third mask (Fig. 3.3c) is a metallization mask for our lift-off process to pattern Ti contact pads. Alignment marks in each mask allow for realignment after each step. All masks were patterned on 2.5" chrome masks on soda lime, using a GCA 3600 Pattern Generator.

To pattern using the mask aligner, FujiFilm OCG 825 (G-line) photoresist was spun at 4000 rpm for 40 s on the standard 5 x 5 mm^2 chips. Samples were then soft baked for 3 min at 90° C to remove solvent from the resist. Using the mask aligner, samples were then exposed for 12 s using the previously mentioned masks at 12.5 mW/cm^2. Samples were then developed in Shipley MF-319 developer for 12 s, rinsed with deionized water to stop development, and blown dry with compressed nitrogen. After development, the samples were typically hard baked at 120° C for a minimum of 5 minutes to harden the resist for the next processing step. This baking causes cross-linking of the polymers in the photoresist, which increases its resistance to etchants.

3.5 Argon Ion Milling

Ion milling has become the standard etch process for oxide systems, since wet etch and other dry etch recipes (like reactive ion etching) typically do not etch oxide systems well. This sputter etching process involves subjecting the sample to a monoenergenic beam of ions (usually an inert gas like Ar) which physically sputters off the material. Since there is no chemical reaction in this process, it is effective to a wide range of different materials including oxides. Typically using either a DC or RF source, a plasma is created by ionizing

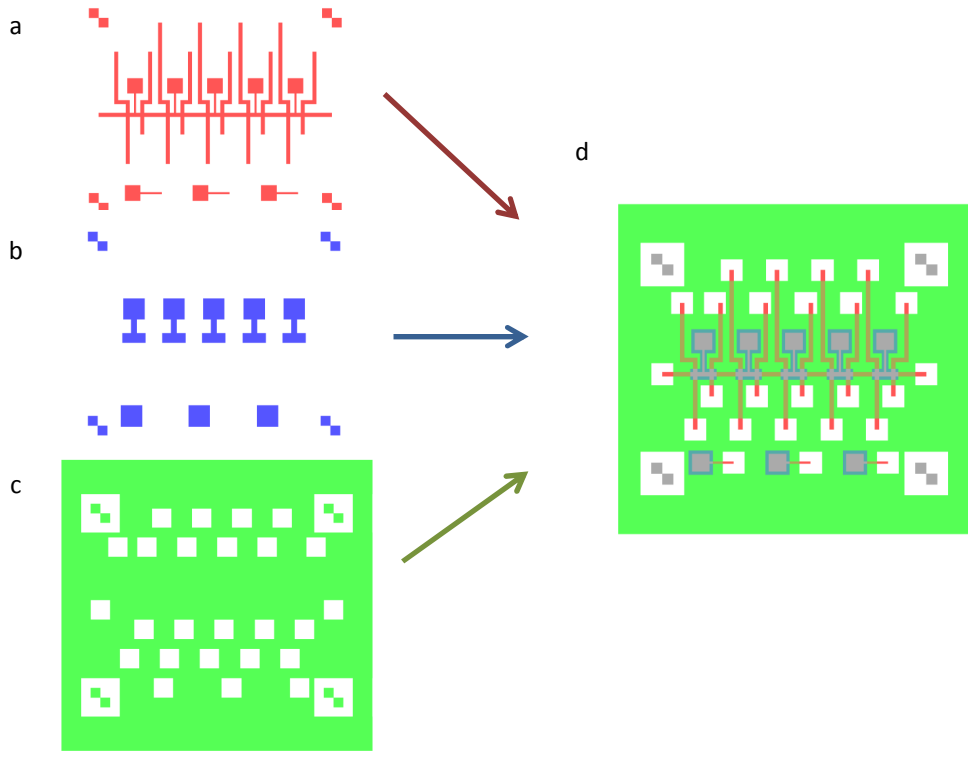

Figure 3.3: The set of three photolithographic masks used in device fabrication. The first mask is used to define the channel (a), the second mask is used to define the gate electrodes (b), and the final mask is used in a lift off process to define contact pads. In (d) all three masks are overlayed to show how each individual mask aligns with the others.

the process gas in a discharge chamber inside the ion gun. The ions are then accelerated and focused using a set of grids placed above the discharge held with a potential difference. Typically a neutralizing filament sits outside the ion gun and provides excess electrons to maintain a charge balance in the plasma as it leaves the gun and is sent towards the sample.

In our process we use a custom built cryogenic ion milling system with a 3.5 cm Kaufmann ion source, an Ion Tech MPS 300 FC power supply, and a liquid nitrogen cooled sample stage. Samples were attached to a copper plate using vacuum grease and the copper plate was attached to the liquid nitrogen cooled stage using vacuum grease and copper clips. The chamber is typically pumped down to $<1 \times 10^{-}6$ Torr before liquid nitrogen is forced through copper coils attached to the sample stage through a pressurized dewar. After a 5 minute precooling step, the chamber is filled with argon gas through a variable leak valve and was held at 2×10^{-4} Torr. The ion mill power supply was then turned on to ignite the plasma and accelerate the beam. The ion mill was run typically with a beam current of 10 mA with an beam voltage of 600 V and an accelerating voltage of 250 V. A shutter was used to

mask the sample every 15 minutes for 5 minutes to decrease heating from the neutralizing filament. This process results in a gold etch rate of ∼20 nm/min and a BFO/LSMO etch rate of ∼4 nm/min. Since the total thickness of the BFO/LSMO heterostructure is not typically a well known value, visual inspection is typically used to determine the etch stop. By viewing through a glass window, it is clear when the etch has reached the substrate as the sample turns clear in areas not covered by photoresist. Since the first ion milling step involves removing all the material down to the substrate, but the second ion milling step involves leaving the LSMO layer intact, the second milling step is timed to be less than that of the first.

Ion damage induced oxygen vacancies

One well known problem with using ion milling as an etch is the creation of defects at the surface during milling. In oxide materials ion milling produces a large number of oxygen vacancies at the surface, which negatively affect its electronic/magnetic properties [59, 60]. The largest source for concern in our process is the creation of oxygen vacancies in the STO substrate. Nominally STO is a band insulator with a band gap of 3.25 eV, but even low amounts of doping from cation-substitution (La for Sr, or Nb for Ti) or oxygen vacancies can induce metallicity at the surface [59, 61, 62]. It has been shown that doping levels as low as 2.7 x 10^{17} cm^{-3} can cause STO to change from insulating to conducting [63]. This results in a large problem for the fabrication of devices on STO substrates.

During the etch process, ions are removed from the surface of the sample due to sputtering. If every ion was equally diffusive there would be no more oxygen defects than any other ion species at the surface, but this is not true. Oxygen, due to its small size and closer spacing in STO, is significantly more mobile than Ti and Sr. Because of this fact, as oxygen is sputtered off the surface of the sample, oxygen from beneath the surface will diffuse up and fill the space causing an oxygen deficient layer beneath the surface. Typically these defects occur deep enough that they are created faster than they can be etched away by the ion beam, and therefore a metallic surface layer is created in the substrate [59].

We employ two methods to counteract these effects. First, we lower the diffusion rate of oxygen by lowering the temperature during etching by using a liquid nitrogen cooled stage. This significantly reduces the number of oxygen vacancies created, and leaves the remaining defects very close to the surface. Second, after all other processing steps are performed, a 2 hr O_2 anneal at 250° is used to heal the remaining surface defects. After this process, by all discernable measurements, the STO substrate is insulating and has no adverse effects on device performance.

3.6 Channel Contact Metallization

One of the final steps to the device fabrication process is to make ohmic contact to the underlying LSMO channel. Ohmic contacts are defined as making a contact to a device

that is non-rectifying such that the current-voltage (IV) curve is linear and antisymmetric with minimal contact resistance. This is in contrast to a Schottky barrier contact that has a non-linear rectifying diode-like IV, which is due to band bending at the interface between the contact metal and the device. Making ohmic contact to LSMO is not necessarily an easy prospect due to the fact that the thickness of LSMO is only 3 nm, and the only direct point of exposure is at an edge of an ion milled mesa with BFO covering it. Direct wire bonding with Al wire at the edges of these mesas produces unsatisfactory contacts with highly nonlinear IV characteristics and high contact resistance.

Here we exploit two techniques to resolve the contact issue. Since wire bonding at the edge of the mesa creates undesirable contacts, we attempt to make contact through the top of the mesa by taking advantage of the leaky dielectric properties of BFO. The second ion milling step now has a dual purpose, both to remove the gate electrode from the non-relevant areas of the device and also to thin the BFO on top of the LSMO. By thinning the BFO layer we increase the chance of making contact by diffusing metal ions through pinhole defects. Another mechanism that helps us to make contact is to exploit the effect that ion milling has on the STO substrate. By inducing metallicity in selective areas of the device substrate, we can attempt to make contact to the LSMO from the bottom of the mesa. To accomplish all of this we initially thin down the BFO as much as possible in the second ion milling step when the gate electrode is removed, and pattern, using photolithography, a new layer with only a contact area exposed. Now the sample is placed back into the ion mill system and milled with the same parameters as described in the previous section for 2 minutes but without liquid nitrogen cooling to induce oxygen defects that cannot be annealed out. Without breaking vacuum 100 nm of Ti is deposited at a rate of 0.1 nm/s on the sample using a custom installed MDC e-Vap electron beam deposition system designed into the same vacuum chamber as the ion mill. Finally, the photoresist is lifted off by using acetone and ultrasound, to reveal the finished contact pads. By choosing a metal with a small ionic radius and sending the entire chip through the final annealing step, the likelihood of making good metallic contact through the BFO dielectric is greatly increased. Applying a direct Al wire bond to the contact pads now creates contacts that are highly linear and have low contact resistance at all temperatures measured (4-400 K).

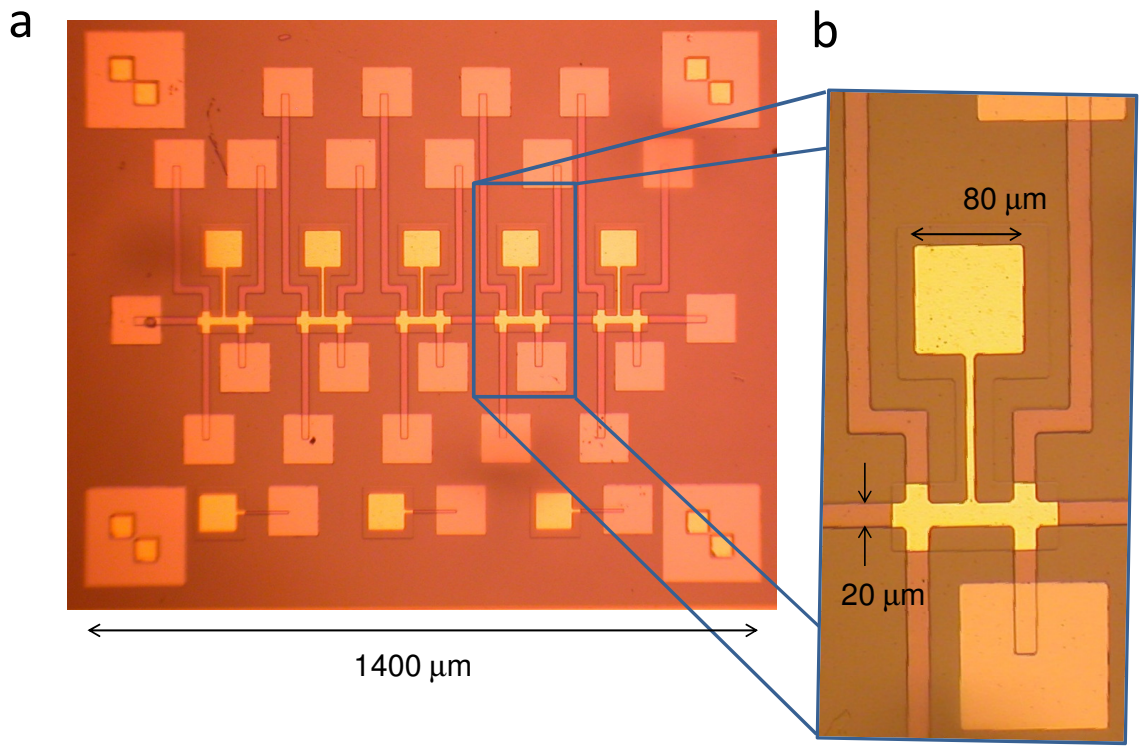

Figure 3.4: A optical micrograph of the finished device.

Chapter 4

Device Characterization and Measurement

4.1 Measurement Setup

To characterize and perform magnetotransport measurements on our device, a custom built cryogenic measurement system was used. Fabricated chips were mounted using silver paint into the pocket of a 16-pin plastic leaded chip carrier (PLCC). Samples were carefully mounted to ensure that devices were aligned to the chip carrier edge so that the applied magnetic field would be applied along either the [100] (B_x) or [010] (B_y) directions relative

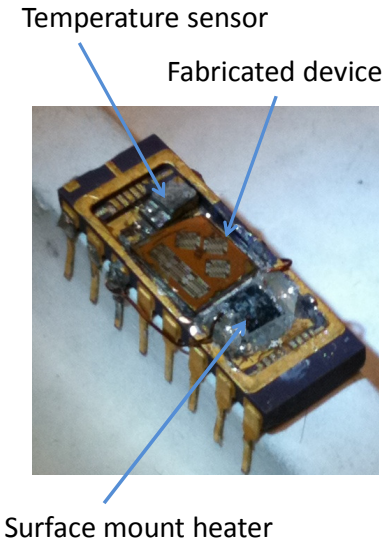

Figure 4.1: A photograph of the PLCC chip carrier used in magnetotransport experiments.

to the crystal. Along with the device, a Lakeshore Cernox thermometer (CX-1050-SD) was mounted near to the sample using epoxy for temperature sensing. A Cernox type thermometer was used for its accuracy and relative insensitivity in magnetic fields, with less than a 0.15% deviation from actual temperature at 8 T. Opposite the thermometer, a 50 Ω surface mount resistor was soldered directly to the legs of the chip carrier and mounted into the pocket using epoxy to serve as a local heater. By using the surface mount resistor as a heater and the Cernox thermometer as a sensor, temperature control could be performed using a Cryocon Model 44C temperature controller. Temperature in this system could be controlled to within 0.0001 K using this method. A picture of the chip carrier is displayed in Fig. 4.1. Using an ultrasonic wire bonder, electrical contacts were made from the terminals of the chip carrier to the devices using 0.7 mil (∼18 microns) Al wire. Extra care was taken when making contact to the gate electrode to prevent the shorting of the gate to the channel by having a bond land to the edge of the Au gate pad, or breaking through the dielectric completely by using excessive ultrasonic power. Also anti-static grounding straps were used to ensure electrostatic discharge from human contact did not cause dielectric breakdown in any of the devices.

After wire bonding the samples, the chip carriers were loaded into a custom built cryogenic dip probe (Fig. 4.2). This probe was built using stainless steel tubing and designed to be used under vacuum. At one end of the tubing there is one hermetically sealed 19-pin LEMO connector for electrical feedthroughs and a vacuum port for probe evacuation. A thermocouple vacuum gauge and a low pressure blow off valve is also mounted at the top of the stainless steel tubing. On the other end, a copper block is attached to the tubing with a 16-pin PLCC socket mounted for the chip carrier to be inserted into. Through the tubing of the probe, twisted pair manganin wire was used to connect the socket to the LEMO feedthrough. Depending on the experiment, magnetic field may be applied in different directions by mounting the sample with or without a 16-pin 90° socket adaptor such that the device can be rotated from the default [001] B_z direction to either the [100] B_x or [010] B_y directions. The entire lower portion of this probe is then encased in a cylindrical brass jacket that is sealed using Wood's metal solder to a brass ring welded to the outside of the stainless steel tubing, allowing for the probe to be pumped down to high vacuum conditions. Typically, measurement preparation involves placing a wire bonded sample into the 16-pin socket, sealing the probe using Wood's metal solder, and pumping the probe using a turbo pump based pump station to ∼1 x 10^{-5} Torr. The probe is then backfilled with 30 mTorr of helium gas to serve as a thermal exchange gas. Using this method temperature could be controlled using a temperature controller from 4.2 K to ∼300 K. A picture of the probe with the chip carrier attached in a 90° socket adaptor is presented in Fig. 4.2.

Following sample loading, the probe is precooled to 77 K in a handheld liquid nitrogen dewar before being inserted into a custom superconducting magnet. We use a Cryogenic Consultants 10.5 T superconducting magnet, recently fitted with a new top flange with several hermetically sealed electrical feedthroughs for temperature and liquid helium level sensing. The magnet is housed in a newly designed custom built liquid helium dewar constructed by Kadel Engineering. The magnet is powered by a Cryomagnetics 4G Bipolar

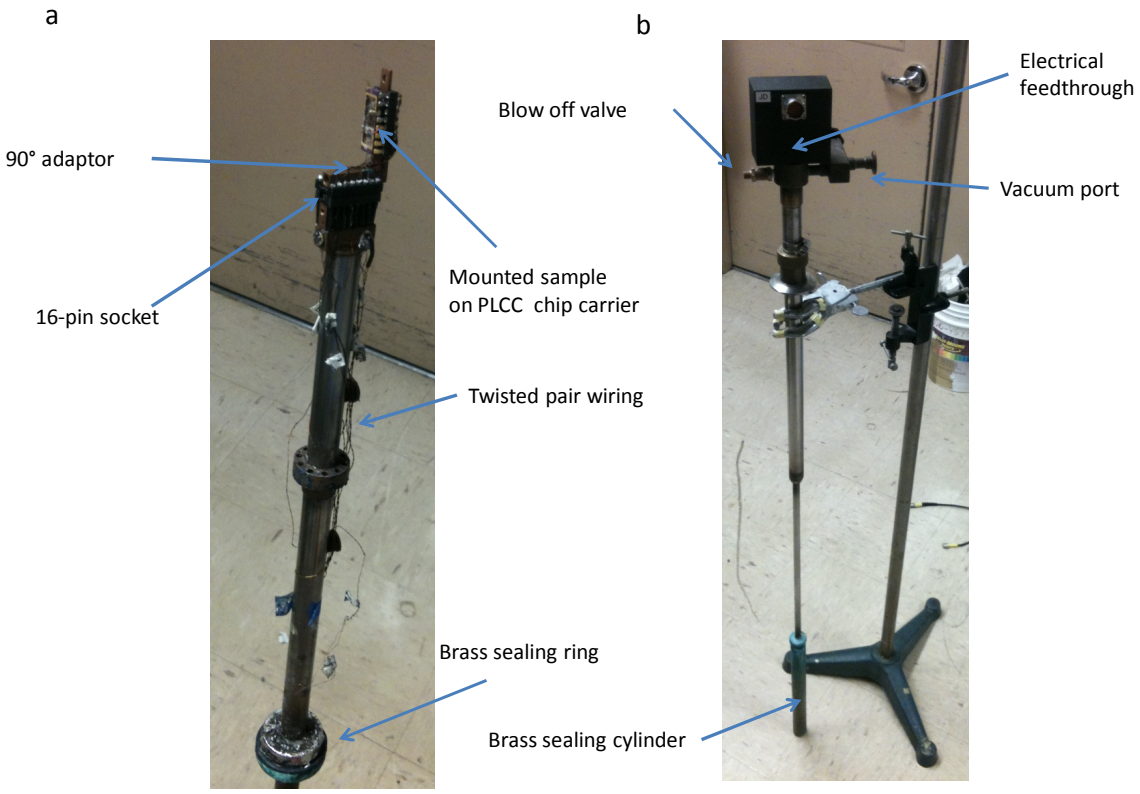

Figure 4.2: A photograph of the cryogenic probe used in magnetotransport experiments. (a) shows the probe with the encapsulating brass cylinder off, and (b) shows the probe after being sealed using Wood's metal solder.

superconducting magnet power supply, which was needed for smooth continuous sweeping of the magnetic field through zero. A 0.01 Ω shunt resistor was attached in series to the magnet and tapped off to measure the magnet current. This value was then then converted to magnetic field based on the original manufacturers calibration. When inserting the probe into the magnet, extra care was taken to ensure that the sample always sat at the center of the magnet where the original field calibration was done. This was accomplished by fitting a hose clamp to the top of the probe marking the position the probe sits when the sample is centered. A photograph of the magnet assembly is presented in Fig. 4.3.

4.2 Magnetotransport

Using the system described in the previous section, magnetotransport measurements can be performed on our devices. The simplest magnetotransport measurement that can be done is to measure the resistance of the LSMO channel as a function of applied magnetic field,

Figure 4.3: A photograph of the superconducting magnet system used in magnetotransport experiments in a custom designed liquid helium dewar.

known as magnetoresistance (MR). Since devices were built with the conduction channel both in the [100] direction and in the [110] direction and magnetic field can be applied in both the [100] (B_x) and [010] (B_y) directions, this allows for four different measurements of magnetoresistance (Fig. 3.1). As we will see in a later section, these different configurations correspond to different device behaviors. A four-point probe method was used to measure the resistance of the channel as depicted schematically in Fig. 4.4. A function generator was used with a bias resistor to current bias the device. Both the voltage across the channel and the voltage across a current measuring resistor in series with the device were fed into separate Ithaco Model 1201 low-noise voltage preamplifiers, which were then lock-in detected using two separate Signal Recovery Model 7265 lock-in amplifiers. This gives two highly sensitive measurements of both current and voltage through the device, thus allowing us to determine the resistance. It was necessary to obtain a measure of current despite current biasing the device due to the phase separated nature of the LSMO channel. Subtle changes in the percolative resistive network in an area of the channel that is not measured by the voltage probes could cause tiny jumps in current that manifests itself as tiny jumps in the voltage of the measured device. If a static bias current is assumed, then these current fluctuations cause our calculated resistance to have tiny jumps as well, when in fact no change has occurred in the area of the device under measurement since the tiny jumps in voltage are related to the tiny jumps in current. Also, it was necessary for each lock-in amplifier to perform a

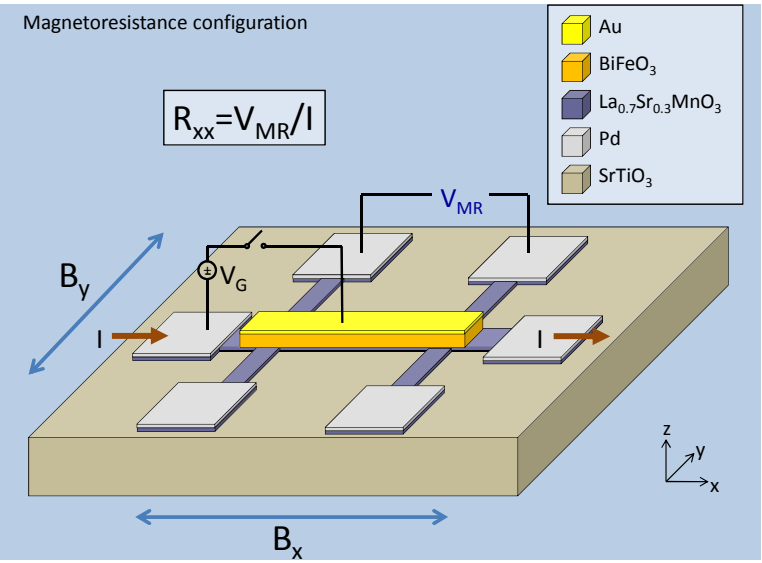

Figure 4.4: A schematic diagram showing how a four-point magnetoresistance measurement is measured in our device.

vector measurement of the voltage and current since parasitic sources of capacitance and inductance can lead to inaccurate measurements of channel resistance. Since the effects of magnetoresistance of LSMO at low temperatures are sometimes small, it sometimes becomes necessary to measure a very small change in resistance. To achieve this extra sensitivity, a bridge method was needed to subtract out the large background portion of the signal so that the remaining field sensitive signal could be determined with increased sensitivity. To accomplish this, before each measurement a phase synced sinusoidal signal equivalent in amplitude to the measured voltage at zero field is fed into the differential input of the lock-in amplifier to be subtracted out. The signal is phase synced to the input signal using a dual channel Agilent 33522A arbitrary waveform generator to ensure the signal is subtracted out correctly. A schematic depiction of the entire measurement setup is provided in Fig. 4.5.

Since LSMO is magnetically hysteretic and electronic transport is intimately linked to magnetism due to double exchange transport, it is to be expected that when measuring the magnetoresistance of LSMO the resulting measurement will also be hysteretic. Here we do magnetoresistance measurements on the LSMO channel by applying magnetic field along one of the two easy axes, [100] or [010]. The result is a curve that typically looks like Fig. 4.6, regardless of the direction field is applied in (B_x or B_y) or the direction of current in the channel. Sheet resistance is used over resistivity due to the small thickness of LSMO (8 u.c., 3 nm). Although highly growth dependent, transport measurements have shown that as LSMO films become thinner, an insulating dead layer exists below 8 u.c. [64]. Films of thickness less than 8 u.c. are insulating. Because of this, the true thickness of the transport layer is not known, but is presumed to be very thin (perhaps 2-dimensional). Therefore, it

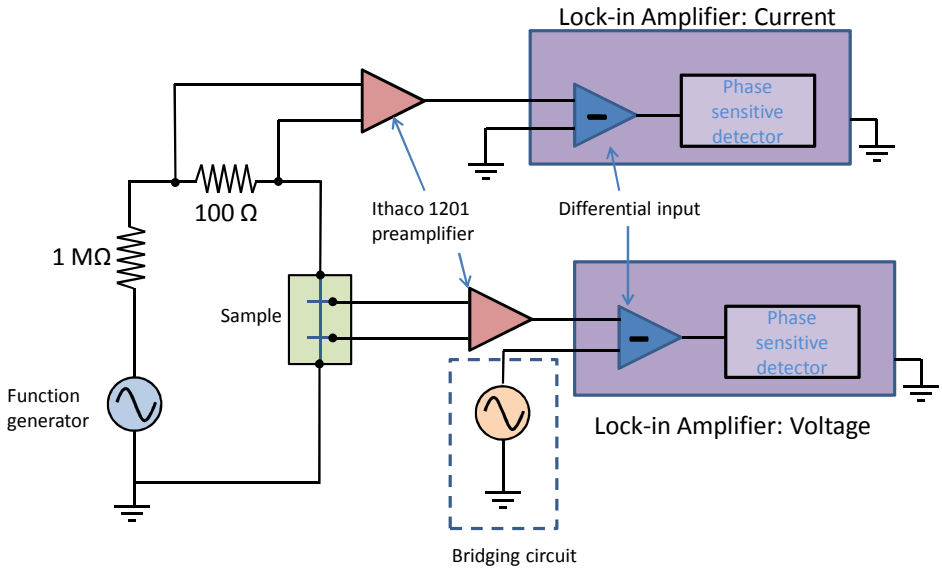

Figure 4.5: A diagram showing the electronics involved in a typical magnetoresistance measurement. A function generator provides a signal which is run through a current biasing resistor, a current measuring resistor, and the sample. Current and voltage are both lock-in detected and an optional bridging circuit may be used to increase the sensitivity of the voltage measurement (dotted box).

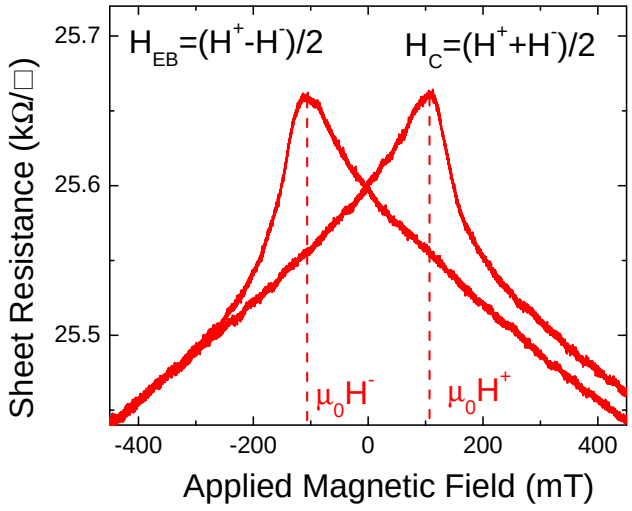

Figure 4.6: A typical magnetoresistance trace obtained from measuring MR.

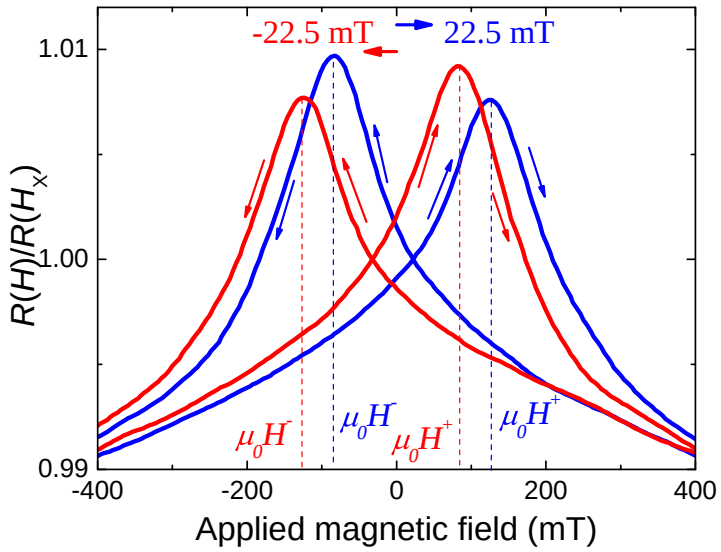

Figure 4.7: Two magnetoresistance measurements in the same device under two different field cooling conditions at 7 K. The red curve has been cooled with a +1 T field, and the blue curve has been cooled with a -1 T field. These values of exchange bias match well with the same field cooling experiment performed using SQUID magnetometery. H_X represents the magnetic field where the magnetoresistance traces cross.

is prudent to use sheet resistance over resistivity to describe the transport for our devices.

4.3 Comparison of Magnetotransport to SQUID Magnetometery

To connect magnetotransport measurements to magnetometery measurements performed with a SQUID magnetometer on unpatterned heterostructures, MR was measured using the same field cooling procedure used in magnetometery. Using the probe heater, the sample was heated up to ∼200 K and cooled in either ±1 T magnetic field to 7 K where MR was measured. The results are presented in Fig. 4.7. The traces are hysteretic and exhibit peaks where magnetization is zero due to the double exchange mechanism. From these data we define H^+ as the location of the positive peak, and H^- to be the location of the negative peak (Fig. 4.7). The coercive field (H_C) is then defined to be half the distance between the two peaks, $H_C = (H^+ - H^-)/2$, and the exchange bias is defined to be the magnitude of the peak shift from zero, $H_{EB} = (H^+ + H^-)/2$. For positive and negative field cooling we obtained essentially identical values to those measured with the SQUID at the same temperature. Since there is such a one to one match between magnetometery data and

MR, we feel confident in using this technique for identifying exchange bias and magnetic coercivity. Since eventual applications involve utilizing only the *conducting* part of the channel, this method is arguably *more* valid since SQUID magnetometery would measure the magnetism in *insulating* FM regions along with the conducting regions.

4.4 Sawyer-Tower Measurements

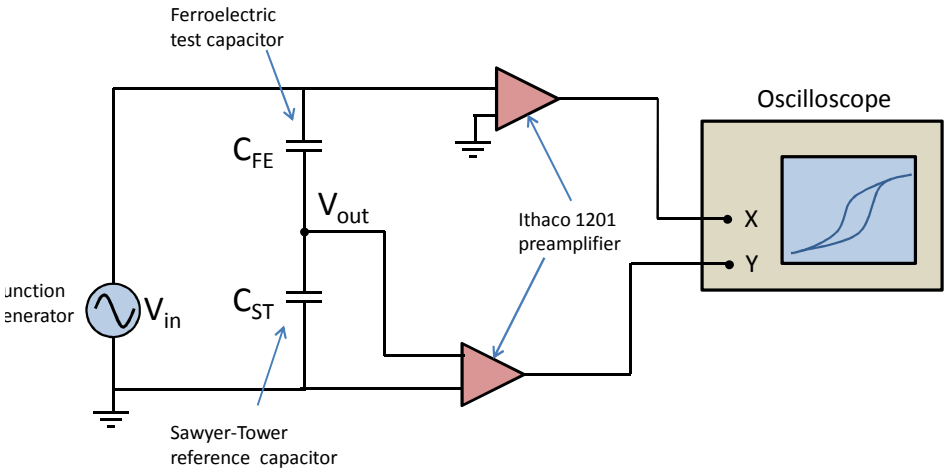

Figure 4.8: A diagram illustrating the Sawyer-Tower method of measuring ferroelectric polarization.

To evaluate the ferroelectric properties of BFO, a ferroelectric test capacitor was put into a Sawyer-Tower circuit configuration. The Sawyer-Tower circuit was one of the first methods of determining the polarization vs. voltage (PV) characteristics for ferroelectrics and remains one of the simplest [65]. The circuit is displayed in Fig. 4.8. Each capacitor is measured in a two-terminal configuration and is put in series with a reference capacitor. By applying a known voltage using a function generator to the entire circuit, the polarization of the test capacitor can be found. Knowing that

$$Q_{FE} = DA_{FE}, \tag{4.1}$$

$$Q_{ST} = C_{ST}V_{out}, \tag{4.2}$$

and that

$$Q_{ST} = Q_{FE} \tag{4.3}$$

because they are capacitors in series, we can deduce that

$$D = \frac{C_{ST}}{A_{FE}} V_{out}. \tag{4.4}$$

Here we define using the labels from Fig. 4.8, that Q_{FE} is the charge on the FE test capacitor, A_{FE} is the area of the FE test capacitor, D represents the displacement field across the FE test capacitor, Q_{ST} is the charge on the reference capacitor, C_{ST} is the capacitance of the reference capacitor, and V_{out} represents the voltage across the reference capacitor. Since the relationship between the D and polarization (P) is $D=\epsilon_0\epsilon_{FE}E+P$, we can extract the polarization from our measurement of V_{out}. It is very important that a high input impedance preamplifier is placed between the circuit and the oscilloscope, or else the low input impedance from the oscilloscope could easily shunt the capacitor under measurement. Additionally, this measurement is highly sensitive to parasitics such as capacitor leakage often leading to a nonexistent PV curve if the FE capacitor is too leaky. The result of a Sawyer-Tower measurement is presented in Fig. 4.9. From this we can conclude that there is minimal leakage in the BFO thin film and that the polarization values are consistent with normal thin film BFO. Subsequent DC measurements of the leakage through the gate showed that the gate resistance was over 100 GΩ.

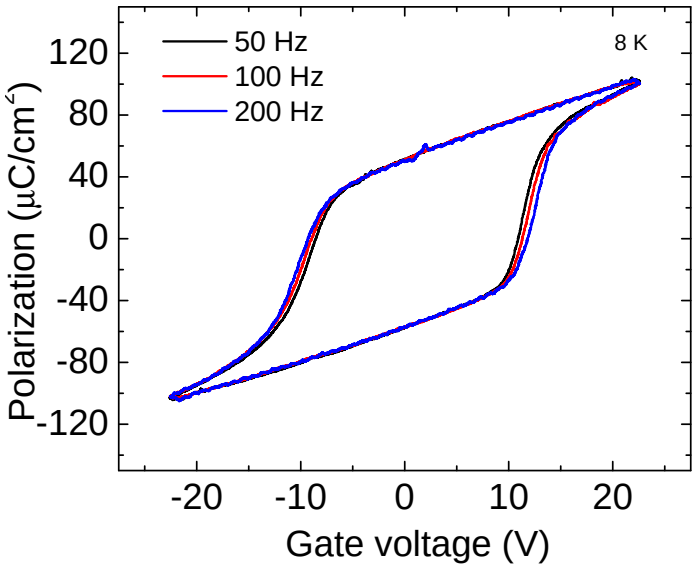

Figure 4.9: A Sawyer-Tower measurement of BFO ferroelectric hysteresis through a ferroelectric test capacitor fabricated on-chip along with BFO/LSMO field effect devices. Measurements were performed at multiple frequencies at 8 K.

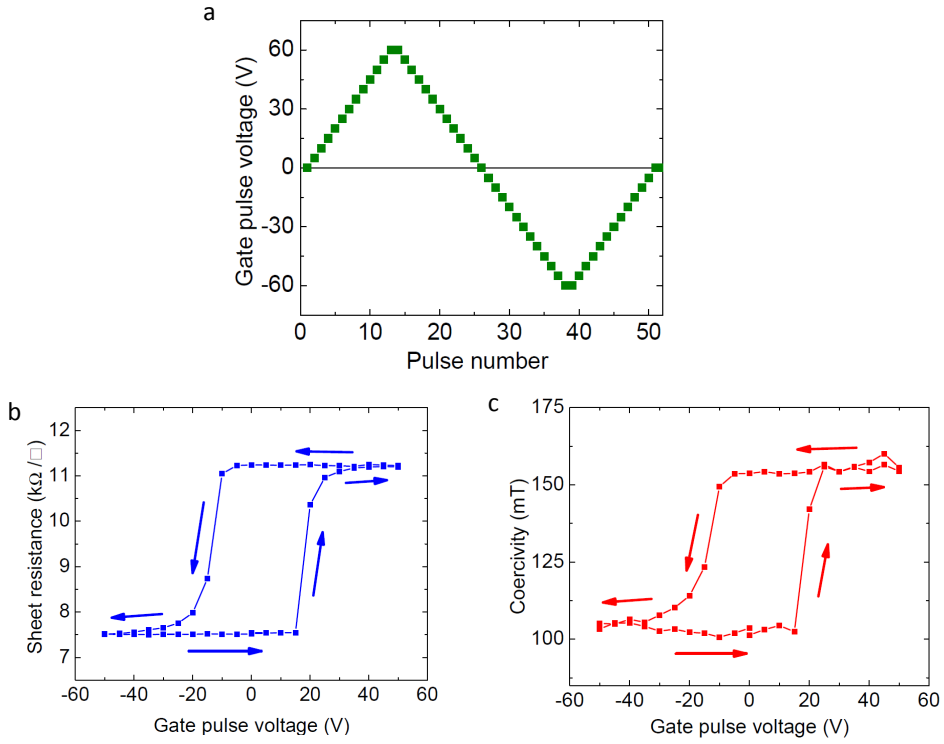

Figure 4.10: (a) shows the voltage pulse sequence applied to the gate during the measurement. Between each voltage pulse a MR measurement is performed and a hysteresis loop for quantities measured in the MR sweep can be formed. (b) shows the hysteresis curve for channel resistance, while (c) shows the hysteresis curve for the magnetic coercivity of the channel.

4.5 Effect of Ferroelectric Polarization on Channel Resistance and Magnetic Coercivity

After proving that the BFO thin film had no pinhole shorts, and that we can reliably change the polarization of this thin film, we now can examine the effect of BFO polarization on the channel resistance and magnetic coercivity. The device was cooled to 5.5 K in zero magnetic field upon which a sequence of 10 ms voltage pulses were applied to the gate (Fig. 4.10a). Between each voltage pulse the gate is left open, and a magnetoresistance sweep is performed. From this magnetoresistance sweep we can determine the channel resistance (by averaging the resistance at the two peaks) and magnetic coercivity (by finding the distance between the two peaks). In this way we can trace out a hysteresis curve of channel resistance and magnetic coercivity analogous to the PV curve measured in the previous section. A sheet

resistance (R_S)voltage pulse hysteresis curve, shown in Fig. 4.10b, illustrates this effect. The arrow on the curve shows the direction of the pulse sequence. For V_G pulses greater than 17 V the sheet resistance obtains an upper saturation value of 11.2 k$\Omega/\square$ and for V_G less than -17 V it exhibits a lower saturation value of 7.5 k$\Omega/\square$. The magnetic coercivity of the LSMO was also hysteretic with voltage applied to the BFO gate. A coercivity-V_G hysteresis curve is shown in Fig. 4.10c. Like the R_S-V_G curve, it also has saturation values at 17 V and -17 V of 155 mT and 100 mT respectively.

4.6 Exchange Bias Modulation

Here, we are finally prepared to address the most important question: What effect does changing BFO polarization have on exchange bias? Since the effect of exchange bias is much smaller than the previously measured quantities, the measurement becomes more challenging. To resolve a change in exchange bias, a new technique needs to be employed since the error in measurement is beginning to become comparable to the quantity being measured [66].

Measurement protocol

To begin the measurement, the device is cooled from room temperature to 5.5 K in zero magnetic field. Then a voltage pulse sequence is applied, with MR measurements done every time after the pulse. The difference in this experiment is that the voltage pulse sequence is designed to fully saturate the BFO ($\pm$24 V) instead of linearly ramping up in voltage. Here each 24 V pulse was applied multiple times in a square wave pattern. After each pulse, multiple MR sweeps were taken for signal averaging purposes to increase the accuracy of the measurement. The nature of this experiment requires us to leave the LSMO magnetized in the positive or negative direction when returning to zero applied magnetic field before the next subsequent pulse. This remanent LSMO magnetization (M_R) has a large effect on the exchange bias modulation, which we will explore in the following sections. An example of a typical measurement sequence is outlined in Fig. 4.11.

Automation

The entire exchange bias measurement process relies on taking a large amount of data to overcome the difficulties of accurately measuring such a small quantity. One downside to this process is that it takes a long time to obtain the data. Since after each gate voltage pulse the magnet is swept 6 times, and a typical sequence of pulses contains on the order of 100 pulses, it is easy to see that manually obtaining these measurements for multiple devices becomes an extremely challenging task. Each device would take several days of continuous measurement to characterize, and multiple devices fabricated on multiple chips would need to be measured in order to reach a conclusion about general device behavior. For these reasons, it was necessary to build an entirely automated measuring system that could perform measurements without human intervention.

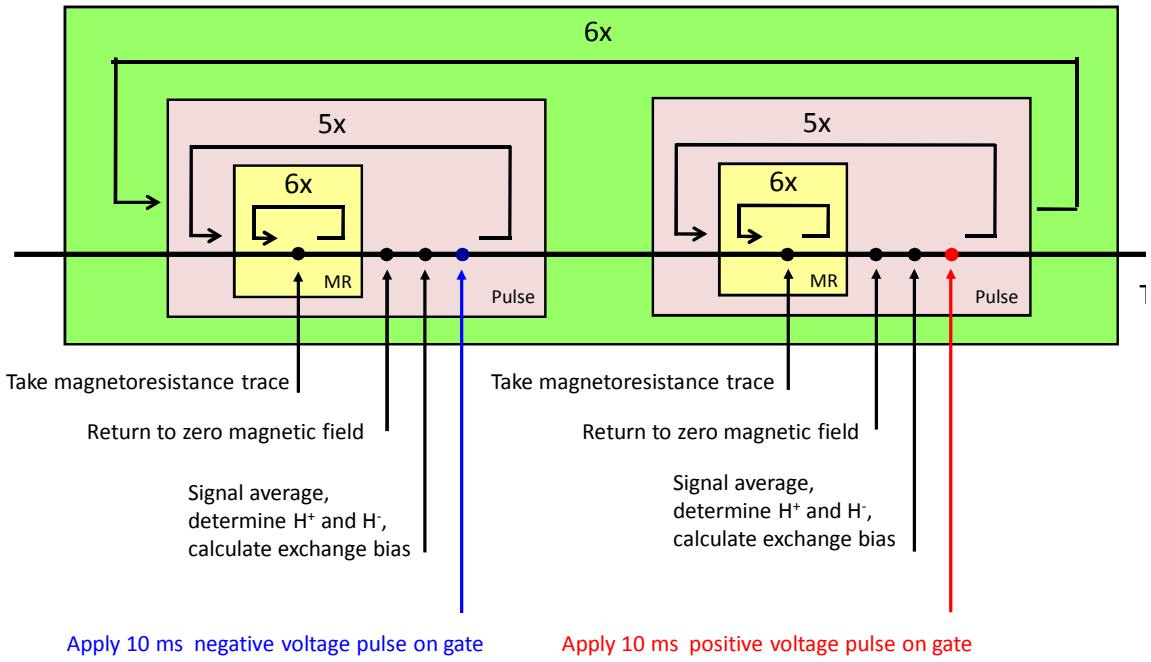

Figure 4.11: An example of the measurement protocol used in measuring exchange bias modulation through MR measurements.

Using the same system as described in Fig. 4.5 with a Labview controlled computer and an Agilent 34904A matrix switch module, the entire exchange bias measurement can be automated. Here the computer simultaneously controls the magnet power supply for magnetic field sweeping, the switch module for gate pulsing, the lock-in amplifier and function generator for bridging, the temperature controller for temperature control and several National Instruments ENET-9125 data acquisition (DAQ) systems for data acquisition. Due to the optically isolated nature of network based communication, all interfacing was done through LAN using ethernet to reduce noise on the measurement. In some cases RS-232 interfacing was used as a last resort. Using Labview, a scripting language was created to interpret commands, such as sweeping magnetic field or gate pulsing, to allow for maximum flexibility in the experiment. In this way, the automation system could be used in the most general case to measure all different types of magnetotransport phenomenon.

By using this automated system, human intervention was reduced and measurements could be set up to run for weeks at a time gathering large amount of data for statistical analysis later. The only remaining need for user intervention was to refill the magnet dewar with liquid helium every 48 hours to ensure the superconducting magnet did not quench.

Exchange bias modulation

Here we use the measurement protocol described in the previous section with the pulse sequence described in Fig. 4.12a to characterize a device with current in the [110] direction with applied magnetic field in the B_X [100] direction. Each pulse was followed by 6 sweeps from ± 0.5 T,and there are 70 pulses in total. The experiment was repeated twice with the LSMO left in different remanent magnetization states before gate pulsing. Figures 4.12b and 4.12c show modulation of exchange bias through the zero applied magnetic field axis with respect to gate pulse at 5.5 K in both remanent magnetization states. Depending on the remanent magnetization state of LSMO upon application of gate pulses, opposite ferroelectric polarizations lead to opposite directions of exchange bias. The exchange bias modulation behavior is mirrored through the zero exchange bias axis between different remanent magnetization states. The temperature of the sample was held constant at 5.5 K throughout pulsing and measurement. **No** additional field cooling was necessary to obtain this modulation effect, nor was any magnetic or electric bias field applied after each voltage pulse. The sole determining factors for the polarity of exchange bias in these devices are a) the polarization state of the BFO film and b) the M_R of LSMO. Thus, without any additional caveats, we have achieved the full direct electric field control of exchange bias, the first time this has ever been achieved in any system.

In addition to reversing exchange bias, the magnetic coercivity and channel resistance of LSMO were also changing with ferroelectric polarization (Fig. 4.12a,b,c). By pulsing the gate with a positive voltage we create a high resistance, high coercivity state, while pulsing with a negative voltage creates a low resistance, low coercivity state. This behavior is consistent at all temperatures measured,and throughout all devices studied in all configurations regardless of the direction of applied magnetic field or device geometry relative to the crystal axes.

Unipolar vs. bipolar modulation

Through experimenting with different device configurations, it was found that modulation through the zero applied magnetic field axis was not necessarily the only type of exchange bias modulation that could occur in these devices. As a reminder, devices were patterned along both the [100] and the [110] directions with respect to the substrate and magnetoresistance was measured with applied magnetic fields in both the [100] (B_X) and the [010] (B_Y) directions separately (Fig. 4.13). This provided four different device configurations for testing the angular dependence of exchange bias modulation. Two different types of exchange bias modulation occur within the four different configurations, the ability to reversibly switch between two exchange bias states with **opposite** polarity (bipolar exchange bias modulation), and the the ability to reversibly switch between two exchange bias states with the **same** polarity (unipolar exchange bias modulation). Devices with current in the [100] direction with applied magnetic field in the [100] (B_X) direction, exhibit unipolar exchange bias modulation while, all three other device configurations exhibit bipolar modulation of exchange bias through zero magnetic field as reported in the previous section. Additionally,

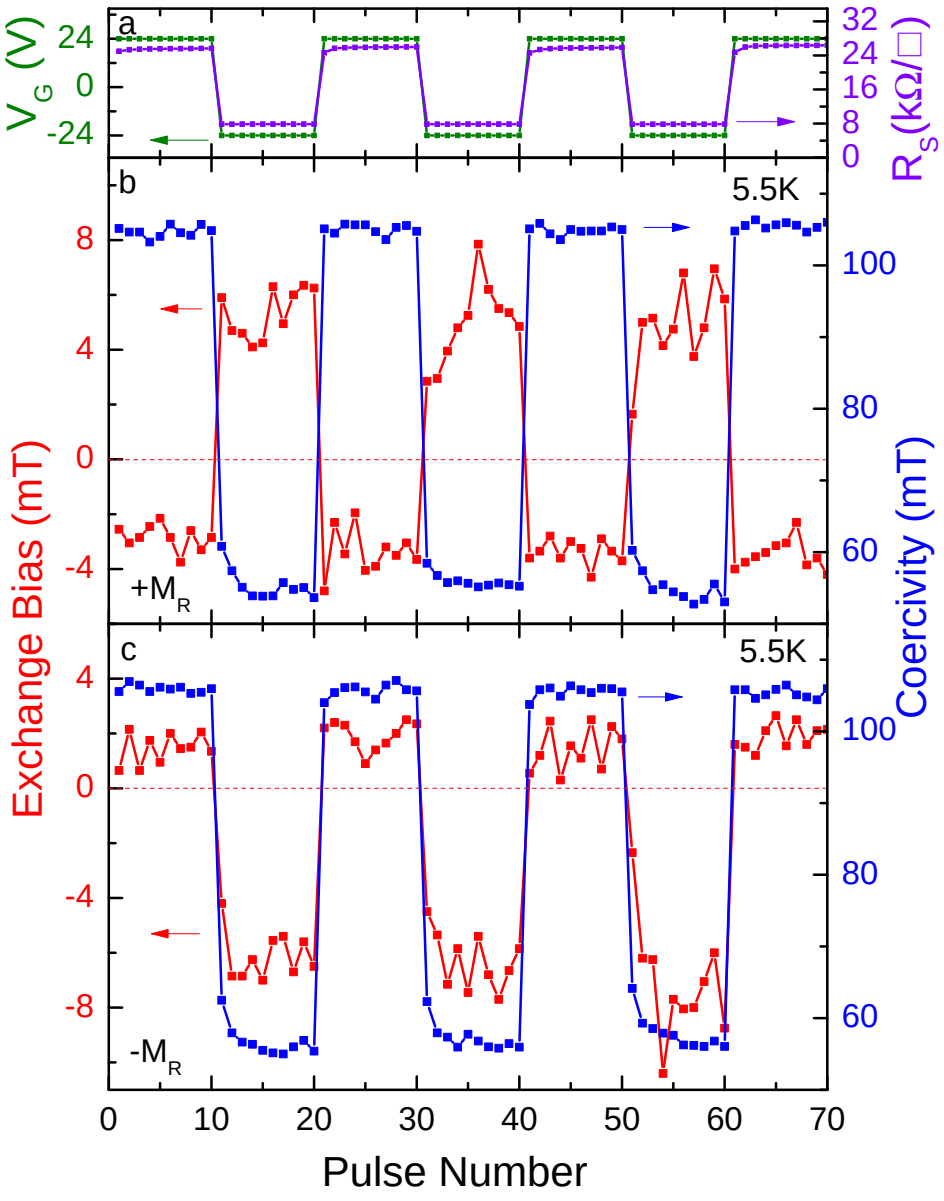

Figure 4.12: The sequence of voltage pulses applied to the gate through exchange bias measurement is shown in (a) along with the corresponding modulation in channel resistance. The exchange bias modulation behavior is shown for a device with current in the [110] direction and magnetic field applied in the B_x direction. (b) represents the $+M_R$ state and (c) represents the $-M_R$ state. Exchange bias is clearly seen to modulate through zero magnetic field.

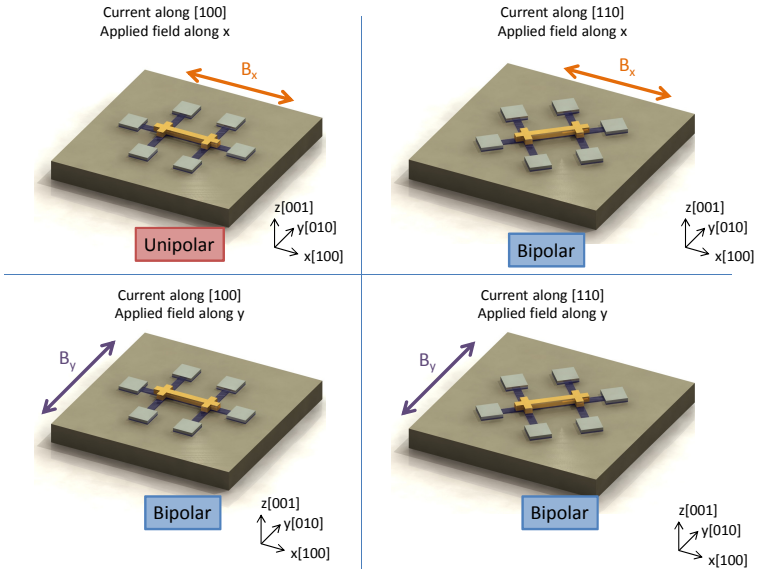

Figure 4.13: Here the four different measurement configurations are shown with its corresponding exchange bias modulation behaviors.

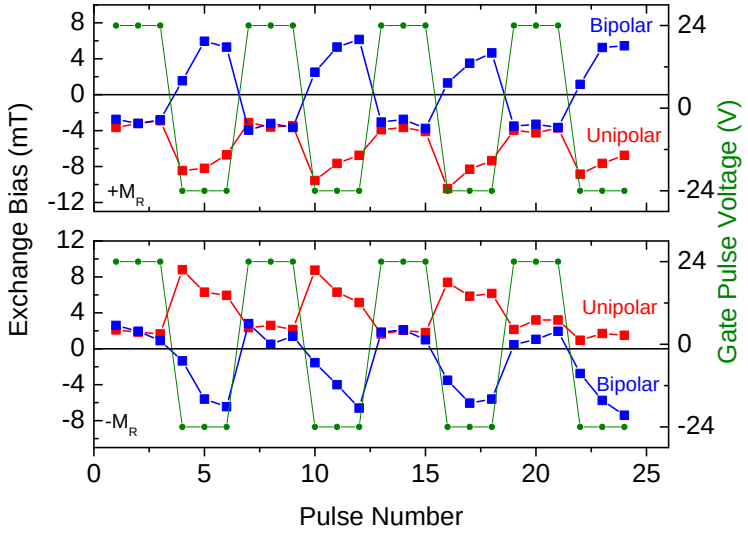

Figure 4.14: The behavior of two different devices are compared to illustrate the difference between unipolar and bipolar exchange bias. The unipolar device is a device with current in the [100] direction with field in the B_x direction, while the bipolar device is a device with current in the [110] direction with field in the B_x direction.

the modulation behavior between these bipolar devices was remarkably similar despite the different current and magnetic field directions. This behavior was highly reproducible and was observed in 20 devices fabricated on three separate epitaxially grown heterostructures. A comparison of unipolar and bipolar modulation is provided in Fig. 4.14. Here, the high-coercivity state in the unipolar device has similar exchange bias polarity and magnitude as in the bipolar device, suggesting that despite the differences in behavior the underlying mechanism of modulation is still the same.

4.7 Temperature Dependent Exchange Bias Modulation

To further explore the properties of these devices, temperature dependent measurements of exchange bias modulation were performed. Here using a temperature controller, we perform the same exchange bias MR measurements as in the previous sections (Fig. 4.12) but at several different temperatures. The average value of exchange bias in each state is then obtained from these measurements and is plotted vs. temperature. Since obtaining each exchange bias measurement is already a long process, and this temperature dependent measurement requires multiple temperatures in both remanent magnetization states, the data presented here are the result of a continuous week long measurement per device. In Fig. 4.15, temperature dependent exchange bias measurements are presented for both a bipolar and a unipolar device. In Fig. 4.15a we observe that there is bipolar modulation in both remanent magnetization states of the LSMO with a decrease towards zero exchange bias in both states as temperature is increased. The two remanent magnetization states have mirror symmetry across the zero exchange bias axis. The magnitude of exchange bias is always smaller in the positive BFO polarization state, which corresponds to the high electrical resistivity/magnetic coercivity state. Modulation disappears around 30 K, well below the blocking temperature of this system which was previously determined to be around ∼100-120 K using field cooling experiments. In Fig. 4.15b we observe that there is unipolar modulation in both remanent magnetization states, which also tends to decrease as temperature is increased. Although in this device there appears to be a slight offset from zero magnetic field in both M_R states that seems to be relatively constant in temperature. Since the blocking temperature of these devices are ∼100-120 K but our measurement stops at 90 K, it is unclear whether this offset disappears as temperature is further increased. The high resistivity/ coercivity state also has a lower value for exchange bias, as was the case for the bipolar device. These measurements were also reproduced on other devices on different chips, for both the unipolar and bipolar case.

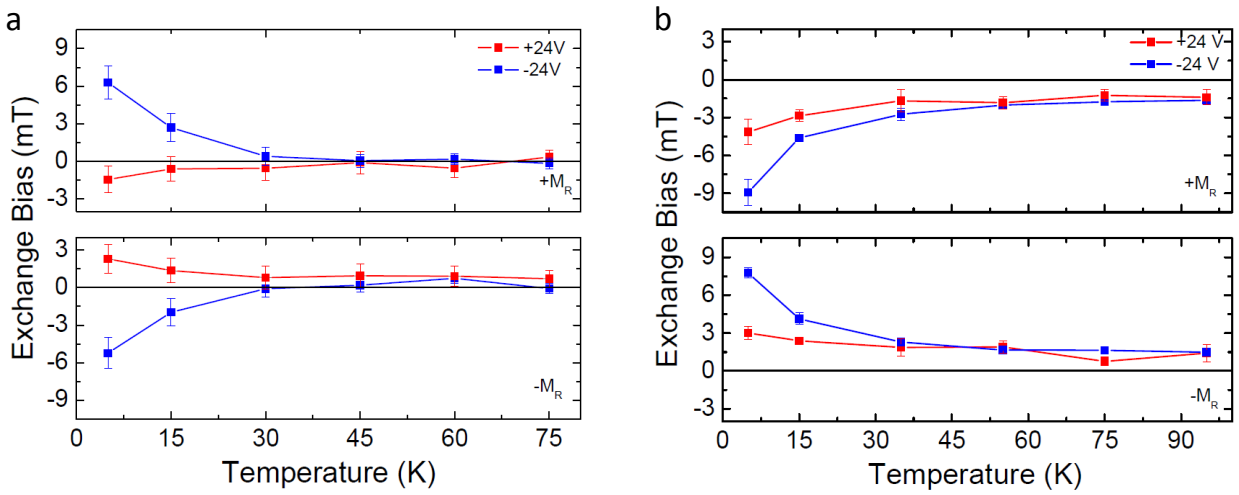

Figure 4.15: The temperature dependence of the exchange bias modulation. A device with current in the [110] direction and applied field in the B_x direction is shown in (a) where bipolar modulation is displayed. A device with current in the [100] direction and applied field in the B_x direction is shown in (b) where unipolar modulation is displayed.

4.8 Temperature Dependent Coercivity and Comparison to PZT/LSMO device

From the measurement of exchange bias vs. temperature, the temperature dependence of coercivity can also be extracted. To offer some comparisons, these measurements were also performed on a similarly built $Pb(Zr_{0.2}Ti_{0.8})O_3$ (PZT)/LSMO control field effect device. Since PZT is only a FE, without any additional AFM order, it is useful to use this device as a control to highlight some of the properties unique to the BFO/LSMO device. In Fig. 4.16 is seen that the large modulation of magnetic coercivity is unique to the BFO/LSMO system. In the PZT/LSMO device, only a small change in magnetic coercivity is induced between different polarization states likely due to electrostatic doping from the ferroelectric[67, 68]. Since there are no exchange interactions at the interface of the PZT/LSMO device, we argue that the larger coercive modulation in the BFO/LSMO system is solely due to the modulation of interfacial magnetic coupling strength.

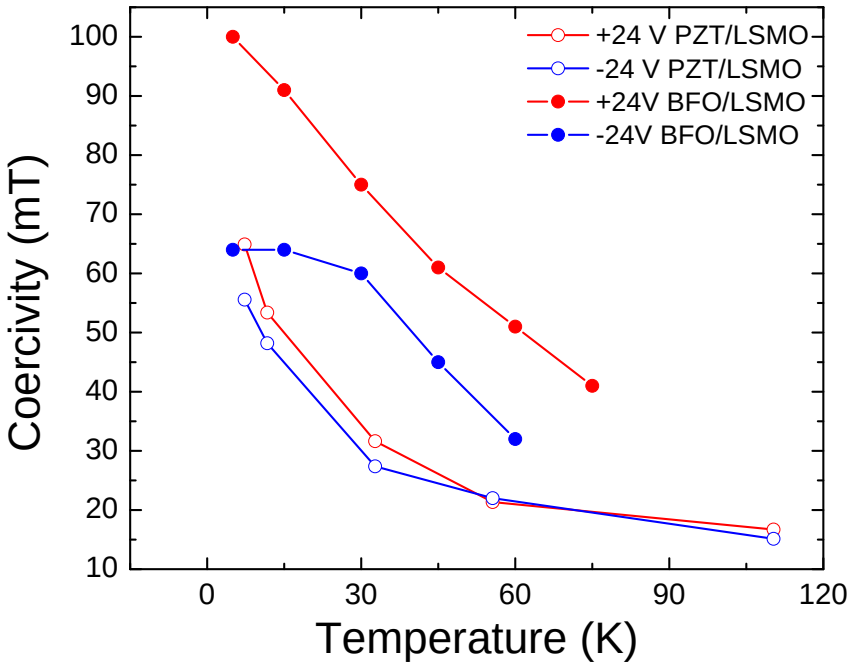

Figure 4.16: Temperature dependence of magnetic coercivity is presented for both a BFO/LSMO based field effect device and a PZT/LSMO based field effect device.

4.9 Sheet Resistance vs. Temperature

To obtain temperature dependent sheet resistance measurements (R-T measurements), a slightly different technique was used. Here we use the same dual lock-in technique to measure both current and voltage, but instead of using the temperature controller to control at specific temperatures, the temperature was ramped up at the rate of ∼0.2 K/s and the resistance was measured continuously. The slow rate of warming was needed to assure that the sample was in thermal equilibrium with the thermometer at all times. Initially the device sits at 5.5 K when a ±24 V voltage pulse is used to fully polarize the device into a specific polarization state before temperature ramping starts and the measurement begins.

Manganites such as LSMO exhibit unique behavior near room temperature, where LSMO undergoes a transition from an insulating to a metallic state at T_C. This is due to the effects of the double exchange transport mechanism. Initially the high temperature state is dominated by polarons in a strongly electron-phonon coupled transport regime where charge carriers can self-localize if energetically favorable lattice distortions exist [51]. This polaronic transport regime leads to a insulating state above T_C that transitions into a metallic state dominated by double exchange transport below T_C. Because of these mechanisms, a peak in

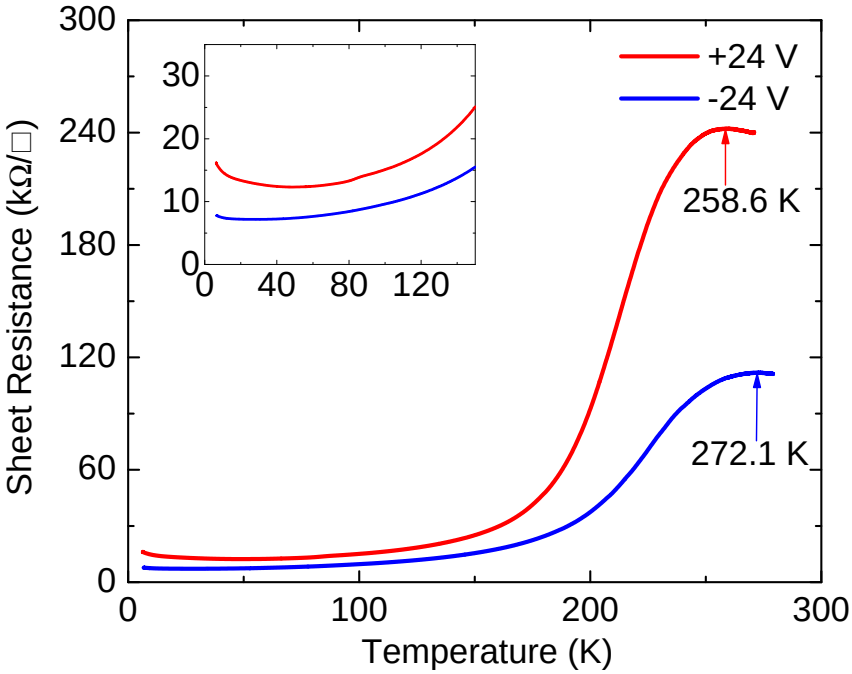

Figure 4.17: Temperature dependence of channel sheet resistance is presented. The Curie temperature of the channel can be determined from the high temperature peak in the R-T curve and is noted on the plot by arrows. The inset shows the same R-T curve but at low temperatures.

resistivity occurs at T_C in LSMO. Using this fact, we can judge what effect BFO polarization has on the T_C of LSMO. The results of the R-T measurement are presented in Fig. 4.17 for both states. A 13.5 K difference in T_C between the two different BFO polarization states can be observed, from 272.1 K in the low resistance state to 258.6 K in the high resistance state. This change in T_C is likely due to electrostatic doping, since we are above the exchange bias blocking temperature in this system, and this behavior is similar to T_C modulation in PZT/LSMO devices built by other groups [67, 68]. Here the carrier density is being modulated due the electrostatic effects of the changing BFO polarization, the resulting effect is the same as if the carrier density were to have changed due to a change in Sr doping in LSMO. The effect of carrier density modulation is examined in a later section in this chapter. The T_C in this device is lower than typical bulk LSMO, which exists at ∼390 K at its highest, but is typical for thin film LSMO where T_C is reduced as LSMO thickness is reduced. Measurements of T_C using this method match well with the value obtained using SQUID magnetometery in unpatterned BFO/LSMO heterostructures.

4.10 Hall Effect

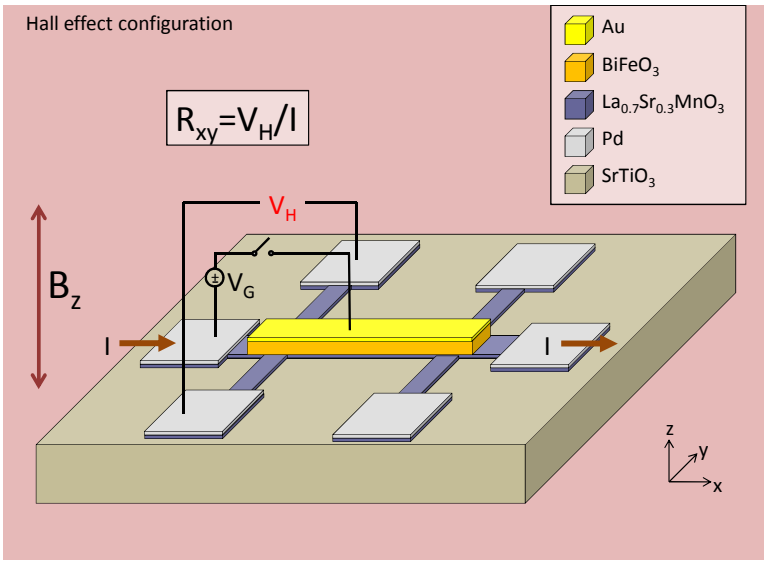

Figure 4.18: A schematic diagram showing how a four-point hall effect measurement is measured in our device.

To observe true effect of BFO polarization on LSMO carrier density, a more direct measurement such as the Hall effect is necessary. First discovered in 1897 by Edwin Hall while working on his doctoral degree, the Hall effect has since become a standard way of measuring carrier density in electronic materials. In the most general terms, the Hall effect refers to the accumulation of charge (which produces a voltage known as the Hall voltage) transverse to the current in the conductor when magnetic field is applied perpendicular to current. This is illustrated in Fig. 4.18. To make things more convenient we introduce a conductivity tensor as follows. For transport only in the x-y plane, we can define this as a 2x2 matrix.

$$\vec{j} = \widehat{\sigma}\vec{E} \tag{4.5}$$

$$\widehat{\sigma} = \begin{pmatrix} \sigma_{xx} & \sigma_{xy} \\ \sigma_{yx} & \sigma_{yy} \end{pmatrix} \tag{4.6}$$

Based on the Onsager reciprocity relations we can say $\sigma_{xx} = \sigma_{yy}$ and $\sigma_{yx} = -\sigma_{xy}$. Then these reduce to

$$\widehat{\sigma} = \begin{pmatrix} \sigma_{xx} & \sigma_{xy} \\ -\sigma_{xy} & \sigma_{xx} \end{pmatrix} \tag{4.7}$$

and

$$\widehat{\rho} = \begin{pmatrix} \sigma_{xx} & \sigma_{xy} \\ -\sigma_{xy} & \sigma_{xx} \end{pmatrix}^{-1} = \frac{1}{\sigma_{xx}^2 + \sigma_{xy}^2} \begin{pmatrix} \sigma_{xx} & -\sigma_{xy} \\ \sigma_{xy} & \sigma_{xx} \end{pmatrix}. \tag{4.8}$$

Similarly,

$$\widehat{\sigma} = \frac{1}{\rho_{xx}^2 + \rho_{xy}^2} \begin{pmatrix} \rho_{xx} & -\rho_{xy} \\ \rho_{xy} & \rho_{xx} \end{pmatrix}. \tag{4.9}$$

If one applies a magnetic field, B, to the sample in the z direction, we can measure the resistance in the x direction, $R_{xx} = V_x/I_x$, this can give you ρ_{xx} in the usual way. At the same time one can measure the Hall resistance $R_{xy} = V_y/I_x$, and similarly find ρ_{xy}. Knowing ρ_{xx} vs. B will give the usual magnetoresistance of the sample, and ρ_{xy} vs. B will give the Hall measurement.

Now we examine the electrodynamics of one electron traveling through the hall bar (Fig. 4.18). We know that the force on the electron can be described as $\vec{F} = m\frac{d\vec{v}}{dt} = \hbar\frac{d\vec{k}}{dt}$, and it is possible to including scattering by modifying the equation to $\vec{F} = m(\frac{d}{dt} + \frac{1}{\tau})\vec{v}$, where τ is the collision time. With this knowledge in addition to the equations for the Lorentz force on the electron, $\vec{F} = -e(\vec{E} + \frac{1}{c}\vec{v} \times \vec{B})$, we are able to deduce that in steady state we have the following relations:

$$v_x = -\frac{e\tau}{m}E_x - \omega_c\tau v_y, \tag{4.10}$$

$$v_y = -\frac{e\tau}{m}E_y + \omega_c\tau v_x, \tag{4.11}$$

$$v_z = -\frac{e\tau}{m}E_z, \tag{4.12}$$

where $\omega_c = eB/mc$, is the cyclotron frequency.

Now by demanding a transverse electric field to stop the electrons from flowing out of the material, we can obtain a relation between E_y and E_x.

$$E_y = -\omega_c\tau E_x \tag{4.13}$$

From this it can be worked out that, for an electron density of n:

$$\sigma_{xx} = \frac{ne^2\tau}{m}\frac{1}{1 + (\omega_c\tau)^2}, \tag{4.14}$$

$$\sigma_{xy} = -\frac{nec}{B}\frac{(\omega_c\tau)^2}{1 + (\omega_c\tau)^2}. \tag{4.15}$$

Here σ_{xy} has a simple relation to B, namely that its inversely proportional to it. As you can see, as we go to the high impurity limit, where $\omega_c\tau \gg 1$, the simple relation that $\sigma_{xy} = -\frac{nec}{B}$ holds, and it is easy to find out the carrier type and density. By switching to transverse resistivity and converting to SI we obtain:

$$\rho_{xy} = -\frac{1}{ne}B. \tag{4.16}$$

The slope of the line when ρ_{xy} vs. B is plotted is commonly referred to as the Hall coefficient R_H. The sign of R_H gives the sign of the charge carrier and the carrier density can be derived

from its magnitude. In magnetic materials this simple relation becomes more complicated due to the anomalous Hall effect, which introduces a magnetization dependent term to the Hall resistivity. The total Hall resistivity for magnetic materials is written as:

$$\rho_{xy}(B) = R_H B + \mu_0 R_S M(B). \tag{4.17}$$

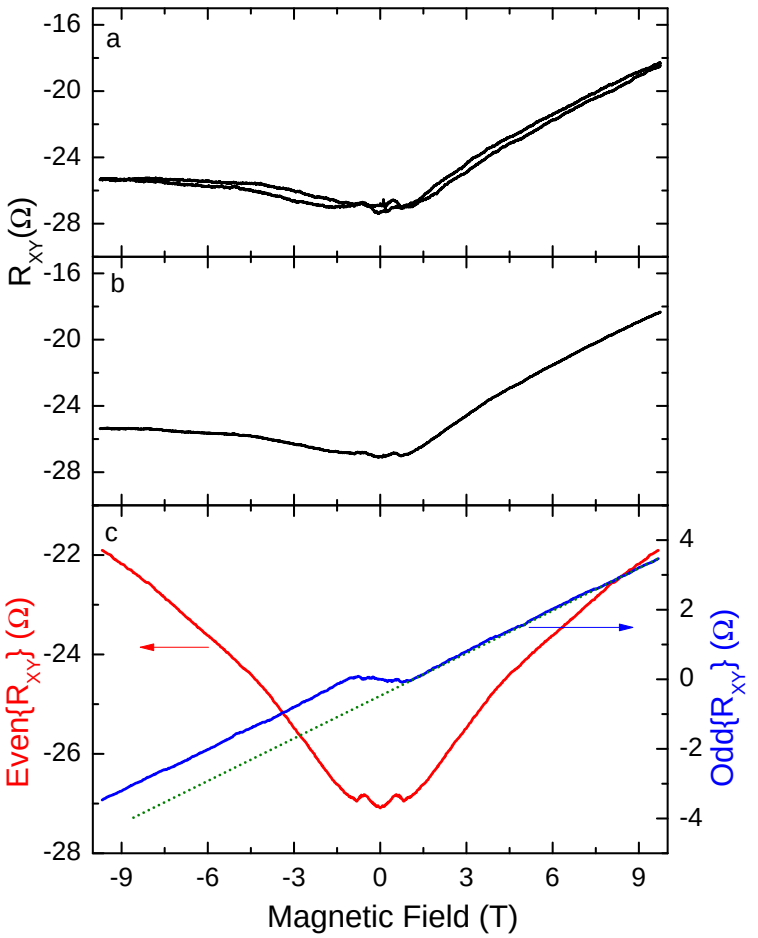

Figure 4.19: The process to obtaining the Hall coefficient from a BFO/LSMO field effect device is outlined. (a) shows the raw R_{xy} trace after sweeping magnetic field through 20 T. (b) shows the data now averaged together to remove the hysteresis from the traces. (c) shows the result of taking the even and odd components of the data in (b). The even component represents the magnetoresistance measured due to nonuniformity in the voltage probes, while the odd component represents the true R_{xy}. The dotted line represents the fit used to extract the Hall coefficient, beyond the anomalous hall portion of the curve.

To obtain these measurements of the carrier density with respect to BFO polarization, the sample was cooled to 5.5 K in no magnetic field. A voltage pulse sequence was then applied to the device with a Hall effect measurement between each pulse, similar to the measurement of MR except that the transverse voltage V_H is now measured instead of $V_M R$ and magnetic field is now applied out of plane (Fig. 4.18). Due to small offsets in the voltage probes due to lithographic errors from process nonuniformity, a component of magnetoresistance is always concomitantly measured. To extract the hall component, several sweeps of R_{xy} were measured from between +/- 10 T. These sweeps were averaged together to eliminate hysteresis and the odd part of the trace is taken. Here the odd and even parts of a function are defined as follows:

$$Odd\{f(x)\} = \frac{1}{2}(f(x) - f(-x)) \tag{4.18}$$

$$Even\{f(x)\} = \frac{1}{2}(f(x) + f(-x)). \tag{4.19}$$

Due to the fact that the magnetoresistance is an even function with respect of magnetic field, we are only left with the Hall component. From this we look at the portion of the R_{xy} vs. B that is outside of the anomalous Hall regime (after magnetization has been saturated) and extract the Hall coefficient/carrier density. This process is outlined in Fig. 4.19. Sheet carrier density was measured each time after a +/-24 V gate pulse in a sequence outlined in Fig. 4.20, in a similar way to the exchange bias measurements.

Ordinary hall effect

Figure 4.20 shows that BFO polarization affects sheet carrier density as one would expect from a ferroelectrically doped channel. There are fewer carriers in the high resistance state, while there are more carriers in the low resistance state. Carrier density appears to change from pulse to pulse, even when two successive pulses are of the same polarity. This is perhaps due to domain motion, and edge polarization effects that cause portions of the channel to not be evenly affected by the BFO. It can be seen that there is roughly only a $\sim$30% change in carrier density, despite the fact that resistivity of the channel changes over 300%. Clearly other factors play into the modulation of channel resistance that are unrelated to electrostatic doping. It is possible that the amount of scattering is increased when BFO polarization is switched due to motion of the electron gas into a more disordered region, or that phase separation plays a larger role in the modulation of resistance than previously thought.

Anomalous hall effect

In addition to the change in the ordinary Hall effect, BFO polarization switching affects the anomalous portion of ρ_{xy} as well. In Fig. 4.21, the Hall effect in two devices are compared. One device is oriented so current is along the [100] direction, and the other is oriented so current is along the [110] direction. The individual sweeps for Hall effect measurements were averaged together for each BFO polarization state in each device and plotted together

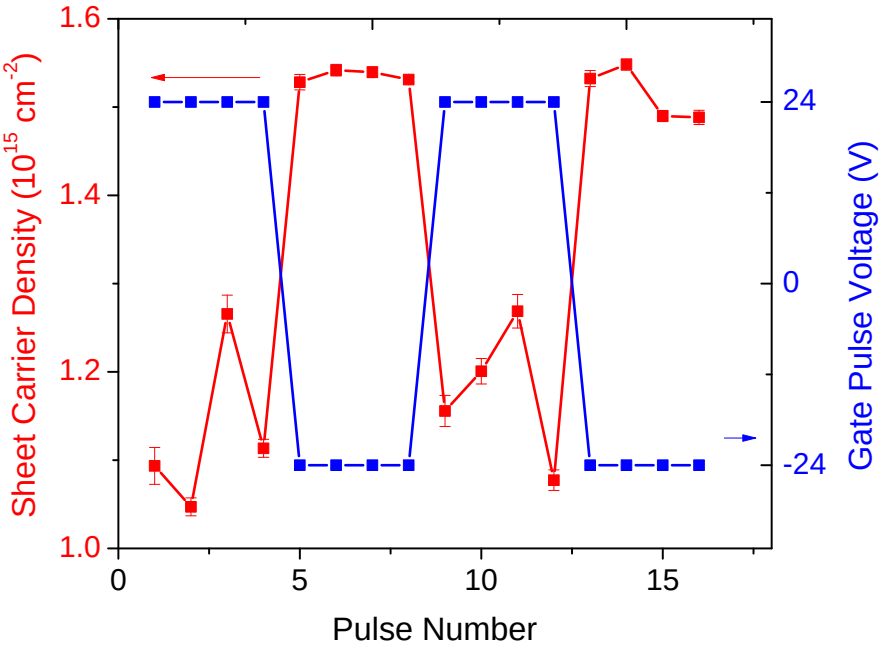

Figure 4.20: Using a similar measurement method as with MR measurements, a sequence of voltage pulses was applied to the gate, and Hall measurements were performed after each pulse. Here, the modulation of carrier density with respect to BFO polarization is shown.

to analyse the average Hall behavior. Here we observed that while in both devices the ordinary Hall effect behaves similarly, there was a remarkable difference in the behaviors in the anomalous Hall region of both devices. In the [100] device there was almost no anomalous Hall component in the +24 V state, while in the [110] device it is almost the same in both ±24 V states. This means that in the [100] device, we can electrically switch the anomalous Hall effect on and off. This result is important due to the fact that there are otherwise no significant differences between the two device orientations, and may lead to the understanding of why one out of four total device configurations shows unipolar modulation and the other three are bipolar.

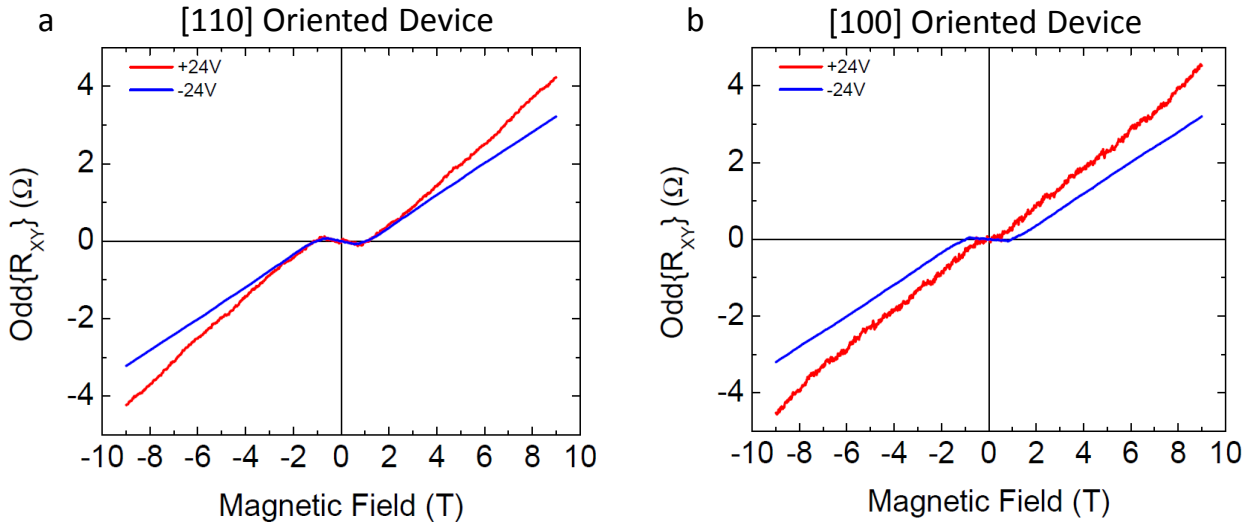

Figure 4.21: Averaged Hall effect measurements are shown for two devices, in both polarization states. The device oriented in the [110] direction shows no change in the anomalous region of the Hall data between polarization states in (a), while the device oriented in the [100] direction does.

Chapter 5

Mechanism for the Electric Control of Exchange Bias

In this chapter we attempt to explain the mechanisms responsible for exchange bias modulation using the information gathered from experiments. A summary of some of the unexplained phenomena seen in our devices is presented here. It has been observed that:

1. Exchange bias can be reversibly controlled with electric field into two different static states.
2. The exchange bias modulation behavior is strongly dependent on the remanent magnetization state when either gate voltage pulses are applied.
3. Two types of exchange bias modulation behavior occur (either unipolar or bipolar), which is determined by the direction the magnetic field is applied relative to the current in the channel.
4. Channel resistance and magnetic coercivity can also be reversibly controlled with electric field. The -24 V gate pulse state corresponds to the up polarization, low coercivity, and low resistance state, while the +24 V gate pulse state corresponds to the down polarization, high coercivity, and high resistance state.
5. When BFO/LSMO devices are compared to PZT/LSMO devices the change in coercivity is larger in BFO/LSMO devices at all temperatures measured.

Using the current understanding of exchange bias, oxide interface interactions, and manganite transport we can speculate on the underlying mechanisms behind these effects.

5.1 Eliminating Possible Models

Before introducing any device models it is prudent to thoroughly eliminate as many possible explanations for device behavior as possible. First, we examine thermal effects caused by

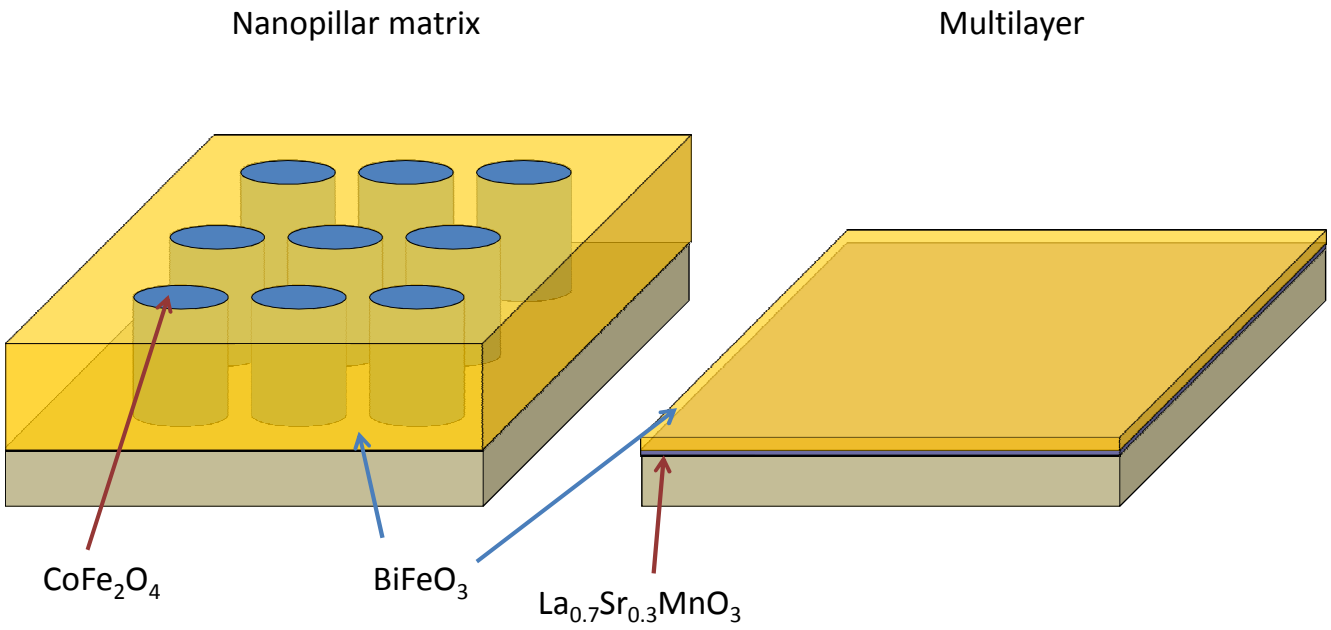

Figure 5.1: An illustration showing the difference between self assembled BFO/$CoFe_2O_4$ nanopillars and BFO/LSMO multilayers. Strain is efficiently transferred to the $CoFe_2O_4$ in the nanopillar matrix, while strain is not transferred to the LSMO due to substrate clamping.

Joule heating on our device, namely the possibility that the gate pulses are heating the system above the blocking temperature (T_B ~100-120 K). At our experimental temperature of 5.5 K the measured gate resistance is well over 100 GΩ (which would correspond to a maximum leakage current of 0.24 nA). With these limits, the total power dissipated within the device can be estimated to be 6 nW. This upper limit on power dissipation is negligible due to fact that samples are linked strongly to the helium bath and heat is easily dissipated. Further support for this conclusion can be argued that since the channel resistance is directly related to temperature, heating effects would manifest as an increase in resistance. We see no such evidence of this behavior; even with large voltages applied to the gate for several minutes there was no observed change in channel resistance. From this we conclude that we are unlikely affecting device behavior through any type of thermal effect from the gating voltage.

Next we examine the effects of strain on the device. By changing the polarization of BFO, strain can be transferred to the neighboring LSMO layer. It is then possible that gating is inducing magnetostrictive effects in the LSMO layer. Self-assembled $CoFe_2O_4$ vertical columnar nanostructures embedded in a BFO matrix have been shown to reverse magnetization after repeated BFO polarization switches [69]. This is believed to be due to the effect of strain-induced magnetic anisotropy changes in the $CoFe_2O_4$. Can a similar

magnetostrictive effect occur in our BFO/LSMO system? One key difference between the two experiments is that the BFO/LSMO structure is a bilayer thin film, while the BFO/$CoFe_2O_4$ system is made of $CoFe_2O_4$ nanopillars embedded in a BFO matrix (Fig. 5.1). In the latter, strain is more efficiently transferred to the magnetic material, while in the former the strain is not efficiently transferred due to clamping from the substrate [70, 71]. Similar strain-induced magnetoelectric effect experiments on PZT/LSMO bilayers have shown little effect on magnetization [72]. Our own experiments with a PZT/LSMO field effect device show no large change in magnetic behavior between different PZT polarization states, and the small amount of change is likely due to electrostatic doping not strain effects [67]. Additionally, no difference in modulation behavior was shown in our BFO/LSMO devices when experiments were performed with a large DC voltage continuously applied to the gate instead of gate pulses, suggesting that additional strain from the linear converse piezoelectric effect does not affect LSMO. From this we conclude that strain is not a factor in the behavior of our devices.

Finally, we examine the effect of BFO domain structure on our device. In our measurements a gate voltage is only applied in the [001] (OOP) direction to polarize the BFO. Using piezoresponse-force microscopy as outlined in a previous chapter, it has been shown that BFO polarization out-of-plane is fully saturated, however complex domain structures may still form in-plane since there are four degenerate in-plane polarization states (Fig. 2.7). Work done on $Co_{0.9}Fe_{0.1}$(CoFe)/BFO heterostructures shows a specific type of ferroelectric domain wall in BFO was a likely cause of exchange bias in this system [73]. Specifically, it was observed that a predominantly 71° domain structure in the BFO leads to an exchange *enhancement* of the coercive field, while a predominantly 109° domain structure leads to exchange *bias*. In contrast, in this present work, although the BFO domain structure is predominantly of the 71° type we still observe exchange bias. Furthermore, measurements of exchange bias in LSMO/BFO samples with different domain structures all show the same magnitude of exchange bias. Exchange bias is also independent of 71° domain wall spacing in this system, further indicating that the coupling is not occurring at the walls. Therefore, we believe that the mechanism for exchange bias in such epitaxial heterostructures is fundamentally different from the CoFe/BFO interface. Since we cannot measure the IP domain structure concurrently with our magnetotransport measurements, domains structure may still play a role in exchange bias behavior, but not in a way similar to the case with CoFe since the origin of exchange bias is different in LSMO [57].

5.2 Phenomenological Model

Having eliminated some possible mechanisms, we can now offer an informed model of our device. Current exchange bias models are based on the existence of an interface state between the AFM and FM that is markedly different than either the FM or the AFM individually [29]. Such an interface state will produce two different types of spins that contribute unequally to the exchange bias system[25, 74–76]. Some interface spins will become pinned in only

one direction by the AFM, unaffected by magnetic field. The interaction between these pinned spins and the FM causes an effective "bias field" that the underlying FM layer must overcome before magnetization can be switched, resulting in exchange bias. Other interface spins will rotate with the FM layer when magnetic field is swept, because they are coupled more tightly to the FM than the AFM. This results in a spin drag effect that increases the coercivity of the FM material. Recently, several groups have observed these types of magnetic interface interactions in exchange bias systems [28, 77]. As outlined in a previous chapter, in BFO/LSMO heterostructures the interface is unique due to an emergent interfacial magnetic state resulting from the enhanced canting of the AFM spins in an otherwise magnetically compensated interface [57]. It was shown that this state is directly related to exchange bias. Also it was shown that in this system the coupling between Fe^{3+} ions in the magnetic interface layer and the $Mn^{3+/4+}$ ions in LSMO was antiferromagnetic in nature, meaning these spins are anti-aligned. Many exchange bias systems exhibit this type of AFM interfacial coupling, but no reversals in exchange bias occur until extremely high magnetic fields are applied to overcome the interfacial coupling and align all spins to the external magnetic field. Since we do not use such high fields, the basic exchange bias model described above does not change. Some spins will be pinned, and some will rotate with the FM; although since the coupling to the interface layer is antiferromagnetic, the interface spins will evolve in the opposite fashion as compared to the ferromagnetically coupled case [78].

Based on these models for exchange bias, we present a physical model that explains the following effects: bipolar exchange bias modulation, the remanent magnetization dependence of that modulation,and coercivity modulation. Furthermore, this picture also explains why exchange bias magnitude is lower in the high coercivity state than in the low coercivity state regardless of M_{R}. The progression of the magnetic state in our device as magnetic field is swept and after a gate pulse reverses BFO polarization is shown in Fig. 5.2. Figure 5.2a shows the progression in terms of a magnetic hysteresis loop and Fig. 5.2b shows the same progression but from an interfacial spin state perspective. Due to the ferroelectric nature of BFO, when ferroelectric polarization is switched, the Fe and Bi ions will move relative to the oxygen octahedra [79]. Since the LSMO channel does not exhibit the same effect, the Fe ion at the interface in BFO exists in two different states depending on ferroelectric polarization, one closer to the LSMO channel and one further away. In our system the AFM anisotropy is much greater than the FM anisotropy [43, 80], thus we are left with only two parameters that determine the exchange bias behavior: AFM anisotropy (K_{AFM}) and the interfacial interaction energy ($J_{\mathrm{AFM/FM}}$). By changing the distance between interacting ions, we are manipulating $J_{\mathrm{AFM/FM}}$ relative to K_{AFM} causing two different exchange bias states to exist: the high $J_{\mathrm{AFM/FM}}$ (positive gate voltage pulse, down polarization, high resistivity, Fe closer to interface) state and the low $J_{\mathrm{AFM/FM}}$ (negative gate voltage pulse, up polarization,low resistivity, Fe further from interface) state. Initially (Fig. 5.2b1) the system is in the negative magnetization state, with small magnitude positive exchange bias and high coercivity. As magnetic field is swept (Fig. 5.2b1-5) a large number of interfacial spins rotate with the FM while a smaller fraction remain pinned, this results in the high coercivity/low exchange bias state and is caused by increased coupling to the FM due to ionic displacement. After

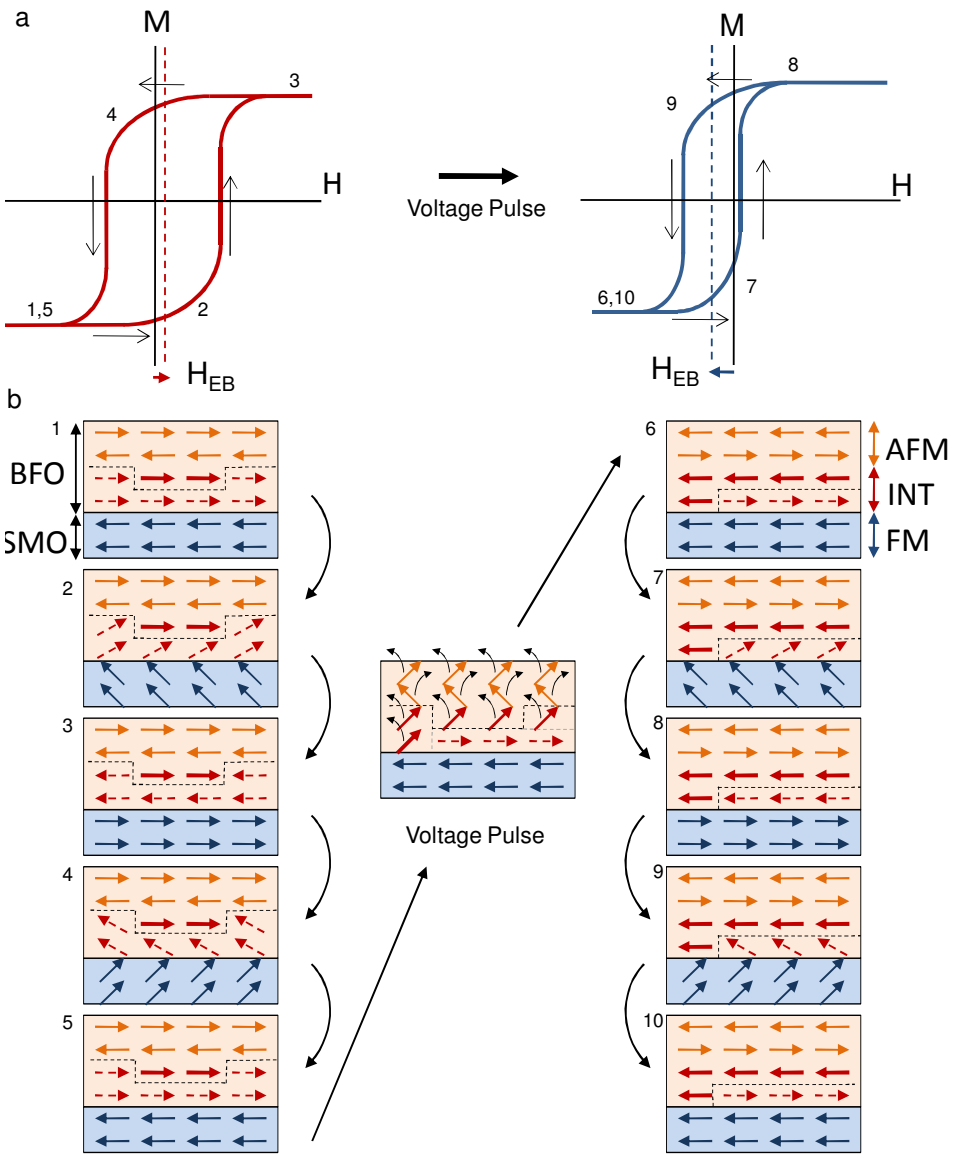

Figure 5.2: (a) Example magnetic hysteresis curve of LSMO before and after BFO ferroelectric polarization reversal in the negative remanent magnetization state. Numbers and arrows represent the progression of time as magnetic field is swept. (b) Depiction of interfacial spins for each number in (a). AFM anisotropy is reduced at the interface between a FM (orange) and AFM (blue) creating an interface layer (red) with rotatable AFM spins (dashed red arrows) that rotate with the FM when magnetic field is applied and pinned AFM spins (bold red arrows) that are not affected by applied magnetic field.

applying a negative voltage pulse to the gate and changing ferroelectric polarization we are now in a different regime and the device now exhibits high magnitude negative exchange bias and low coercivity (Fig. 5.2b6). Since the coupling at the interface is weakened due to ionic displacement, a larger fraction of interfacial spins are pinned to the AFM. Due to the coupled AFM/FE order in BFO the individual coupled spins have also changed polarity leading to exchange bias reversal.

It was observed in all devices, that changing between remanent magnetization states required positive gate pulses before negative pulses. By merely reversing the direction of sweeping magnetic field (thus leaving the system in the reverse remanent magnetization), exchange bias behavior does not significantly change even upon further negative pulsing. Using the same model, we can explain this effect and the remanent magnetization dependence of exchange bias modulation. A positive voltage pulse is first required to increase coupling to the FM so more interfacial spins rotate with the LSMO upon sweeping. After sweeping magnetic field, the rotatable spins will now be in the direction of the LSMO remanent magnetization, and once a negative voltage pulse is applied, some fraction of these rotatable spins become pinned contributing to exchange bias in the exact opposite way it would have behaved in the opposite remanent magnetization. Note that here we assume that the AFM has no effect on setting the exchange bias polarity, and only has the ability to flip the pinned spins once a remanent magnetization state is determined.

5.3 Unipolar vs. Bipolar Modulation

The marked similarity of modulation behavior between the three bipolar configurations suggests that unipolar modulation is a special case, and there might exist a mechanism that nullifies the bipolar behavior. In fact, as we see in Fig. 4.14, the high-coercivity state in the unipolar device has roughly the same exchange bias polarity and magnitude as in the bipolar device. This suggests that the model for exchange bias modulation in the unipolar devices is still the same, but the effect of pinned spins reversing under BFO polarization switching is absent. The exchange bias magnitude is still larger in the low-coercivity state which suggests that there is still an increase in pinned spins but the direction is solely determined by the magnetization of the LSMO and is not flipped by BFO polarization. Reasons for this lack of spin reversal are not well understood although they may be related to the BFO ferroelectric domain structure in-plane, which can only be imaged on the unpatterned heterostructures at room temperature before device fabrication and thus remains a mystery to us after numerous switches. Changes in the domain structure could favor a certain type of switching behavior that leaves AFM interface spins untouched upon switching.

The only other evidence for differences between devices is the change in anomalous Hall effect in [100] devices when BFO polarization is switched, which does not appear in [110] devices. In manganite systems the anomalous Hall effect is even more complex than in conventional ferromagnetic systems. As a reminder the Hall effect in ferromagnetic systems behaves as $\rho_{xy}(B) = R_H B + \mu_0 R_S M(B)$. In conventional ferromagnetic systems both R_H and

R_S have the same sign, but in LSMO R_H has hole-like behavior while R_S is electron-like. This causes the characteristic dip near zero magnetic field in Fig. 4.21. The current understanding of the origin of this effect involves modifying the anomalous Hall effect for double exchange systems. Here a charge carrier moves in a topologically nontrivial spin background that causes it to acquire a Berry phase that affects the motion of the charge carrier in the same way a phase arising from a physical magnetic field would [81]. This "magnetic field" then contributes in a way opposite to the applied physical magnetic field. This Berry phase contribution is highly related to spin-orbit coupling strength in the material. Work has been done in $La_{2/3}Ca_{1/3}MnO_3$ systems that show there is a difference in spin-orbit coupling strength when current is directed along the [100] vs. the [110] directions through anomalous Hall effect and anisotropic magnetoresistance measurements [82]. In our device we go one step further, where anomalous Hall effect can be electrically controlled in [100] oriented devices. While the underlying mechanisms for this are unclear, one theory might involve the ability to change spin-orbit coupling strength in LSMO with BFO polarization. This could be yet another important factor in whether the device behaves in a bipolar or unipolar fashion.

5.4 Path to Full Control of Magnetization and Room Temperature Operation

Having examined the possible mechanisms behind exchange bias modulation, now we can speculate on some of the necessary steps to take in order to fully control the magnetization of a thin film ferromagnet at room temperature with electric field. Two of the most obvious requirements to enable the switching of magnetization at room temperature is that $H_{EB} > H_C$ (Fig. 1.6) , and that the blocking temperature must exist above room temperature. Currently we are in the regime where $H_{EB} < H_C$, such that even though we are modulating exchange bias through zero magnetic field, magnetization does not switch. Additionally, the blocking temperature of this system sits well below room temperature at around 100-120 K.

Without changing the materials system, we can attempt to counter some of these effects through careful materials engineering. A simple way to increase exchange bias is to grow the LSMO thinner. This increases the contribution of the interface layer and has been shown to increase exchange bias in this system. The problem with this method is that there is an electronic/magnetic dead layer in LSMO when the thickness is reduced below 8 u.c., though this fact is highly growth dependent and perhaps higher quality growth can reduce or circumvent this limitation [64]. Another method of increasing exchange bias in this system is by changing the interface termination at the BFO/LSMO interface. By adding an additional 2.5 u.c. thick layer of $SrRuO_3$ before the growth of LSMO, the termination of LSMO at the interface can be changed from a MnO_2 termination to a $La_{0.7}Sr_{0.3}O$ termination. Exchange bias in these systems has been shown to increase, although not to the point where $H_{EB} > H_C$. Additionally, since BFO exhibits a compensated magnetic interface along the (100) plane, we

can attempt to create an uncompensated plane to increase exchange bias by allowing growth to occur on the (111) planes, which may increase blocking temperature as well. In a system like this, gating will become more difficult because a voltage applied along the out-of-plane direction will only involve 180° switchs in polarization which will leave the AFM easy planes unchanged.

By changing the materials system, we open the door to a larger number of possibilities. By changing the FM layer it is possible to have exchange bias occur in several other systems coupled to BFO such as CoFe [73], CoFeB [83],$CoFe_2O_4$ [69],or NiFe[84]. Some of the key factors in selecting which ferromagnetic material may enhance performance use are outlined here:

1. The system should exhibit room temperature exchange bias.
2. The system should have $H_{EB} > H_C$.
3. It should be easy to create high quality epitaxial interfaces between the FM and BFO.
4. It should be easy to create high quality thin films of this material without dead layers.
5. The material should ideally not have complicated electronic transport properties (like phase separation in LSMO).

To this date there are no FM materials that exhibit all these behaviors when coupled to BFO. CoFe and NiFe come the closest although creating high quality epitaxial single crystal interfaces is a challenge [85]. Using a different mechanism, progress has been made in terms of switching magnetization with BFO in CoFe systems. Here the magnetic moment in a non-exchange biased sample of BFO/CoFe is directly coupled to the canted magnetic moment in BFO allowing for magnetization reversal in some BFO/CoFe heterostructures closely related to the IP domain structure [86]. Another method of obtaining a higher level of control in BFO systems is through device engineering. We have seen that in-plane domain structure plays a large role in some BFO coupled systems. Through nanoscale device engineering we create a device within a single ferroelectric domain of BFO. By introducing both a top electrode gate, and a side gate, electric field can now be applied in four different directions. If a BFO field effect device is patterned along the [110] direction, there will only be four possible polarization directions in BFO that can be directly controlled with the application of gate voltage. E-beam lithography techniques will be necessary to pattern side gates close enough to the channel that excessive voltages will not have to be applied to switch the BFO in the in-plane direction. In Fig. 5.3, a example of a nanopatterned Hall bar with side gates are shown. This mask was patterned using e-beam lithography and reactive ion etching on a trilayer mask consisting of Shipley S1808 photoresist/Ge/PMMA. At this scale, gating through both the top and side gates would roughly only require 24 V to fully polarize. Through this type of nanoscale device engineering, we gain extra control over some factors contributing to exchange bias in BFO systems and perhaps open the door to full reversible static magnetization control when the right material systems are used.

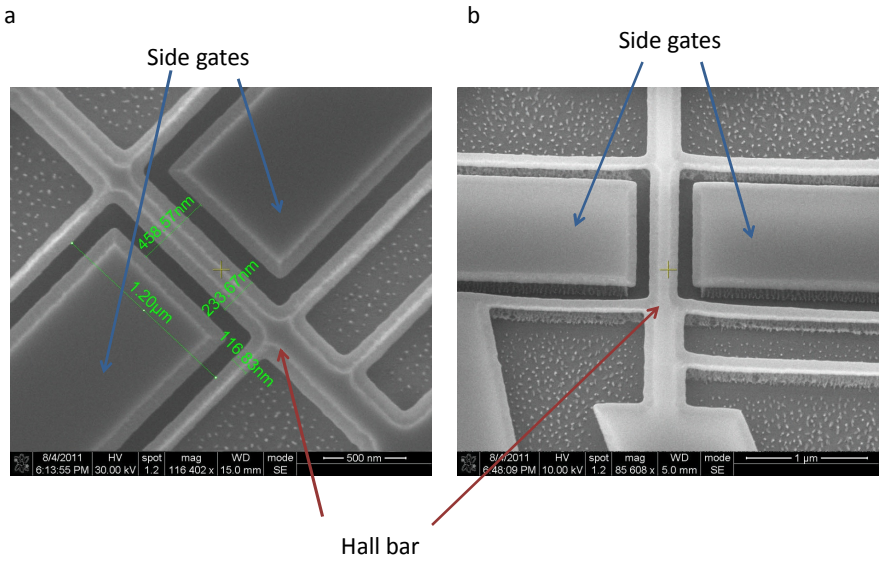

Figure 5.3: A scanning electron micrograph of a nanopatterned Hall bar type structure with side gates. This pattern was written using e-beam lithography into a electron beam sensitive resist (PMMA), and further patterned using reactive ion etching. The result is a tall nanoscale trilayer mask made from Shipley S1808 photoresist, Ge, and PMMA ready for ion milling. (a) is a top down view, where (b) is viewed at a 28° tilt angle.

Chapter 6

Conclusions and Future Prospects

We have discovered a mechanism for the direct control of exchange bias with electric field, the first time this has been accomplished in any system. This effect is reversible and comes concurrently with the modulation of channel resistance (sometimes over 300%), and the modulation of magnetic coercivity. Since LSMO is highly spin polarized at low temperatures [87], and this device architecture is already designed as a field effect device ready for use, one can immediately see the potential applications. This type of exchange bias control is also a crucial first step toward fully controlling the magnetization of a thin film using an electric field [88, 89]. Using this method of controlling magnetization would offer a low-current/low-power alternative to the typical current induced magnetization control mechanisms [90]. In addition, in this device we are able to directly manipulate the interfacial spin structure between a FM and an AFM and see the immediate effects. This allows us to peer into the exchange bias mystery in a way that has not been done before and what we observe matches the current understanding of exchange bias systems, thus expanding our understanding of this interface phenomenon.

However, there are still several unexplained aspects of these devices, the most salient of which is the relationship between device configuration and unipolar/bipolar exchange bias modulation. This begs for more experimentation into the angular dependence of exchange bias modulation, as well as a more careful examination of in-plane domain structure. Creating a similar Hall bar device in the nanoscale regime, where single domain control of BFO polarization can be accomplished, will help elucidate some of these effects. Additionally, more careful angular dependent studies into the anomalous Hall effect could reveal that some basic property of the material, such as spin orbit coupling strength, is changing and causing unipolar behavior. From a more basic manganite physics standpoint, one question left unanswered is why the LSMO carrier density only changes by approximately 30% when channel resistance sometimes changes 300% with BFO polarization. This may be due to heavily decreased mobility due to the fact that the system is close to a thickness limit where the film goes insulating, but phase separation may also play a role. Since LSMO has a larger bandwidth than its closely related cousins such as $La_{1-x}Ca_xMnO_3$, it is expected that there are *less* phase separation effects in its transport properties, although this is likely to change

as the thickness of LSMO is decreased. Investigations into the phase separated nature of ultrathin-film LSMO are necessary to shed light on this topic. Additionally, the Understanding all these topics will allow for further improvement on this device structure, which may eventually lead to large exchange bias effects and the full control of magnetization up to room temperature. From both a device applications and physics standpoint, the results gathered from BFO/LSMO field effect devices represent an exciting advance for the next generation of exchange bias systems and devices.

Bibliography

[1]P Curie, J. Physique **3**, 393 (1894).

[2]D. Astrov, "The magnetoelectric effect in antiferromagnetics", Sov. Phys.-JETP **11**, 708–709 (1960).

[3]I. Dzyaloshinskii, Sov. Phys.-JETP **10**, 628 (1959).

[4]M. Fiebig, "Revival of the magnetoelectric effect", J. Phys. D: Appl. Phys. **38**, R123 (2005).

[5]W. Eerenstein, N. Mathur, and J. Scott, "Multiferroic and magnetoelectric materials", Nature **442**, 759–765 (2006).

[6]S. Cheong and M. Mostovoy, "Multiferroics: a magnetic twist for ferroelectricity", Nat. Mater. **6**, 13–20 (2007).

[7]R. Ramesh and N. Spaldin, "Multiferroics: progress and prospects in thin films", Nat. Mater. **6**, 21–29 (2007).

[8]N. Spaldin and M. Fiebig, "The renaissance of magnetoelectric multiferroics", Science **309**, 391–392 (2005).

[9]N. Hill, "Why are there so few magnetic ferroelectrics?", J. Phys. Chem. B **104**, 6694–6709 (2000).

[10]T. Kimura, "Spiral magnets as magnetoelectrics", Annu. Rev. Mater. Res. **37**, 387–413 (2007).

[11]J. Wang, J. Neaton, H. Zheng, V. Nagarajan, S. Ogale, B. Liu, D. Viehland, V. Vaithyanathan, D. Schlom, U. Waghmare, N. Spaldin, K. Rabe, M. Wuttig, and R. Ramesh, "Epitaxial $BiFeO_3$ multiferroic thin film heterostructures", Science **299**, 1719–1722 (2003).

[12]J. Valasek, "Piezo-electric and allied phenomena in Rochelle salt", Phys. Rev. **17**, 475 (1921).

[13]R. Cohen and H. Krakauer, "Electronic structure studies of the differences in ferroelectric behavior of $BaTiO_3$ and $PbTiO_3$", Ferroelectrics **136**, 65–83 (1992).

[14]R. Seshadri and N. Hill, "Visualizing the role of Bi 6s lone pairs in the off-center distortion in ferromagnetic $BiMnO_3$", Chem. Mater. **13**, 2892–2899 (2001).

[15]T. Kimura, S. Kawamoto, I. Yamada, M. Azuma, M. Takano, and Y. Tokura, "Magnetocapacitance effect in multiferroic $BiMnO_3$", Phys. Rev. B **67**, 180401 (2003).

[16]T. Katsufuji, S. Mori, M. Masaki, Y. Moritomo, N. Yamamoto, and H. Takagi, "Dielectric and magnetic anomalies and spin frustration in hexagonal $RMnO_3$(R= Y, Yb, and Lu)", Phys. Rev. B **64**, 104419 (2001).

[17]M. Kenzelmann, A. Harris, S. Jonas, C. Broholm, J. Schefer, S. Kim, C. Zhang, S. Cheong, O. Vajk, and J. Lynn, "Magnetic Inversion Symmetry Breaking and Ferroelectricity in $TbMnO_3$", Phys. Rev. Lett. **95**, 87206 (2005).

[18]Z. Huang, Y. Cao, Y. Sun, Y. Xue, and C. Chu, "Coupling between the ferroelectric and antiferromagnetic orders in $YMnO_3$", Phys. Rev. B **56**, 2623 (1997).

[19]T. Zhao, A. Scholl, F. Zavaliche, K. Lee, M. Barry, A. Doran, M. P. Cruz, Y. H. Chu, C. Ederer, N. A. Spaldin, R. R. Das, D. M. Kim, S. H. Baek, C. B. Eom, and R. Ramesh, "Electrical control of antiferromagnetic domains in multiferroic $BiFeO_3$ films at room temperature", Nat. Mater. **5**, 823–829 (2006).

[20]J. Nogues and I. K. Schuller, "Exchange bias", J. Magn. Magn. Mater. **192**, 203–232 (1999).

[21]W. H. Meiklejohn and C. P. Bean, "New Magnetic Anisotropy", Phys. Rev. **102**, 1413–1414 (1956).

[22]C. Vaz, "Electric field control of magnetism in multiferroic heterostructures", J. Phys.: Condens. Matter **24**, 333201 (2012).

[23]M. Kiwi, "Exchange bias theory", J. Magn. Magn Mater. **234**, 584–595 (2001).

[24]A. Berkowitz and K. Takano, "Exchange anisotropya review", J. Magn. Magn. Mater. **200**, 552–570 (1999).

[25]J. Nogues, J. Sort, V. Langlais, V. Skumryev, S. Surinach, J. Munoz, and M. Baro, "Exchange bias in nanostructures", Physics Reports **422**, 65 –117 (2005).

[26]D. Mauri, H. Siegmann, P. Bagus, and E. Kay, "Simple model for thin ferromagnetic films exchange coupled to an antiferromagnetic substrate", J. Appl. Phys. **62**, 3047–3049 (1987).

[27]A. Malozemoff, "Random-field model of exchange anisotropy at rough ferromagnetic-antiferromagnetic interfaces", Phys. Rev. B **35**, 3679 (1987).

[28]H. Ohldag, A. Scholl, F. Nolting, E. Arenholz, S. Maat, A. T. Young, M. Carey, and J. Stohr, "Correlation between exchange bias and pinned interfacial spins", Phys. Rev. Lett. **91**, 017203 (2003).

[29]F. Radu and H. Zabel, "Exchange bias effect of ferro-/antiferromagnetic heterostructures", Magnetic Heterostructures **227**, 97–184 (2008).

[30]V. Laukhin, V. Skumryev, X. Marti, D. Hrabovsky, F. Sanchez, M. V. Garcia-Cuenca, C. Ferrater, M. Varela, R. Luders, J. F. Bobo, and J. Fontcuberta, "Electric-field control of exchange bias in multiferroic epitaxial heterostructures", Phys. Rev. Lett. **97**, 227201 (2006).

[31]X. He, Y. Wang, N. Wu, A. N. Caruso, E. Vescovo, K. D. Belashchenko, P. A. Dowben, and C. Binek, "Robust isothermal electric control of exchange bias at room temperature", Nat. Mater. **9**, 579–585 (2010).

[32]N. Spaldin, S. Cheong, and R. Ramesh, "Multiferroics: Past, present, and future", Phys. Today **63**, 38 (2010).

[33]M. Fiebig, T. Lottermoser, D. Frohlich, A. Goltsev, and R. Pisarev, "Observation of coupled magnetic and electric domains", Nature **419**, 818 (2002).

[34]B. Van Aken, T. Palstra, A. Filippetti, and N. Spaldin, "The origin of ferroelectricity in magnetoelectric $YMnO_3$", Nat. Mater. **3**, 164 (2004).

[35]G. Catalan and J. Scott, "Physics and applications of bismuth ferrite", Adv. Mater. **21**, 2463 (2009).

[36]P. Royen and K. Swars, "Das System Wismutoxyd-Eisenoxyd im Bereich von 0 bis 55 Mol% Eisenoxyd", Angew. Chem. **69**, 779 (1957).

[37]C. Michel, J. Moreau, G. Achenbach, R. Gerson, and W. James, "The atomic structure of $BiFeO_3$", Solid State Commun. **7**, 701 (1969).

[38]J. Teague, R. Gerson, and W. James, "Dielectric hysteresis in single crystal $BiFeO_3$", Solid State Commun. **8**, 1073 (1970).

[39]P. Fischer, M. Polomska, I. Sosnowska, and M. Szymanski, "Temperature dependence of the crystal and magnetic structures of $BiFeO_3$", J. Phys. C: Solid State Phys. **13**, 1931 (1980).

[40]I. Sosnowska, T. Neumaier, and E. Steichele, "Spiral magnetic ordering in bismuth ferrite", J. Phys. C: Solid State Phys. **15**, 4835 (1982).

[41]D. Lebeugle, D. Colson, A. Forget, M. Viret, A. Bataille, and A. Gukasov, "Electric-Field-Induced Spin Flop in $BiFeO_3$ Single Crystals at Room Temperature", Phys. Rev. Lett. **100**, 227602 (2008).

[42]S. Lee, W. Ratcliff, S. Cheong, and V. Kiryukhin, "Electric field control of the magnetic state in $BiFeO_3$ single crystals", Appl. Phys. Lett. **92**, 192906 (2008).

[43]C. Ederer and N. Spaldin, "Weak ferromagnetism and magnetoelectric coupling in bismuth ferrite", Phys. Rev. B **71**, 060401 (2005).

[44]H. Fujishiro, M. Ikebe, Y. Konno, and T. Fukase, "Sound Velocity Anomaly Associated with Polaron Ordering in $La_{1-x}Sr_xMnO_3$", J. Phys. Soc. Jpn. **66**, 3703 (1997).

[45]E. Dagotto, *Nanoscale phase separation and colossal magnetoresistance: the physics of manganites and related compounds* (Springer, 2003).

[46]J. Van Santen and G. Jonker, "Electrical conductivity of ferromagnetic compounds of manganese with perovskite structure", Physica **16**, 599 (1950).

[47]G. Jonker and J. Van Santen, "Ferromagnetic compounds of manganese with perovskite structure", Physica **16**, 337 (1950).

[48]S. Jin, T. Tiefel, M. McCormack, R. Fastnacht, R. Ramesh, and L. Chen, "Thousandfold change in resistivity in magnetoresistive La-Ca-Mn-O films", Science **264**, 413 (1994).

[49]C. Zener, "Interaction between the d-shells in the transition metals. II. Ferromagnetic compounds of manganese with perovskite structure", Phys. Rev. **82**, 403 (1951).

[50]M. Uehara, S. Mori, C. Chen, and S. Cheong, "Percolative phase separation underlies colossal magnetoresistance in mixed-valent manganites", Nature **399**, 560 (1999).

[51]M. Salamon and M. Jaime, "The physics of manganites: Structure and transport", Rev. Mod. Phys. **73**, 583 (2001).

[52]L. Zhang, C. Israel, A. Biswas, R. Greene, and A. de Lozanne, "Direct observation of percolation in a manganite thin film", Science **298**, 805 (2002).

[53]E. Dagotto, T. Hotta, and A. Moreo, "Colossal magnetoresistant materials: the key role of phase separation", Phys. Rep. **344**, 1 (2001).

[54]D. Chrisey and G. Hubler, *Pulsed laser deposition of thin films* (Wiley-VCH, 2003).

[55]A. Ichimiya and P. Cohen, *Reflection high-energy electron diffraction* (Cambridge University Press, 2004).

[56]M. Kawasaki, K. Takahashi, T. Maeda, R. Tsuchiya, M. Shinohara, O. Ishiyama, T. Yonezawa, M. Yoshimoto, and H. Koinuma, "Atomic Control of the $SrTiO_3$ Crystal Surface.", Science **266**, 1540 (1994).

[57]P. Yu, J.-S. Lee, S. Okamoto, M. D. Rossell, M. Huijben, C.-H. Yang, Q. He, J. X. Zhang, S. Y. Yang, M. J. Lee, Q. M. Ramasse, R. Erni, Y.-H. Chu, D. A. Arena, C.-C. Kao, L. W. Martin, and R. Ramesh, "Interface Ferromagnetism and Orbital Reconstruction in $BiFeO_3$-$La_{0.7}Sr_{0.3}MnO_3$ Heterostructures", Phys. Rev. Lett. **105**, 027201 (2010).

[58]J. Stohr, "Exploring the microscopic origin of magnetic anisotropies with X-ray magnetic circular dichroism (XMCD) spectroscopy", J. Magn. Magn. Mater. **200**, 470 (1999).

[59]H. Gross, N. Bansal, Y. Kim, and S. Oh, "In situ study of emerging metallicity on ion-bombarded $SrTiO_3$ surface", J. Appl. Phys. **110**, 073704 (2011).

[60]G. Pacchioni, "Oxygen vacancy: The invisible agent on oxide surfaces", ChemPhysChem **4**, 1041 (2003).

[61]D. Reagor and V. Butko, "Highly conductive nanolayers on strontium titanate produced by preferential ion-beam etching", Nat. Mater. **4**, 593 (2005).

[62]G. Herranz, O. Copie, A. Gentils, E. Tafra, M. Basletic, F. Fortuna, K. Bouzehouane, S. Fusil, E. Jacquet, C. Carrtro, M. Bibes, A. Hamzic, and A. Barthlmy, "Vacancy defect and carrier distributions in the high mobility electron gas formed at ion-irradiated $SrTiO_3$ surfaces", J. Appl. Phys. **107**, 103704 (2010).

[63]O. Tufte and P. Chapman, "Electron mobility in semiconducting strontium titanate", Phys. Rev. **155**, 796 (1967).

[64]M. Huijben, L. Martin, Y. Chu, M. Holcomb, P. Yu, G. Rijnders, D. Blank, and R. Ramesh, "Critical thickness and orbital ordering in ultrathin $La_{0.7}Sr_{0.3}MnO_3$ films", Phys. Rev. B **78**, 094413 (2008).

[65]C. Sawyer and C. Tower, "Rochelle salt as a dielectric", Phys. Rev. **35**, 269 (1930).

[66]S. M. Wu, S. A. Cybart, P. Yu, M. D. Rossell, J. X. Zhang, R. Ramesh, and R. C. Dynes, "Reversible electric control of exchange bias in a multiferroic field-effect device", Nat. Mater. **9**, 756–761 (2010).

[67]X. Hong, A. Posadas, A. Lin, and C. H. Ahn, "Ferroelectric-field-induced tuning of magnetism in the colossal magnetoresistive oxide La1-xSrxMnO3", Phys. Rev. B **68**, 134415 (2003).

[68]X. Hong, J. B. Yau, J. D. Hoffman, C. H. Ahn, Y. Bason, and L. Klein, "Effect of electric field doping on the anisotropic magnetoresistance in doped manganites", Phys. Rev. B **74**, 173306 (2006).

[69]F. Zavaliche, H. Zheng, L. Mohaddes-Ardabili, S. Yang, Q. Zhan, P. Shafer, E. Reilly, R. Chopdekar, Y. Jia, P. Wright, D. Schlom, Y. Suzuki, and R. Ramesh, "Electric field-induced magnetization switching in epitaxial columnar nanostructures", Nano Lett. **5**, 1793 (2005).

[70]C. Nan, G. Liu, Y. Lin, and H. Chen, "Magnetic-field-induced electric polarization in multiferroic nanostructures", Phys. Rev. Lett. **94**, 197203 (2005).

[71]H. Zheng, J. Wang, S. Lofland, Z. Ma, L. Mohaddes-Ardabili, T. Zhao, L. Salamanca-Riba, S. Shinde, S. Ogale, F. Bai, D. Viehland, Y. Jia, D. Schlom, M. Wuttig, A. Roytburd, and R. Ramesh, "Multiferroic $BaTiO_3$-$CoFe_2O_4$ nanostructures", Science **303**, 661 (2004).

[72]Y. Ma, W. Cheng, M. Ning, and C. Ong, "Magnetoelectric effect in epitaxial Pb(ZrTi)O/ LaSrMnO composite thin film", Appl. Phys. Lett. **90**, 152911 (2007).

[73]L. Martin, Y. Chu, M. Holcomb, M. Huijben, P. Yu, S. Han, D. Lee, S. Wang, and R. Ramesh, "Nanoscale control of exchange bias with $BiFeO_3$ thin films", Nano Lett. **8**, 2050 (2008).

[74]B. Miller and E. Dahlberg, "Use of the anisotropic magnetoresistance to measure exchange anisotropy in Co/CoO bilayers", Appl. Phys. Lett. **69**, 3932–3934 (1996).

[75]M. Stiles and R. McMichael, "Model for exchange bias in polycrystalline ferromagnet-antiferromagnet bilayers", Phys. Rev. B **59**, 3722 (1999).

[76]M. Stiles and R. McMichael, "Coercivity in exchange-bias bilayers", Phys. Rev. B **63**, 064405 (2001).

[77]J. Wu, J. S. Park, W. Kim, E. Arenholz, M. Liberati, A. Scholl, Y. Z. Wu, C. Hwang, and Z. Q. Qiu, "Direct Measurement of Rotatable and Frozen CoO Spins in Exchange Bias System of CoO/Fe/Ag(001)", Phys. Rev. Lett. **104**, 217204 (2010).

[78]J. Nogues, C. Leighton, and I. K. Schuller, "Correlation between antiferromagnetic interface coupling and positive exchange bias", Phys. Rev. B **61**, 1315–1317 (2000).

[79]J. X. Zhang, Q. He, M. Trassin, W. Luo, D. Yi, M. D. Rossell, P. Yu, L. You, C. H. Wang, C. Y. Kuo, J. T. Heron, Z. Hu, R. J. Zeches, H. J. Lin, A. Tanaka, C. T. Chen, L. H. Tjeng, Y. H. Chu, and R. Ramesh, "Microscopic Origin of the Giant Ferroelectric Polarization in Tetragonal-like BiFeO3", Phys. Rev. Lett. **107**, 147602 (2011).

[80]K. Steenbeck and R. Hiergeist, "Magnetic anisotropy of ferromagnetic $La_{0.7}(Sr, Ca)_{0.3}MnO_3$ epitaxial films", Appl. Phys. Lett. **75**, 1778–1780 (1999).

[81]J. Ye, Y. Kim, A. Millis, B. Shraiman, P. Majumdar, and Z. Tesanovic, "Berry phase theory of the anomalous Hall effect: application to colossal magnetoresistance manganites", Phys. Rev. Lett. **83**, 3737 (1999).

[82]M. Bibes, V. Laukhin, S. Valencia, B. Martinez, J. Fontcuberta, O. Gorbenko, A. Kaul, and J. Martinez, "Anisotropic magnetoresistance and anomalous Hall effect in manganite thin films", J. Phys.: Condens. Matter **17**, 2733 (2005).

[83]H. Bea, M. Bibes, F. Ott, B. Dupe, X. Zhu, S. Petit, S. Fusil, C. Deranlot, K. Bouzehouane, and A. Barthelemy, "Mechanisms of Exchange Bias with Multiferroic $BiFeO_3$ Epitaxial Thin Films", Phys. Rev. Lett. **100**, 17204 (2008).

[84]J. Dho, X. Qi, H. Kim, J. MacManus-Driscoll, and M. Blamire, "Large electric polarization and exchange bias in multiferroic $BiFeO_3$", Adv. Mater. **18**, 1445 (2006).

[85]J. Dho and M. Blamire, "Controlling the exchange bias in multiferroic $BiFeO_3$ and NiFe bilayers", J. Appl. Phys. **106**, 073914 (2009).

[86]J. Heron, M. Trassin, K. Ashraf, M. Gajek, Q. He, S. Yang, D. Nikonov, Y. Chu, S. Salahuddin, and R. Ramesh, "Electric-Field-Induced Magnetization Reversal in a Ferromagnet-Multiferroic Heterostructure", Phys. Rev. Lett. **107**, 217202 (2011).

[87]D. C. Worledge and T. H. Geballe, "Spin-polarized tunneling in $La_{0.67}Sr_{0.33}MnO_3$", Appl. Phys. Lett. **76**, 900–902 (2000).

[88]R. Ramesh and N. A. Spaldin, "Multiferroics: progress and prospects in thin films", Nat. Mater. **6**, 21–29 (2007).

[89]J. Ma, J. M. Hu, Z. Li, and C. W. Nan, "Recent Progress in Multiferroic Magnetoelectric Composites: from Bulk to Thin Films", Adv. Mater. **23**, 1062–1087 (2011).

[90]S. Zhang, P. M. Levy, and A. Fert, "Mechanisms of spin-polarized current-driven magnetization switching", Phys. Rev. Lett. **88**, 236601 (2002).